



# MONASH University

## **Multifunctional nanostructured coatings using cellulose nanocrystals**

*Ragesh Prathapan*

*BEng, M.Tech in Nanotechnology (Gold medallist)*

A thesis submitted for the degree of *Doctor of Philosophy* at  
Monash University in 2018  
School of Chemistry, Faculty of Science

*Dedicated to my Mom and Dad*

ഹരേ കൃഷ്ണ



## **Copyright notice**

© Ragesh Prathapan (2018).

I certify that I have made all reasonable efforts to secure copyright permissions for third-party content included in this thesis and have not knowingly added copyright content to my work without the owner's permission.

## Table of Contents

Copyright notice.....	ii
Abstract.....	vii
Declaration.....	viii
Publications during enrolment.....	ix
Thesis including published works declaration.....	x
Acknowledgements.....	xiii
List of Figures.....	xv
List of Tables.....	xx
List of Abbreviations.....	xxi
<b>Chapter 1 – Introduction</b> .....	2
Preface for Chapter 1.....	1
1.1 Cellulose, its structure and sources.....	2
1.2 Cellulose nanocrystals – preparation and applications.....	6
1.2.1 Preparation of cellulose nanocrystals.....	6
1.2.2 Application of cellulose nanocrystals.....	12
1.3 Alignment of cellulose nanocrystals.....	16
1.3.1 Self-assembly of cellulose nanocrystals.....	16
1.3.2 Shear-based alignment of cellulose nanocrystals.....	17
1.3.3 Magnetic alignment of cellulose nanocrystals.....	20
1.3.4 Electric Field alignment of cellulose nanocrystals.....	22
1.3.5 Other techniques of aligning cellulose nanocrystals.....	24
1.4 Conclusions.....	27
1.5 References.....	27
<b>Chapter 2 – Methods and Instruments</b> .....	36
Preface for Chapter 2.....	35

2.1 Atomic force microscopy (AFM) .....	36
2.2 Contact angle measurements (CA) .....	39
2.3 Dynamic light scattering systems (DLS) – measuring zeta potential .....	42
2.4 References.....	47

### **Chapter 3 – Modulating the zeta potential of cellulose nanocrystals using salts and**

<b>surfactants</b> .....	50
Preface for Chapter 3 .....	49
Introduction.....	51
Experimental .....	51
Materials .....	51
CNC preparation .....	51
Instrumentation techniques .....	51
AFM sample preparation .....	52
Results and discussions.....	52
Conclusions.....	56
Supplementary Material.....	58

### **Chapter 4 – Decreasing the wettability of cellulose nanocrystal surfaces using wrinkle-based**

<b>alignment</b> .....	60
Preface for chapter 4 .....	59
Introduction.....	60
Experimental section.....	61
Materials .....	61
Instrumentation techniques .....	61
PDMS preparation .....	61
Aligned CNC preparation .....	61
Control sample preparation.....	62

Measuring contact angle and roll-off angle .....	62
Results and discussion .....	63
Stamping process and optimization of the transfer polymers .....	63
Periodicity, defects, and ordering .....	64
Wetting and contact angle hysteresis .....	65
Oil contact angle and hysteresis studies on aligned CNC surfaces in water .....	67
Conclusions.....	67
Supporting information.....	70
<b>Chapter 5 – Surface engineering of transparent cellulose nanocrystal coatings for biomedical applications .....</b>	<b>75</b>
Preface for Chapter 5 .....	74
Introduction.....	76
Experimental section.....	78
Materials .....	78
Instrumentation techniques .....	79
CNC coating preparation .....	79
Cellulose acetate and regenerated cellulose preparation .....	80
Testing protocol – blood typing studies and its quantification .....	80
Measuring contact angle .....	81
Results and discussion .....	81
Surface morphology.....	82
Wettability.....	84
Drying profile: effect of fluid and surfaces.....	86
Comparing cellulose nanocrystal to amorphous cellulose surface .....	92
Blood typing on transparent cellulose nanocrystal coatings.....	93
Conclusion .....	99

Supporting information.....	104
<b>Chapter 6 – Enhancing printing resolution on hydrophobic polymer surfaces using aligned cellulose nanocrystal coatings .....</b>	<b>110</b>
Preface for Chapter 6 .....	109
Experimental procedures .....	126
Materials .....	126
Instrumentation techniques .....	126
PDMS wrinkles and aligned CNC preparation.....	127
Supporting information.....	124
<b>Chapter 7 – Concluding comments and future directions .....</b>	<b>129</b>

---

## Abstract

Cellulose nanocrystals are derived from microcrystalline cellulose using acid hydrolysis, resulting in needle-shaped crystals with dimensions of 175 nm length and 5 nm width. A great deal of research on these materials has been reported previously, demonstrating tremendous applications in various fields like nanofillers for reinforcement of polymer composites, cast coatings for diagnostic and photonic applications, packaging materials, etc.

In this thesis, we have explored the utility of cellulose nanocrystals (CNCs) in diagnostic and polymer coating applications, informed by a fundamental understanding of their colloidal stability. Atomic force microscopy (AFM), contact angle measurements and phase analysis light scattering (PALS) were used to characterize CNCs and the materials produced by their alignment on various solid surfaces. The zeta potential of CNCs was modulated using different salts and surfactants (Chapter 3). These dispersions were then cast into films, from which surface roughness was calculated to understand its relationship with the zeta potential under various pH conditions. Wrinkle-based alignment (surface patterning on poly(dimethyl siloxane) achieved using plasma oxidation under different strain rates) was employed to create aligned CNC using a water-mediated transfer process, and the effect of alignment on wettability at different wrinkle periodicities was analysed (Chapter 4). With the wrinkle-based alignment, it was possible to hydrophobize a surface coated with CNCs without any chemical functionalization, thus retaining the CNCs native hydrophilic nature. These aligned CNCs were then cast as thin transparent coatings on glass substrates to analyse the drying mechanism of red blood cell stains for diagnostic applications (Chapter 5). Aligned and randomly distributed CNCs behaved similarly when analysing the drying profiles of red blood cells, which could be used for further morphological characterizations using various imaging techniques. In Chapter 6, aligned CNCs were coated onto hydrophobic polystyrene surfaces to enhance printing resolution when using water-based inks by preventing ink bleeding, a traditional disadvantage of hydrophobic polymers.

---

## Declaration

This thesis contains no material which has been accepted for the award of any other degree or diploma at any university or equivalent institution and that, to the best of my knowledge and belief, this thesis contains no material previously published or written by another person, except where due reference is made in the text of the thesis.

Signature: ...



.....

Print Name: ...Ragesh Prathapan.....

Date: .....2<sup>nd</sup> August, 2018.....

## **Publications during enrolment**

- 1) **Ragesh Prathapan**, Joseph D Berry, Andreas Fery, Gil Garnier and Rico F Tabor, **Decreasing the Wettability of Cellulose Nanocrystal Surfaces Using Wrinkle-Based Alignment**, ACS Applied Materials & Interfaces, 2017, 9, 15202–15211.  
Publication Link: <http://pubs.acs.org/doi/abs/10.1021/acsami.7b03094>
- 2) **Ragesh Prathapan**, Rajiv Thapa, Gil Garnier and Rico F Tabor, **Modulating the zeta potential of cellulose nanocrystals using salts and surfactants**, Colloids and Surfaces A: Physicochemical and Engineering Aspects, 2016, 509, 11–18.  
Publication Link: <http://www.sciencedirect.com/science/article/pii/S0927775716307208>
- 3) **Ragesh Prathapan**, Heather McLiesh, Gil Garnier and Rico F Tabor, **Surface Engineering of Transparent Cellulose Nanocrystal Coatings for Biomedical Applications**, ACS Applied Bio Materials, 2018, 1, 728-737.  
Publication Link: <https://pubs.acs.org/doi/abs/10.1021/acsabm.8b00193>



## Thesis including published works declaration

I hereby declare that this thesis contains no material which has been accepted for the award of any other degree or diploma at any university or equivalent institution and that, to the best of my knowledge and belief, this thesis contains no material previously published or written by another person, except where due reference is made in the text of the thesis.

This thesis includes 2 original papers published in peer reviewed journals and 2 submitted publications. The core theme of the thesis is Cellulose nanocrystal coatings and its applications. The ideas, development and writing up of all the papers in the thesis were the principal responsibility of myself, the student, working within the School of Chemistry, Monash University under the supervision of Dr Rico F Tabor and Prof Gil Garnier.

(The inclusion of co-authors reflects the fact that the work came from active collaboration between researchers and acknowledges input into team-based research.)

In the case of Chapters 3, 4, 5 and 6 my contribution to the work involved the following:

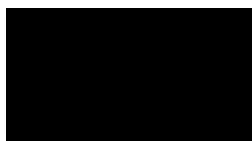
Thesis Chapter	Publication Title	Status (published, in press, accepted or returned for revision, submitted)	Nature and % of student contribution	Co-author name(s) Nature and % of Co-author's contribution*	Co-author(s), Monash student Y/N*
3	Modulating the zeta potential of cellulose nanocrystals using salts and surfactants	Published	87.5%. Experimental works, analysis of results and writing manuscript.	1) Rajiv Thapa, AFM imaging of the sample, 2.5%  2) Gil Garnier, concept and inputs for manuscript work, 5%  3) Rico F Tabor, concept and inputs for manuscript work, 5%	Yes  No  No

4	Decreasing the Wettability of Cellulose Nanocrystal Surfaces Using Wrinkle-Based Alignment	Published	85%. Experimental works, analysis of results and writing manuscript.	<p>1) Joseph D Berry, customized software for contact angle measurement, 2.5%</p> <p>2) Andreas Fery, concept of wrinkling, 2.5%</p> <p>3) Gil Garnier, concept and input for manuscript work, 5%</p> <p>4) Rico F Tabor, concept and inputs for manuscript work, 5%</p>	<p>No</p> <p>No</p> <p>No</p> <p>No</p>
5	Surface Engineering of transparent cellulose nanocrystal coatings for biomedical applications	Published	80%. Experimental works, analysis of results and writing manuscript.	<p>1) Heather McLiesh, Blood testing protocol, 10%</p> <p>2) Gil Garnier, concept and input for manuscript work, 5%</p> <p>3) Rico F Tabor, concept and inputs for manuscript work, 5%</p>	<p>No</p> <p>No</p> <p>No</p>

6	Enhancing printing resolution on hydrophobic polymers surfaces using aligned cellulose nanocrystal coatings	Submitted	75%. Experimental works, analysis of results and writing manuscript.	1) Bernhard Alexander Glatz, Crack-free wrinkle design, 2.5%	No
				2) Anik Kumar Ghosh, creating wrinkled PDMS samples, 10%	No
				3) Stefan Michel, Contact angle measurements of water on substrates, 2.5%	No
				4) Gil Garnier, concept and input for manuscript work, 5%	No
				5) Rico F Tabor, concept and inputs for manuscript work, 5%	No

I have renumbered sections of submitted or published papers in order to generate a consistent presentation within the thesis.

**Student signature:**



**Date: 2<sup>nd</sup> August, 2018**

The undersigned hereby certify that the above declaration correctly reflects the nature and extent of the student's and co-authors' contributions to this work. In instances where I am not the responsible author I have consulted with the responsible author to agree on the respective contributions of the authors.

**Main Supervisor signature:**



**Date: 2<sup>nd</sup> August, 2018**

## Acknowledgements

I would like to express my sincere gratitude towards my supervisors: Dr Rico F Tabor and Prof Gil Garnier, who stood as the backbone for me accomplishing my PhD studies. Moreover, being my main supervisor, Rico took the role of a friend, motivating me during all the ups and downs I faced during my candidature. The way both supervisors supported me to think and act thoughtfully in my work has elevated my professional attitude towards handling research. At times of high stress, both motivated me to a great extent and always encouraged me to follow my passion, dancing and choreographing, which really boosted my confidence to work in a stress-free environment.

The financial support of Victoria Government is acknowledged for awarding a Victoria India Doctoral Scholarship, covering by living expenses. This research was supported by an Australian Government Research Training Program (RTP) Scholarship, which covered my tuition fees. I would also like to acknowledge the Monash Centre for Atomically Thin Materials (MCATM) for providing a top-up scholarship during my mid- candidature. Also, I acknowledge the financial support by the German Academic Exchange service (DAAD) through its Thematic Network, Melbourne-Bayreuth Polymer/Colloid Network sponsored from funds of the Federal Ministry of Education and Research (BMBF). I would like to acknowledge Dr Xiya Fang and Dr Flame Burgmann for helping out with training and developing my skills on scanning electron microscopy.

I should really thank my fellow Soft Materials and Colloids group (SMaC Lab) members for being a great part of my PhD life and making this journey filled with joy and happiness. I would also like to thank my co-mates at APPI (Australian Pulp and Paper Institute) for their great support. A few other members of Monash deserve a special mention: Parvathy, who was my best buddy, having lunch and coffee together and whom I envy for her perfect nature for doing everything so systematically; my dance team “Navratna”, my classical dance guru shyama madam, and many more, who made my PhD life so blissful with the divine art.

It's important for me to acknowledge my family members (Mom, Dad, my sisters, my two lovely nieces- akku and kanthari), as no words can express their moral and unconditional support.

This goes especially for my Mom and Dad, who always pray for my bright future and without whom I wouldn't even have been able to start this career. I would like to thank my spiritual guru, Manoj sir who inspired me to rise from most of the material pitfalls in my life. And definitely my sweet hearts: Arjun and Raju for their great moral support. All these great opportunities couldn't be achieved without the grace and blessings of my lord, Krishna and hence I humbly offer this thesis at his lotus feet and seek for his mercy to use the knowledge I achieved for the betterment and welfare of the mankind and other living beings.

## List of Figures

### Chapter 1 – Introduction

<b>Figure 1.1.</b> Structure of cellulose .....	2
<b>Figure 1.2.</b> High-pressure homogenizer that converts pulp fibres to micro fibrillated cellulose (MFC) view.....	4
<b>Figure 1.3.</b> Chemo-mechanical treatment for extracting cellulose nanofibers .....	5
<b>Figure 1.4.</b> Scanning electron microscopy, transmission electron microscopy and atomic force microscopy of cellulose nanocrystals .....	7
<b>Figure 1.5.</b> Scanning electron microscopy (SEM) and Transmission electron microscopy (TEM) images of cellulose powder, rod-shaped and spherical shaped cellulose nanocrystals .....	9
<b>Figure 1.6.</b> Schematic diagram illustrating ultra-sonication treatment to produce cellulose nanocrystals from micro-crystalline cellulose .....	11
<b>Figure 1.7.</b> Schematic diagram illustrating the high energy bead milling technique for producing thermally stable cellulose nanocrystals.....	12
<b>Figure 1.8.</b> Schematic diagram illustrating the three-step pathway by which cellulose nanocrystals are fluorescently labelled .....	13
<b>Figure 1.9.</b> Atomic force microscopy images of cellulose nanocrystals prepared via acid hydrolysis of cotton as source material a) without, and b) with surface functionalization with cationic polyelectrolyte.....	15
<b>Figure 1.10.</b> Polarized optical microscopy images of cellulose nanocrystal suspensions with cross hatch pattern, and chiral nematic structures.....	17
<b>Figure 1.11.</b> CNC dispersions at different concentrations subjected to varying shear rates, observed using optical microscopy in cross-polarization mode.....	19
<b>Figure 1.12.</b> Comparison of storage moduli of cellulose nanowhisker reinforced nanocomposites in the presence and absence of a magnetic field .....	21

<b>Figure 1.13.</b> Atomic force microscopy image showing the alignment of CNC films (tunicate source) under the influence of electric field .....	24
--	----

<b>Figure 1.14.</b> Schematic diagram showing the use of wrinkling technology to align cellulose nanocrystals using a water-mediated transfer process .....	26
---	----

## **Chapter 2 – Methods and Instruments**

<b>Figure 2.1.</b> Force-distance curve of an AFM operating in tapping or intermittent contact mode .....	37
---	----

<b>Figure 2.2.</b> Schematic diagram of AFM instrumentation .....	38
---	----

<b>Figure 2.3.</b> Wettability models explaining the dependence of contact angle on surface roughness .....	41
---	----

<b>Figure 2.4.</b> Sessile drop analysis technique for measuring contact angle of a liquid droplet on a solid substrate using tangent fitting .....	42
---	----

<b>Figure 2.5.</b> Schematic representation of electrical double layer developed during electrophoresis .....	44
---	----

<b>Figure 2.6.</b> Schematic representation of the instrumentation of the Brookhaven Zeta PALS system .....	46
---	----

## **Chapter 3 – Modulating the zeta potential of cellulose nanocrystals using salts and surfactants**

<b>Figure 1.</b> The effect of pH on the zeta potential of CNC and characterization results using AFM (atomic force microscopy), XRD (x-ray diffraction) and FTIR (Fourier transform infra-red spectroscopy) .....	52
--	----

<b>Figure 2.</b> The effect of NaCl and CaCl <sub>2</sub> concentration on the zeta potential of CNC at different pH conditions .....	53
---	----

<b>Figure 3.</b> The effect of hydrophobic ions on the zeta potential of CNC .....	53
--	----

<b>Figure 4.</b> Zeta potential measurements for CNC as a function of anionic (SDS) and cationic surfactant (CTAB) concentration, with and without 10 mM NaCl .....	54
---	----

<b>Figure 5.</b> Effect of CNC zeta potential on the RMS roughness of cellulose films .....	55
---	----

<b>Figure 6.</b> AFM images of cellulose nanocrystals (CNC) with cetyltrimethylammonium bromide (CTAB) and calcium chloride (CaCl <sub>2</sub> ) at different concentrations .....	55
--	----

#### **Chapter 4 – Decreasing the wettability of cellulose nanocrystal surfaces using wrinkle-based alignment**

<b>Figure 1.</b> Fabrication of aligned CNC surfaces.....	62
---	----

<b>Figure 2.</b> Atomic force microscopy (AFM) images of wrinkled PDMS coated with CNC and stamping onto a glass slide coated with PEI.....	62
---	----

<b>Figure 3.</b> AFM images of CNC stamped onto a PAE coated glass slide and its stability testing with water.....	63
--	----

<b>Figure 4.</b> (a) AFM height image of wrinkled PDMS at different periodicity and stamped onto PAE/PEI coated glass substrate .....	63
---	----

<b>Figure 5.</b> AFM height images showing the alignment of CNCs on a PAE-coated glass slide from a PDMS wrinkled template with periodicity 444 nm .....	64
--	----

<b>Figure 6.</b> Graphical comparison of the periodicity for wrinkled PDMS and stamped surfaces along with random CNC surfaces.....	64
---	----

<b>Figure 7.</b> Contact angle hysteresis plots of (a) Aligned nanowrinkled CNC on PAE coated glass surface. (b) Gold sputtered aligned nanowrinkled CNC on PAE surface. (c) Aligned microwrinkled CNC on PAE/PEI coated glass surface.....	66
---	----

<b>Figure 8.</b> (a) The maximum advancing and minimum receding contact angles represented in the form of bar diagram along with critical roll off angle values. (b) Edge profiles obtained from micrography of a water droplet drying on the 637 nm aligned CNC surface .....	67
--	----

<b>Figure 9.</b> Oil contact angle hysteresis plot of aligned microwrinkled CNC on PAE/PEI coated glass surface, random CNC on PAE/PEI surface and the blank glass slide .....	67
--	----

<b>Figure S1.</b> Contact angle of the aligned nano and micro-wrinkled CNC on PAE coated glass surface .....	71
--	----

<b>Figure S2.</b> Contact angle of control samples .....	72
--	----



<b>Figure S3.</b> (a) Oil contact angle measuring set-up and the contact angles measured with oil droplets residing on different surfaces.....	73
--	----

## **Chapter 5 – Surface engineering of transparent cellulose nanocrystal coatings for biomedical applications**

<b>Figure 1.</b> Schematic illustrating the conceptual application of cellulose nanocrystal (CNC) surfaces for blood typing.....	82
--	----

<b>Figure 2.</b> AFM images showing different surfaces used for the blood drying mechanism ..	83
---	----

<b>Figure 3.</b> Contact angle values of reagent blood cells (3% v/v), human blood, and water on different surfaces along with their surface roughness values .....	86
---	----

<b>Figure 4.</b> Drying profile optical images of particle dispersions, reagent blood cells and human blood on different surfaces.....	86
--	----

<b>Figure 5.</b> Drying profile optical images of different RBC concentration of human blood in plasma on random CNC surfaces .....	90
---	----

<b>Figure 6.</b> Optical images of human blood before, after drying and the contact angle sessile drop image on different cellulosic surfaces.....	92
--	----

<b>Figure 7.</b> Optical microscope images of CNC (random), regenerated CNC and glass surfaces with human blood; positive and negative test before and after flushing PBS .....	94
---	----

<b>Figure 8.</b> Quantification of the blood testing study along with optical microscopy images of the O positive blood cells and transparent study of CNC coated glass substrates .....	97
--	----

<b>Figure S1.</b> Contact angle sessile droplets of reagent blood cells and whole blood on different surfaces .....	105
---	-----

<b>Figure S2.</b> AFM height image and the corresponding histogram of scratched random CNC coating surface on glass.....	106
--	-----

## **Chapter 6 – Enhancing printing resolution on hydrophobic polymer surfaces using aligned cellulose nanocrystal coatings**

<b>Figure 1.</b> (i-vi) Schematic representation illustrating the preparation of aligned CNC on polystyrene surface using crack-free wrinkling technology. Topographical atomic force microscopy (AFM) images showing topology of wrinkled PDMS templates at different conditions of spin-coating and CNC concentration .....	114
<b>Figure 2.</b> Atomic force microscopy (AFM) images showing topology of: a) polystyrene (non-plasma treated); b) random CNC on plasma treated polystyrene; c) Aligned CNC on plasma treated polystyrene. d) Column graph comparing the roughness of the surfaces in (a–c); e) The maximum advancing and minimum receding contact angles of water, and the equilibrium contact angle of ink on the model surfaces in this study .....	116
<b>Figure 3.</b> Photographs of text along with the schematic behaviour of ink printed onto test surfaces, and corresponding optical microscopy images for aligned and random CNC coated polystyrene .....	117
<b>Figure 4.</b> Column graph showing the calculated spreading factor of ink on normal (80 gsm white) paper as compared to CNC coated surfaces.....	119
<b>Figure S1.</b> Atomic force microscopy (AFM) height images showing wrinkles on PDMS obtained at different oxidation time and spin-coating conditions .....	124
<b>Figure S2.</b> Atomic force microscopy (AFM) height images showing the polystyrene surface after 2 minutes exposure to 30 W plasma .....	125

**List of Tables**

**Chapter 3 – Modulating the zeta potential of cellulose nanocrystals using salts and surfactants**

**Table S1:** Calculated ionic strength and Debye length for the experiments in which the mobility of CNCs was measured in the presence of salt .....58

**Chapter 5 – Surface engineering of transparent cellulose nanocrystal coatings for biomedical applications**

**Table S1:** Comparison of ratios of width of drying profile (after/before) for different liquid samples on different surfaces.....107

## List of Abbreviations

CNC	cellulose nanocrystals
MFC	micro fibrillated cellulose
SEM	scanning electron microscopy
TEM	transmission electron microscopy
MCC	microcrystalline cellulose
PLA	poly(lactic acid)
PEI	poly(ethyleneimine)
AFM	atomic force microscopy
CA	contact angle
CAH	contact angle hysteresis
DLS	dynamic light scattering
PALS	phase-analysis light scattering
NCC	nanocellulose crystals
RMS	root mean square
cmc	critical micelle concentration
CTAB	cetyltrimethylammonium bromide
SDS	sodium dodecyl sulfate
PDMS	polydimethylsiloxane
PEO	poly(ethylene oxide)
PAE	poly(aminoamide) epichlorohydrin
FT	Fourier transform
OCA	oil contact angle
PTFE	polytetrafluoroethylene
RH	relative humidity
RBCs	red blood cells

PBS	phosphate buffered saline
Anti	antibody
Pos	positive
EDTA	Ethylenediamine tetraacetic acid
PS	polystyrene

# Preface for Chapter 1

Cellulose nanocrystal (CNC) research is a hot topic in the bioprocessing community, especially the utility of these materials in different fields including biomedical and materials applications. In this chapter, we first explore the difference between cellulose, micro-fibrillated cellulose and cellulose nanocrystals. The preparation of cellulose nanocrystals using acid-hydrolysis, ball-milling, *etc.* is then discussed, along with the various applications of CNCs. The chapter later focusses special attention on the alignment of cellulose nanocrystals. Alignment is used to enhance mechanical and thermal properties when used in composites, as photonic materials in iridescent films, *etc.*, as will be evident from the last sections of this chapter. Different methods of alignment including self-assembly, shear-based alignment, magnetic and electric field alignment, spin-coating, dip-coating, *etc.* are discussed in detail.



imparts the material's swelling nature.<sup>[7]</sup> Depending on the chain orientation, there are two allomorphs of cellulose:  $I_{\alpha}$  (monoclinic) and  $I_{\beta}$  (triclinic).<sup>[8]</sup> Hydrogen bonding between the hydroxyl groups present in cellulose holds the chains strongly together. The length of the cellulosic chains vary depending upon the source and are normally in the range of 2 to 20 nm.<sup>[6]</sup> The swelling nature of cellulose limits its applications in many fields, and hence extraction of the crystalline part is required in order to avoid this. This takes in the form of cellulose nanocrystals, which are obtained through various processes including acid hydrolysis, ultrasonication and ball milling. The raw wood pulp is delaminated by mechanical pressure-systems such as high pressure homogenization (**Fig. 1.2**), which yields micro fibrillated cellulose (MFC), the raw source for cellulose nanocrystal synthesis.<sup>[9],[10]</sup> Multiple passes through a homogenizer are required to produce fine MFC; fibre widths of 5-15 nm for MFC were reported by Lindstrom and co-workers.<sup>[11]</sup>

In an open chain glucose molecule, carbons 2, 3, 4 and 5 (**Fig. 1.1**) have a fixed stereochemistry, whereas in the pyranose form, two different stereochemistries at C-1 are possible, as the carbonyl at C-1 can be approached from either side by the hydroxyl at C-1. The molecule is said to have an  $\alpha$ -configuration if the C-6 carbon and the hydroxyl group at C-1 are on the same side.<sup>[12]</sup> However, the C-1 oxygen in cellulose is on the opposite side of the ring, resulting in the so-called  $\beta$  configuration, which extends the cellulosic chain in a linear fashion in which the equatorial positions possess all the functional groups.<sup>[13]</sup> Such a  $\beta$ -configuration makes cellulose a potential candidate as a fiber-polymer, as highly ordered structures are seen in cellulose due to the grouping of the chains by hydrogen bonding. In most cellulosic materials, the cellulose chains have both crystalline and disordered regions. The fiber acquires good strength and insolubility in most solvents through the inter-chain hydrogen bonds, which are stronger in crystalline regions. The chains in less ordered regions are less densely packed, facilitating more hydrogen bonding to other molecules such as water.



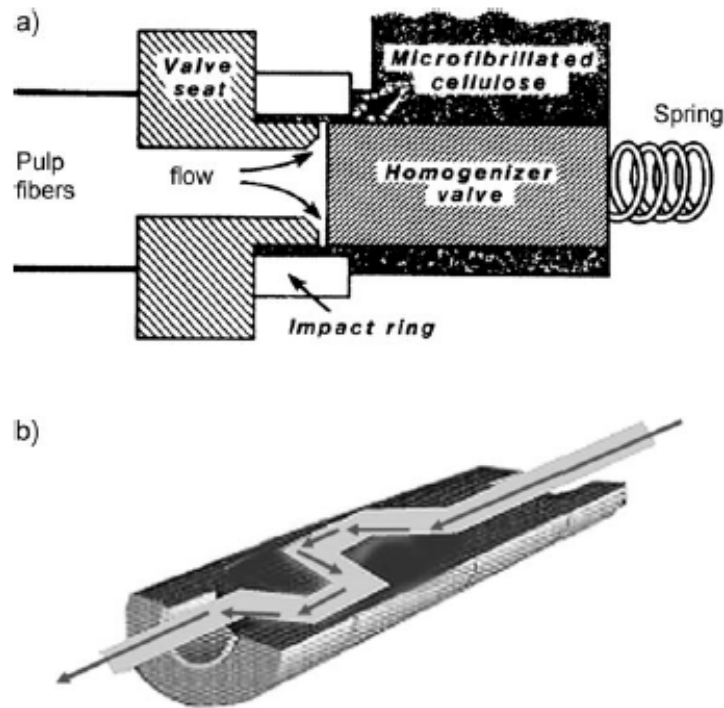


**Figure 1.2.** a) High-pressure homogenizer that converts pulp fibres to micro fibrillated cellulose (MFC). b) Schematic showing the high-pressure micro fluidizer interior view. Reproduced with permission from reference 10. Copyright © 2011, John Wiley and Sons.

Based on the origin, cellulose fibers can be classified into seed, bast, fruit, leaf, stalk and grass. For composite applications, the most commonly used classes are leaf and bast types.<sup>[14]</sup> Several factors such as climate, harvest, modification of fiber, technical processes, *etc.* affect the properties of cellulose fibers.<sup>[15]</sup> The key factors relevant to cellulose research are the material's relatively high stiffness, high strength and low density.<sup>[16]</sup> For the development of reinforced nano-composites, cellulose nanofibers have been extensively used. Several literature studies have reported the synthesis of cellulose nanofibers from natural plant sources and their characterization. Purified nanofibers of diameter 10-80 nm were extracted from wheat straw using a chemo-mechanical treatment, reported by Alemдар and Sain.<sup>[17]</sup> Zimmermann, *et al.* synthesized nano fibrillated cellulose (NFC) from various cellulose

sources.<sup>[18]</sup> The length and diameter of the synthesized NFC was found to be below 100 nm. Wang and Sain extracted cellulose nanofibers from soybean stock using a chemo-mechanical treatment as seen in **Fig. 1.3**.<sup>[19]</sup> The extracted cellulose nanofibers were found to have lengths on the order of thousands of nanometers and diameters between 100 and 500 nm.

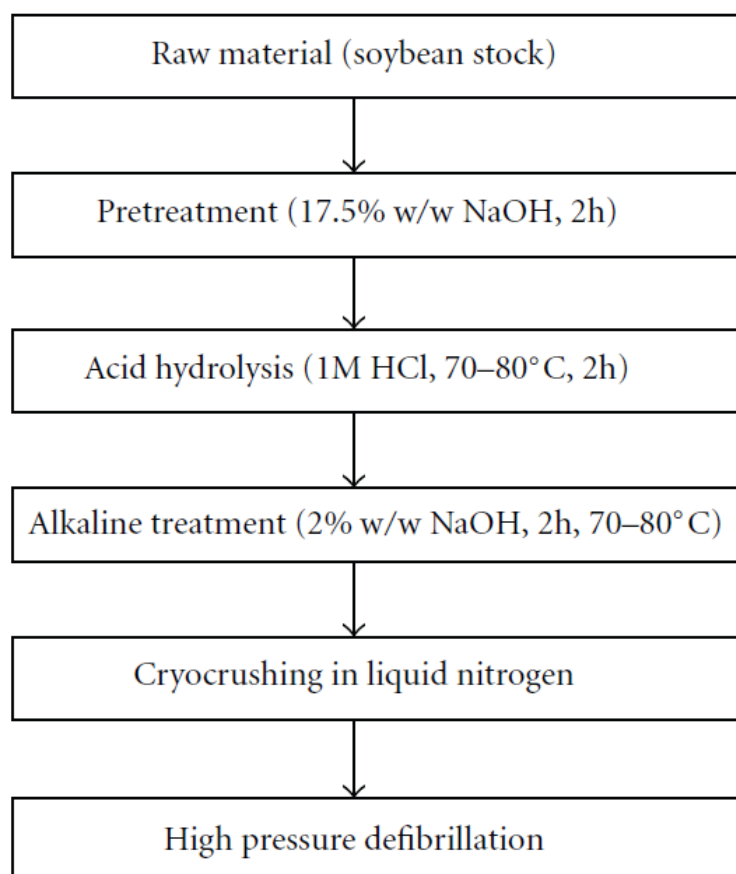


**Figure 1.3.** Chemo-mechanical treatment for extracting cellulose nanofibers. Reproduced with permission from reference 19. Copyright © 2006, John Wiley and Sons.

It is often necessary to increase the hydrophobicity of cellulose fibers and improve the matrix-fiber interaction so as to fabricate composites with better mechanical properties and environmental performance. The use of plant cellulose-reinforced composites is currently seen

as less attractive due to several factors such as low melting point, poor moisture resistance, and lack of good interfacial adhesion. To tackle these issues, cellulose fiber surfaces can be subjected to pretreatments that chemically modify and rarify the surface along with enhancing the surface roughness.<sup>[20],[21]</sup> So far, the best pre-treatment methods reported for surface modification of natural fibers include silylation,<sup>[20]</sup> peroxide benzylation,<sup>[22]</sup> graft copolymerization,<sup>[20]</sup> mercerization<sup>[23]</sup> and bacterial cellulose treatment.<sup>[24],[25],[26]</sup>

## **1.2 Cellulose nanocrystals- preparation and applications**

### ***1.2.1 Preparation of cellulose nanocrystals***

In the materials community, cellulose nanocrystals (CNCs) have garnered significant interest due to their abundance, inherent renewability, sustainability and excellent physical and chemical properties.<sup>[6]</sup> Also, CNCs are promising candidates for reinforcing nano-composites owed to their light weight, low-cost, nanoscale dimensions and unique morphology. CNCs are also referred to in the literature by different names including nanocrystals, whiskers, and microcrystals.<sup>[27]</sup> Acid hydrolysis is the main process for isolation of CNCs from cellulose fibers. During acid hydrolysis, crystalline regions remain intact (as they are resistant to acid attack) whereas hydrolysis of disordered cellulose regions occurs.<sup>[6]</sup> Such an acid treatment produces rod-like cellulose nanocrystals. It was found that the morphology and crystallinity of the original cellulose fibers is retained in CNCs as seen in **Fig. 1.4**.<sup>[28]</sup> The kinetic difference in hydrolysis rates between the crystalline and amorphous regions is the key factor for controlled acid cleavage and hence crystalline regions remain, while amorphous regions are hydrolysed readily.

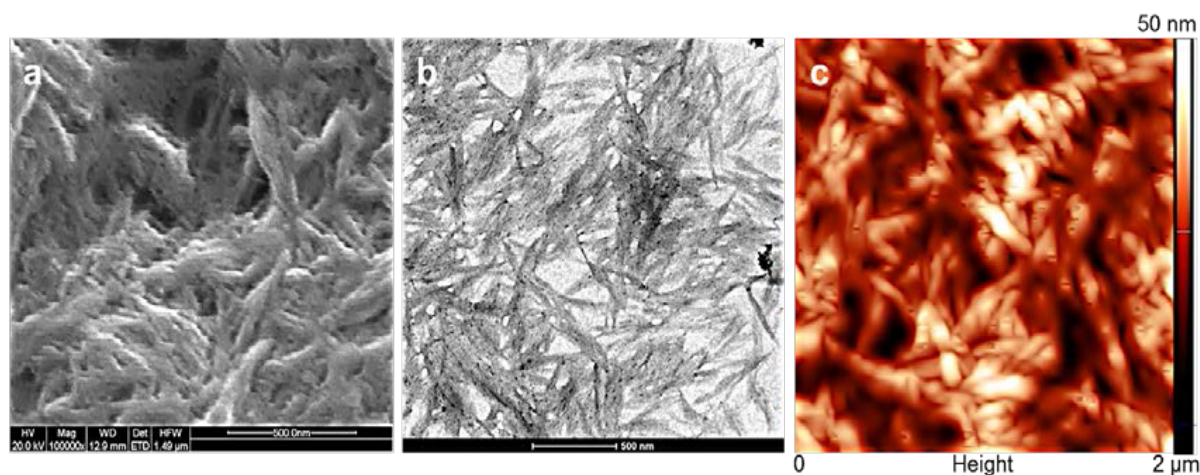


**Figure 1.4.** a) Scanning electron microscopy image (field-emission) of cellulose nanocrystals; b) transmission electron microscopy image of cellulose nanocrystals, and c) atomic force microscopy image of cellulose nanocrystals. Reproduced with permission from reference 28. Copyright © 2013 Science and Education Publishing.

The preparation of CNCs is affected by parameters such as acid-to-cellulosic fiber ratio, and the nature of the acid used. Purification of suspensions after acid treatment involves repeated centrifugations and dialysis for several days. For the acid hydrolysis treatment of CNCs, sulfuric and hydrochloric acids are commonly used. Nevertheless, acid cleavage using phosphoric<sup>[29],[30]</sup> and hydrobromic acids<sup>[31]</sup> has also been reported. It was found that CNCs flocculated and their ability to disperse was limited if the hydrolysis was undertaken using hydrochloric acid.<sup>[32]</sup> However, with sulfuric acid hydrolysis, better dispersion of CNCs in water was observed due to the production of charged surface sulfate esters, formed by the reaction of the acid with the surface hydroxyl groups of cellulose. The downside of this approach is that the thermal stability of the nanocrystals is compromised with the introduction of charged sulfate groups.<sup>[33]</sup> Another reason that hydrochloric acid is less attractive for hydrolysis is apparent from rheological behavior differences. It was seen that a suspension treated with hydrochloric acid showed thixotropic and anti-thixotropic behavior at

concentrations of 0.5% and 0.3% respectively,<sup>[32]</sup> whereas with sulfuric acid, no time-dependent viscosity was observed for the suspension. It was seen that spherical CNCs were obtained when the hydrolysis was carried out using a combination of hydrochloric and sulfuric acids with concurrent ultrasonic treatment.<sup>[34],[35]</sup> As these spherical CNCs possess fewer sulfate groups on their surfaces, they exhibit good thermal stability.<sup>[35]</sup> Bondenson, *et al.* demonstrated that a CNC yield of 30% with length between 200 and 400 nm and width less than 10 nm could be obtained when using sulfuric acid with a concentration of 63.5% (w/w) over 2 h.<sup>[36],[37]</sup>

A decrease in nanocrystal length and increased surface charge was observed if the hydrolysis time was prolonged for several hours.<sup>[38]</sup> Based on the hydrolysis conditions and cellulosic material source, the geometry of CNCs can vary widely. Such variation is due to the acid hydrolysis, which is diffusion-controlled. Chemical functionalization of CNCs is carried out either by introducing positively or negatively charged groups on their surface, or by tuning their surface energy characteristics, improving their dispersion and compatibility in composites. Lu, *et al.* used cotton cellulose as the starting material for cellulose nanocrystal preparation, wherein acid hydrolysis followed by freeze-drying yielded rod-like, spherical and network morphologies as seen in **Fig. 1.5**.<sup>[39]</sup> Dispersion in aqueous media was facilitated by the sulfate groups introduced by sulfuric acid hydrolysis, whereas improved specific surface area and meso-porosity was induced by freeze-drying.

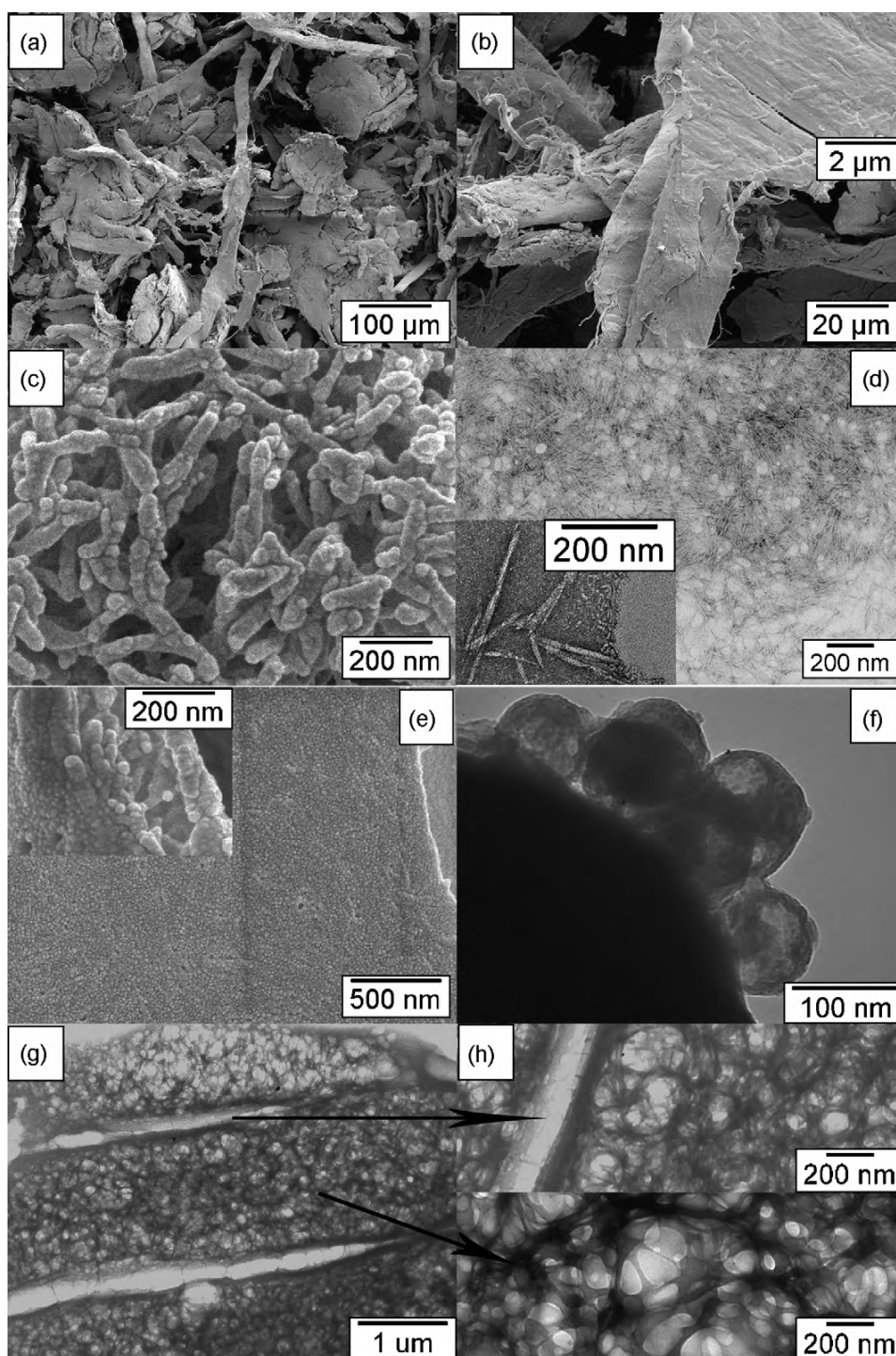


**Figure 1.5.** Scanning electron microscopy (SEM) images of (a and b) cellulose powder, (c and e) rod-shaped and spherical shaped cellulose nanocrystals respectively. Transmission electron microscopy images (TEM) to study the rod shaped (d), spherical shaped (f) and network shaped cellulose nanocrystals prepared. Reproduced with permission from reference 39. Copyright © 2010 Elsevier Ltd.

Few works have been reported with respect to preparation of cellulose nanocrystals using physical treatments. Li, *et al.* used high intensity ultra-sonication to prepare rod-shaped CNCs (diameter: 10-20 nm; length: 50-250 nm) from microcrystalline cellulose (MCC).<sup>[40]</sup> Ultra-sonication treatment had an inverse effect on the crystallinity and length of CNCs prepared. Nevertheless, the technique is limited by its non-selective nature, cleaving both crystalline and amorphous parts of MCC (**Fig. 1.6**). An ultra-sonically assisted enzymatic process was used to prepare cellulose nanocrystals (CNC) from wheat MCC.<sup>[41]</sup> The resulting nanocrystals had width less than 10 nm and length of 40-50 nm, which was sensitive to the ultra-sonication process. Tang, *et al.* observed the morphological similarity in cellulose nanocrystals prepared via acid hydrolysis with and without ultrasonic treatment;<sup>[42]</sup> the yield was slightly higher when using ultra-sonic treatment. A similar study was also carried out by Guo, *et al.* to explore the effects of ultra-sonication treatments on the CNC structure.<sup>[43]</sup> A disordered CNC structure was obtained when the CNC was subjected to prolonged acid attack under ultra-sonication. Similar effects were also observed in the work reported by Li, *et al.*, wherein surface erosion of cellulose folding, along with reduced CNC length occurred during ultra-sonication for preparation of CNCs.<sup>[44]</sup> A FeCl<sub>3</sub>-catalyzed hydrolysis technique assisted by ultra-sonication was used to prepare CNCs from bamboo pulp.<sup>[45]</sup> The prepared CNCs had a rod-shaped morphology and formed an interconnected network structure with a width of 10-20 nm and length of 100-200 nm. The conventional acid-based hydrolysis technique was found to yield cellulose nanocrystals of poor thermal stability, and use of strong acids and solvents makes it industrially laborious.<sup>[35]</sup> Hydrothermal treatment using hydrochloric acid and mild-acid treatments such as phosphoric acid have also been used to prepare thermally stable CNCs.<sup>[46],[47]</sup> However, the prepared CNCs showed poor scalability and low yield. Recently, high energy bead milling (**Fig. 1.7**) was employed to isolate rod-shaped CNCs (freeze-dried) from MCC in an aqueous medium.<sup>[48]</sup> The obtained yield was between 57-76% and the CNCs

were found to be thermally stable (degradation temperature: 250°C). The use of dilute phosphoric acid along with the milling technique resulted in CNCs with aspect ratio 21 to 33, with high crystallinity. Irrespective of the high yield, the technique may not be viable for industrial purposes owing to the contamination of cellulose nanocrystals with zirconium (in high ppm quantities) and the aggregation of cellulose nanocrystals due to the effects of the high energy imparted during the ball milling technique.

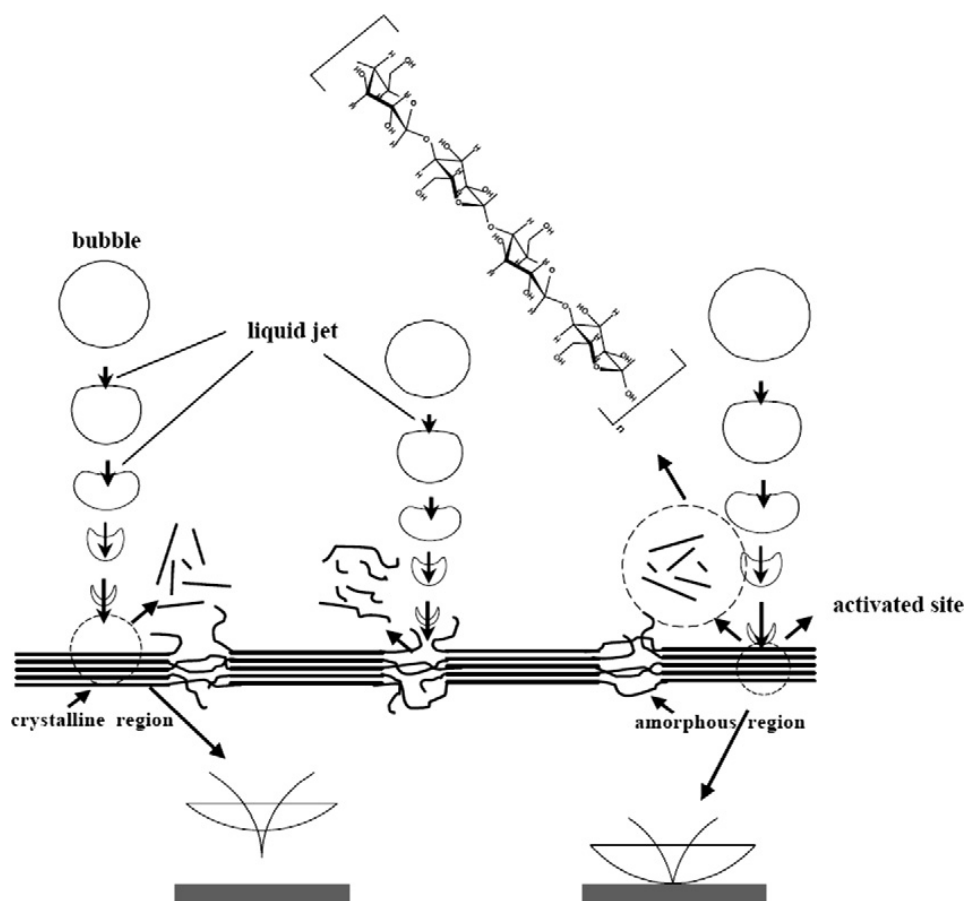


**Figure 1.6.** Schematic diagram illustrating ultra-sonication treatment to produce cellulose nanocrystals from micro-crystalline cellulose. Reproduced with permission from reference 40.

Crown copyright © 2011 Published by Elsevier B.V. All rights reserved.



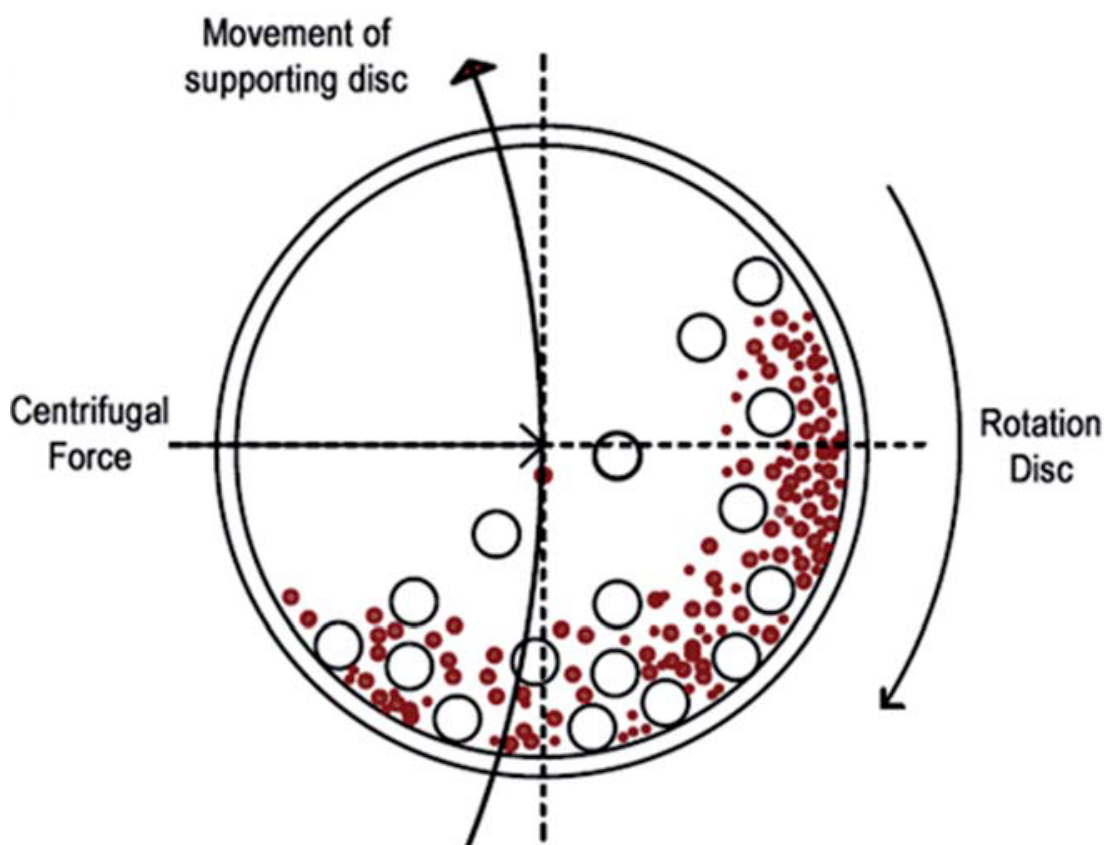


**Figure 1.7.** Schematic diagram illustrating the high energy bead milling technique for producing thermally stable cellulose nanocrystals. Reproduced with permission from reference 48. Copyright © 2015, Royal Society of Chemistry.

### ***1.2.2 Application of cellulose nanocrystals***

Owing to their intrinsic properties such as high surface area, and mechanical strength, CNCs find immense applications in the nanocomposites field.<sup>[49]</sup> The presence of hydroxyl functional groups makes them readily available for chemical functionalization, facilitating their incorporation into various polymer matrices.<sup>[50],[51],[52],[53],[54]</sup> These polymer composites find applications in packaging, textiles, coatings, and automobile parts. To detect the in vivo interaction of cellulose nanocrystals with cells, cellulose nanocrystals have been fluorescently

labelled using a three-step reaction pathway (**Fig. 1.8**).<sup>[55]</sup> The process dissolved softwood pulp using sulfuric acid and incorporated covalently bonded fluorescent molecules onto cellulose nanocrystal surface to enable fluorescent detection of the CNC location in vivo .

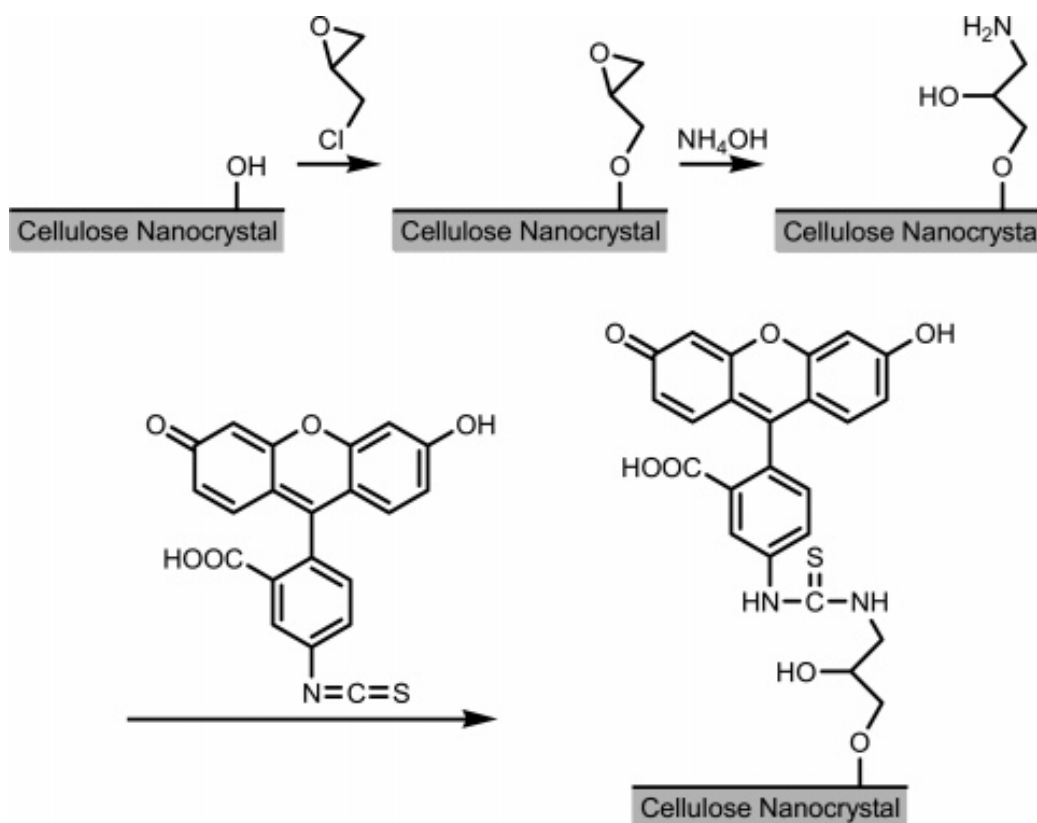


**Figure 1.8.** Schematic diagram illustrating the three-step pathway by which cellulose nanocrystals are fluorescently labelled. Reproduced with permission from reference 55. Copyright © 2007, American Chemical Society.

The thermal and mechanical performance of polyurethane based composites was found to be affected by the addition of cellulose nanocrystals during polymerization that induced variations in polymer microstructure. The addition of cellulose nanocrystals acted as the limiting factor for deformation and modulus of the nanocomposites synthesized.<sup>[56]</sup> A decrease in thermal resistance was found when cellulose whiskers were incorporated as a filler into polylactic acid (PLA) nanocomposites.<sup>[57]</sup> Depending on the concentration of the filler,

mechanical properties (modulus) of the composite varied by enhancing the brittleness of the PLA nanocomposites.<sup>[58]</sup> A decrease in tensile storage modulus was observed when a percolated network of cellulose whiskers was introduced into poly(vinyl acetate) under simulated physiological conditions.<sup>[59]</sup> The materials prepared also exhibited a decreased swelling which could potentially be used for other biomedical applications.<sup>[59]</sup> Composite sheets were prepared using a solution casting method incorporating cellulose nanocrystals into poly(methyl methacrylate) nanocomposites, retaining the material's transparency. The introduction of CNCs enhanced the storage modulus and thermal stability of the prepared nanocomposite.<sup>[60]</sup> Cellulose nanowhiskers assembled layer-by-layer with chitosan were used to prepare a biodegradable nanocomposite with high density. The prepared nanocomposite used nanowhiskers obtained from eucalyptus wood pulp by acid hydrolysis, which were homogeneously distributed within the chitosan layers.<sup>[61]</sup> Such nanocomposites serve as a high-performance renewable materials. The methodology used in preparation of these nanocomposites could be extended for the preparation of new bio-based nanocomposites, which could be used in several applications including food packaging and biomedical applications. Recently, cellulose nanocrystals were used in coating technologies for drug delivery applications, owing to their non-toxic behaviour.<sup>[62],[63],[64]</sup>

Cationic functionalization of cellulose nanocrystals was carried out by Hasani, *et al.* using epoxypropyltrimethylammonium chloride (EPTMAC).<sup>[65]</sup> The functionalized cellulose nanocrystals (**Fig. 1.9**) obtained from cotton via acid hydrolysis showed reduced total surface charge density, resulting in unexpected rheological and gelling properties, and forming stable aqueous suspensions.<sup>[65]</sup> Similar surface modification of cellulose nanocrystals was carried out by Salajkova, *et al.* using quaternary ammonium salts.<sup>[66]</sup> Strong birefringence was observed for modified CNCs when suspended in toluene, and a water contact angle increase from 12° to 71° was found upon modification of the CNCs. Various other surface functionalizations of

CNCs have been reported to form stable CNC suspensions with either enhanced hydrophobicity or birefringence.<sup>[67],[68a],[68b]</sup> Eyley, *et al.* reported different methods of surface modifications of cellulose nanocrystals including oxidation, esterification, amidation, carbamation, etherification and nucleophilic substitution.<sup>[68c]</sup> However, in this thesis, less emphasis is placed on such chemical modifications, which affect the surface functional groups and change the surface characteristics.

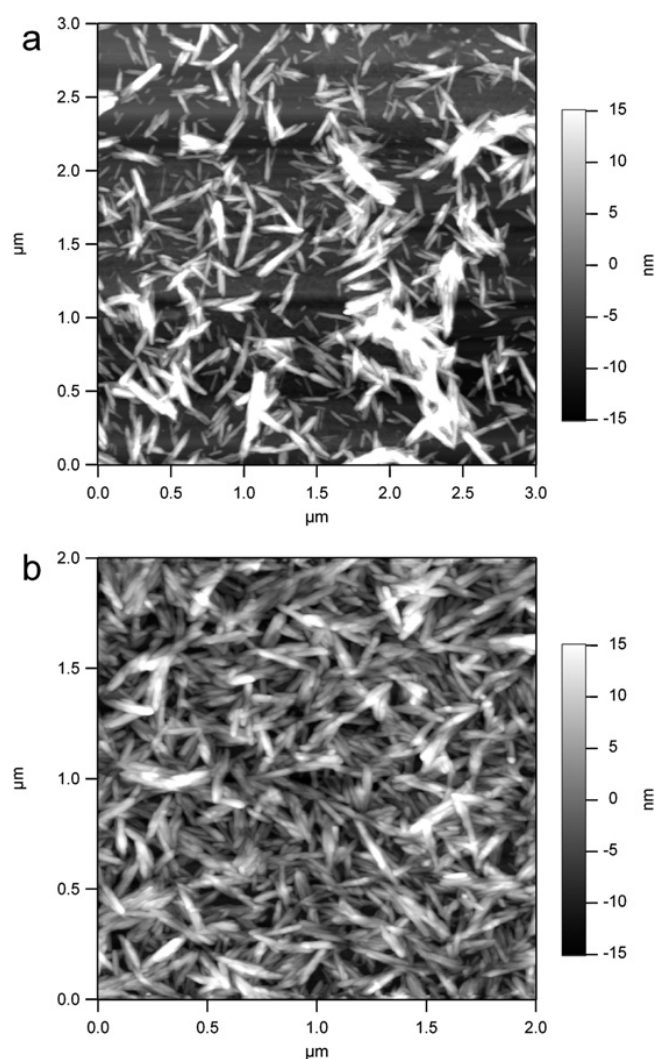


**Figure 1.9.** Atomic force microscopy images of cellulose nanocrystals prepared via acid hydrolysis of cotton as source material a) without, and b) with surface functionalization with EPTMAC. Reproduced with permission from reference 65. Copyright © 2008, Royal Society of Chemistry.

## 1.3 Alignment of Cellulose Nanocrystals

### 1.3.1 Self-assembly of cellulose nanocrystals

Negatively charged sulphate groups are created on the surface of CNCs upon acid hydrolysis of MFC using sulfuric acid, which electrostatically repel each other to form stable CNC dispersions. To minimize these electrostatic interactions, cellulose nanocrystals in concentrated suspensions configure themselves to give specific local orientations.<sup>[6]</sup> Similar self-assembly was seen with other rod like structures that exist as non-flocculating suspensions.<sup>[69],[70],[71]</sup> Chiral nematic liquid crystalline structure, characterized by a fingerprint-like pattern occurs due to this self-assembly, which could be observed using an optical microscope in crossed polarization mode.<sup>[72]</sup> Such an ordered chiral nematic phase (**Fig. 1.10**) occurs only when the concentration of CNCs reaches a critical concentration, forming an orientationally anisotropic phase.<sup>[73],[74]</sup> Shear birefringence is shown by the CNCs at concentrations above the critical concentration.<sup>[75]</sup> Certain studies reveal that such chiral nematic order may be attributed to a twist in CNCs, which is inherent in the cellulose backbone and the crystalline material.<sup>[72],[76]</sup> More evidence of such twisting was also provided by studies carried out on surfactant stabilized CNC suspensions.<sup>[77]</sup> These chiral nematic structures go on to form iridescent films upon complete water evaporation. Numerous applications utilize such solid films including security papers and optical coating materials.<sup>[78],[79],[80]</sup> The chiral nematic phase self-assembly of cellulose nanocrystal suspensions was studied by Roman, *et al.*<sup>[81]</sup> Slow evaporation of the suspension resulted in the formation of parabolic focal conic (PFC) defects, which were characterized using atomic force microscopy and polarized light. The ordering of cellulose nanocrystals at concentrations below this nematic phase transition is however a challenging problem. Many studies have attempted to align CNCs using magnetic alignment,

electric field alignment, shear-based alignment, *etc.*, but all these techniques exhibit only local alignment and possess limitations with respect to processing parameters and scalability.

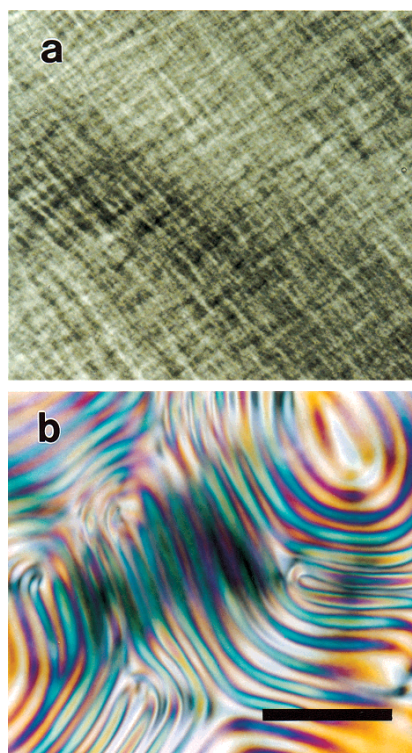


**Figure 1.10.** Polarized optical microscopy images of cellulose nanocrystal suspensions showing a) 7.1% post sulphated suspension with cross hatch pattern, and b) chiral nematic structure with 5.4% solid content exhibiting fingerprint structure obtained during acid hydrolysis. Scale bar: 200  $\mu\text{m}$ . Reproduced with permission from reference 74. Copyright © 2000, American Chemical Society.

### ***1.3.2 Shear-based alignment of cellulose nanocrystals***

Alignment of CNCs in the direction of a shear flow was observed by Orts, *et al.* using small-angle neutron scattering (SANS), wherein the neutron beam was passed perpendicular to the shear flow.<sup>[82]</sup> An increase in alignment of CNCs with shear rate from 0.1 to 7000  $\text{s}^{-1}$  was observed. A similar study was carried out by Ebeling, *et al.* where two shear rates (low: 5  $\text{s}^{-1}$ ; high: 500  $\text{s}^{-1}$ ) were used to align CNCs perpendicular and parallel to the shear direction for low and high shear rates respectively.<sup>[83]</sup> The study indicates that the orientation of CNCs could be

controlled by adjusting the shear rates. The order parameter for isotropic and anisotropic CNC configurations, prepared using various shear rates, was studied by Chowdhury, *et al.*<sup>[84]</sup> The study was carried out to investigate the crystal orientation using UV-vis spectrophotometry, a low-cost and simple technique. Varying shear rates were used to prepare self-standing CNC films of short-range order. Order parameters were calculated by determining the dichroitic ratio, evaluated from the transmitted light intensity of the CNC films when placed between cross-polarizers. Compared to other traditional techniques, the birefringent method employed was inexpensive and reproducible.

Optical contrast measurements (**Fig. 1.11**) were used by Haywood, *et al.* to study the microstructural relaxation effects of shear forces on alignment of CNC films.<sup>[85]</sup> The final structure of CNC films was primarily affected by the combined effects of rheology, relaxation, and dispersion microstructure in the initial stage. Doctor blade coating has been used to shear align CNCs. After relaxation, CNCs coated from an isotropic phase didn't align at lower concentrations. However, at higher concentrations, the degree of freedom<sup>[86]</sup> decreased, as a result of which CNCs aligned at shear rates up to  $100 \text{ s}^{-1}$ . The alignment of CNCs in liquid crystalline dispersions using shear rates from 25 to  $100 \text{ s}^{-1}$  was found to be comparatively easier due to the self-assembly of CNCs in the nematic phase.<sup>[87]</sup>

Uniformly oriented cholesteric CNC helices were prepared by Park, *et al.* using a circular shear-based method, wherein vertical helix orientation was achieved when the concentration of CNCs used was increased into the liquid crystalline range.<sup>[88]</sup> Shear induced alignment of CNCs using 'in-line polarized light imaging integrated single-droplet oscillatory system' (a complex microfluidic imaging technique) was studied by Alizadehgiashi, *et al.*<sup>[89]</sup> The alignment of CNCs was found to be affected by the suspension viscosity and the shear rate, which was analysed using an oscillating droplet (in a capillary) of isotropic aqueous CNC suspension. Alignment of CNCs in fibres using shear-based forces produced by hydrodynamic

flow and spinning has also been reported in the literature.<sup>[90],[91]</sup> Grazing incidence wide-angle X-ray scattering (GIWAX) was used by Sanchez-Botero, *et al.* to measure aligned CNCs at different concentrations (7 wt% and 9 wt%) and to study the influence of other process parameters such as shear-cast velocity and solution concentration on the CNC ordering.<sup>[92]</sup> X-rays were focussed onto a cast film made from CNCs and GIWAX patterns were recorded at fixed intervals of time. It was found that the process parameters (shear velocity, evaporation rate and concentration of precursor suspension) had negligible influence on the CNC orientation.

Convective and shear based forces were used by Hoeger, *et al.* to align CNCs deposited as ultra-thin films on solid supports.<sup>[93]</sup> Using image analysis, the degree of CNC orientation was measured. A CNC concentration of 2.5 % (w/w), far lower than the critical concentration for chiral nematic phase formation, was used for alignment, wherein the CNCs aligned well in the shear withdrawal direction supported by gold and silica substrates. The mechanical strength and wear resistance of the prepared ultra-thin film was enhanced by the shear-based alignment.

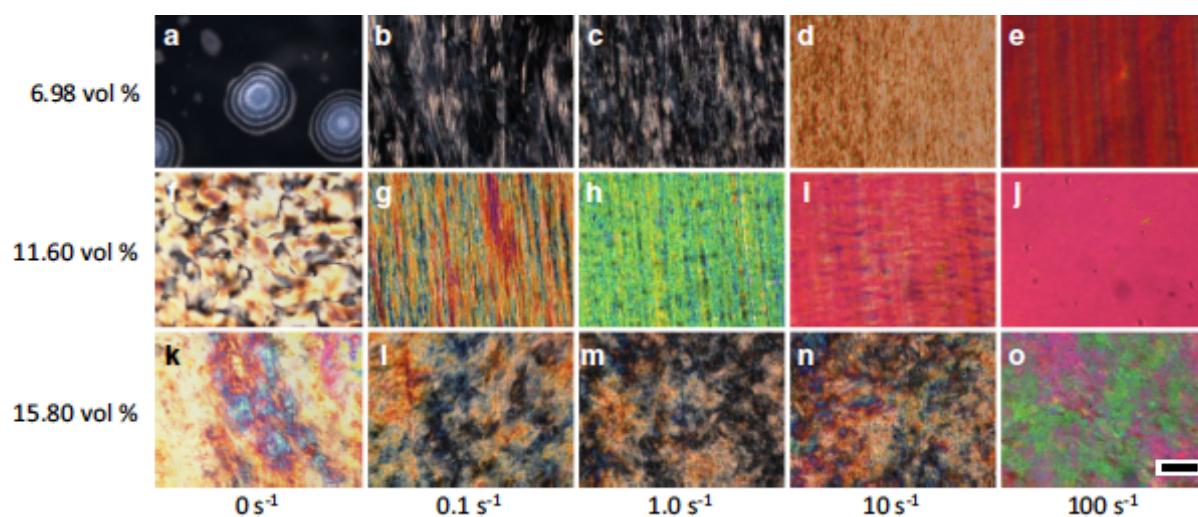


**Figure 1.11.** CNC dispersions at different concentrations subjected to varying shear rates (Flow direction upwards), observed using optical microscopy in cross-polarization mode. Scale bars: 100  $\mu\text{m}$ . Reproduced with permission from reference 85. Copyright © 2016, Springer Science Business Media Dordrecht.



### 1.3.3 Magnetic alignment of cellulose nanocrystals

A magnetic field of 1.2 T was used by Pullawan, *et al.* to align cellulose nanowhiskers (derived from tunicates), which were incorporated into a cellulose matrix system.<sup>[94]</sup> The volume fraction of cellulose nanowhiskers was found to be a key criterion affecting the mechanical properties of the final composite material. It was found that lowering the volume fraction of these cellulose nanowhiskers makes them readily orient under the applied magnetic field. The oriented cellulose nanowhiskers were found to impart enhanced strength and stiffness to the composite. However, the orientation under a 1.2 T magnetic field was incomplete, as 50% of the cellulose nanowhiskers remained misaligned with the magnetic field. A similar study into aligning cellulose nanowhiskers using a magnetic field (1.2 T) was carried out by Li, *et al.* in order to fabricate reinforced nanocomposite paper.<sup>[95]</sup> The paper was made by aligning the nanowhiskers in wood pulp under the influence of magnetic fields, wherein the negative diamagnetic anisotropy of the nanowhiskers was found to be the key characteristic for magnetic alignment. The fabricated nanocomposite paper was found to have a stronger storage modulus in the direction perpendicular to the applied magnetic field, but was weak in the direction parallel to the magnetic field (**Fig. 1.12**). However, only local alignment of cellulose nanowhiskers under the applied magnetic field was again seen.

A non-invasive approach of aligning CNCs using Fe<sub>3</sub>O<sub>4</sub> (51 wt%) in low magnetic fields (~ 60 mT) was reported by Dhar, *et al.*<sup>[96]</sup> In situ precipitation was used to facilitate the adsorption of Fe<sub>3</sub>O<sub>4</sub> nanoparticles onto the CNCs. Poly(lactic acid), PLA was used to disperse these nano-fillers in which the CNCs were aligned (owing to the high magnetic moment of the iron oxide nanoparticles) in the magnetic field. The resultant nanocomposite film was found to possess improved electrical and thermal properties, compared to the non-aligned nanocomposite.<sup>[96]</sup> However, the loading of iron oxide nanoparticles required was very high, limiting its practical application.

Sugiyama, *et al.* were the first to report the magnetic alignment of cellulose microcrystals under strong magnetic fields of 7 T.<sup>[97]</sup> Owing to the diamagnetic susceptibility response of cellulose, the fibre axis of the microcrystals oriented perpendicular to the direction of the magnetic field. Two different types of magnetic field: static and rotating, were used by Kimura, *et al.* to align tunicate cellulose micro-fibrils at a concentration above the critical transition concentration into a chiral nematic phase.<sup>[98]</sup> The micro-fibrils were prepared from cellulosic mantles of tunicin using acid hydrolysis. The fibre axis perpendicular to the magnetic field showed higher diamagnetic susceptibility compared to the fibre axis parallel to the magnetic field. The reported work may not be feasible for industrial purposes however, as very high magnetic fields ranging from 5 T to 28 T were used to achieve alignment. Similar work on alignment of cellulose nanofibers (prepared from regenerated cellulose) under the influence of a strong magnetic field (7 T) was reported by Kim, *et al.*<sup>[99]</sup> The decomposition temperature of the material was found to be greater when aligned using a strong magnetic field.

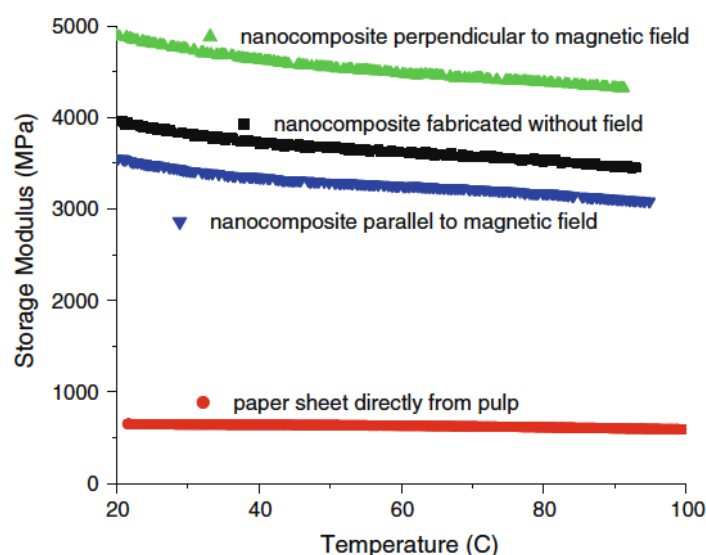


**Figure 1.12.** Comparison of storage moduli of cellulose nanowhisker reinforced nanocomposites in the presence and absence of a magnetic field. Reproduced with permission from reference 95. Copyright © 2010, Springer-Verlag.

Revol, *et al.* reported the magnetic alignment (7 T) of cellulose nanocrystals (axial ratio: 20-40) in the chiral nematic liquid crystalline phase.<sup>[100]</sup> The chiral nematic axis, owing to the negative diamagnetic susceptibility, orients itself parallel to the applied magnetic field. Iridescent cellulose nanocrystal films were prepared by Edgar, *et al.* from cellulose suspensions under the influence of a magnetic field of 7 T, produced within an NMR spectrometer.<sup>[101]</sup> The chiral nematic order of the prepared film was found to increase with the applied magnetic field, which was recorded by measuring induced circular dichroism changes.

Kvien, *et al.* used a strong magnetic field of 7 T to align nanowhiskers in a poly(vinyl alcohol) matrix.<sup>[102]</sup> Enhancement of the dynamic modulus of the nanocomposite by a value of 2 GPa was found in the direction of aligned cellulose nanowhiskers compared to the perpendicular direction. A composite of cationic polymer with cellulose nanocrystals in the chiral nematic phase was used by Cranston, *et al.* to form a polyelectrolyte film, via layer-by-layer assembly.<sup>[103]</sup> The cellulose nanocrystals in the polyelectrolyte film were oriented in a magnetic field of 7 T. Even though the orientation of the nanocrystals was successful, long exposure (~24 h) to the magnetic field was required to achieve complete alignment.

Even though many works have reported magnetic field alignment of cellulose nanocrystals, most of them use high magnetic field strengths (above 5 T) which are not suitable for scalable processing. The low magnetic field alignment of cellulose nanocrystals reported showed only local alignment.

#### ***1.3.4 Electric Field alignment of cellulose nanocrystals***

The alignment of rod-shaped particles<sup>[104],[105]</sup> was previously studied using electric fields, wherein electric birefringence<sup>[106]</sup> was found to be the main reason for orientation of these particles under the influence of the electric field. The electric field alignment of cellulose

nanocrystals was initially studied by Bordel, *et al.* with a frequency ranging from 10 Hz to 10 KHz, wherein non-polar solvents were used to suspend the CNCs to avoid issues arising from the high conductivity of water.<sup>[107]</sup> When an electric field of strength 1200 V/cm was applied, the long axis of the CNCs oriented parallel to the direction of the applied electric field. Habibi, *et al.* used electric field alignment (2000 V/cm; frequency:  $10^4$ - $10^6$  Hz) to orient a cellulose nanocrystal suspension.<sup>[108]</sup> It was found that the strength and frequency of the applied electric field greatly influenced the orientation of cellulose nanocrystals (**Fig. 1.13**).

A coupled mechanism of dielectrophoresis along with convective shear-based assembly was used by Csoka, *et al.* to align CNCs.<sup>[109]</sup> The dielectrophoresis used low electric field strengths of 400 V/cm at frequency of  $\sim 2000$  Hz. A shear rate of 8.4 cm/hr was applied to CNC suspensions of 2.5 wt %, dispersed between mica substrates under the influence of an electric field that oriented the CNCs. The coupled mechanism resulted in greater alignment of CNCs compared to alignment using either technique separately.<sup>[109]</sup> Alignment of CNCs using apolar solvents under the influence of DC and AC electric field systems were studied by Frka-Petesic, *et al.*<sup>[110]</sup> Nevertheless, the two configuration systems (DC and AC) resulted in a similar order of magnitude of electric dipole moments (permanent and induced dipoles under the influence of electric field) of CNCs. Also, electric field alignment of CNCs faces the limitation of achieving only local alignment as seen in many reports, as well the use of toxic solvents, which is industrially undesirable.

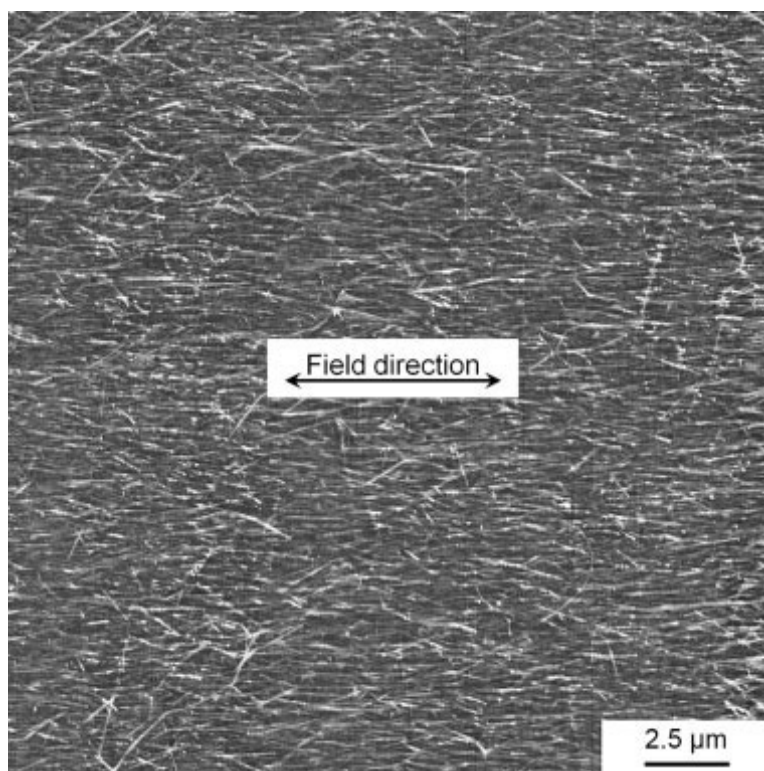


**Figure 1.13.** Atomic force microscopy image showing the alignment of CNC films (tunicate source) under the influence of electric field of strength 10 V and frequency 250 KHz. Reproduced with permission from reference 108. Copyright © 2008, John Wiley and Sons.

### ***1.3.5 Other techniques of aligning cellulose nanocrystals***

Many other techniques of aligning cellulose nanocrystals have been reported in the literature including spin-coating, dip-coating, electro-spinning, freeze-drying, *etc.*<sup>[111]-[117]</sup> Nevertheless, these techniques again fail in achieving the desired global alignment. High levels of alignment of cellulose nanocrystals were achieved by unidirectional freezing of nano cellulose dispersions;<sup>[111]</sup> CNCs at 0.2 wt% aligned in the freezing direction. A stronger resistance to melting was observed from the directionally frozen nano cellulose network.<sup>[111]</sup> Huan, *et al.* fabricated reinforced poly(lactic acid), PLA fibre mats using electro-spinning, wherein 20 wt% CNCs were incorporated into the polymer matrix for electrospinning.<sup>[112]</sup> The alignment technique was found to influence the porous structure of the final composite and

also resulted in the production of fibre mats with a high degree of crystallinity compared to mats made using random CNCs. Also, enhancement of the thermal and mechanical properties of the PLA composite was found with the aligned fibrous structure.<sup>[112]</sup> A similar use of cellulose nanocrystals for reinforcement was reported by Song, *et al.*, wherein electrospinning was used to create aligned poly(vinyl acetate) (PVA)/cellulose nanocrystal composites.<sup>[113]</sup> High tensile strength was observed for the aligned nanofibrous composite, along with a continuous birefringence, owing to the nematic phase of CNC.

Iridescently coloured thin films of CNCs were prepared by spin-coating CNCs onto reflective substrates, owing to thin-film interference (based on film thickness and refractive index).<sup>[114]</sup> The spin-coating conditions including spin-speed (rpm), duration of spinning and concentration of CNC suspension used, are the main factors governing the ordering of CNCs using spin-coating.<sup>[115]</sup> Aligned CNC templates prepared using spin-coating were used to orient muscle cells (myoblasts) that aligned in the direction of the aligned CNCs.<sup>[116]</sup> The aligned CNC for this purpose were fabricated by spin-coating CNCs (tunicate derived) onto a cationic polyelectrolyte coated glass slide. Very poor orientation of CNCs was observed for multi-layered films of CNC with a cationic polyelectrolyte, fabricated using a combination of spin-coating and dip-coating techniques.<sup>[117]</sup> Aligned CNC films using dip-coating have been reported in the literature, wherein the orientation parameter was controlled by the dipping shear action and dipping time.<sup>[118]</sup> Nevertheless, this technique is not feasible for large scale production, owing to the weak degree of orientation obtained. Stable, oriented CNC layers were prepared using Langmuir-Schaeffer (LS) and Langmuir-Blodgett (LB) methods with the help of a cationic surfactant.<sup>[119],[120]</sup> Non-radial and uniaxial alignment of CNCs was achieved using LB and LS techniques. The surfactant after film deposition was removed using chloroform.<sup>[120]</sup> The alignment of CNCs using the LS technique was mainly attributed to the

self-assembly of CNCs resulting in nematic configurations.<sup>[119]</sup> But as discussed earlier, none of the reported techniques was successful in achieving perfect orientation globally.

A new fascinating technology known as wrinkling technology was recently reported, in which wrinkles were created on PDMS substrates upon relaxation of stretched PDMS after plasma exposure.<sup>[121],[122]</sup> The key factors for wrinkle production were the plasma exposure time, plasma power, strain conditions and the type of substrates used.<sup>[122]</sup> So far in the field of alignment of cellulose nanocrystals, only one study has been reported with respect to alignment using wrinkling technology. Nystrom, *et al.* used different wrinkle periodicities to align the rod-shaped cellulose nanocrystals which were transferred to a poly(ethyleneimine) (PEI)-treated silica surface using 1  $\mu$ L milli-Q water, in a so-called water-mediated transfer process (**Fig. 1.14**).<sup>[123]</sup> The transferred CNCs were aligned perfectly, showing a global alignment order. However, the study raises questions regarding the efficient transfer of CNC particles to the intended substrate, and also the robustness of using PEI coated substrates for CNC alignment.

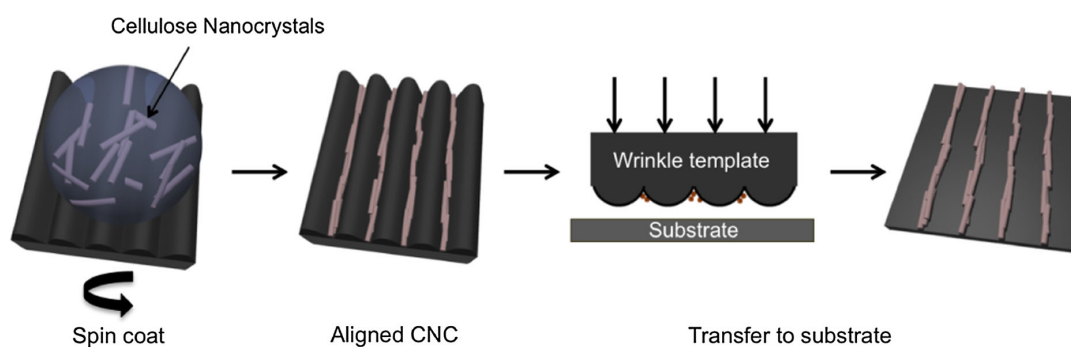


**Figure 1.14.** Schematic diagram showing the use of wrinkling technology to align cellulose nanocrystals using a water-mediated transfer process. Reproduced with permission from reference 123. Copyright © 2014, Springer Science Business Media Dordrecht.

## 1.4 Conclusions

Cellulose nanocrystals, a natural product, provide a path for increasing sustainability in several applications including re-inforcement of polymer matrices, drug delivery applications, production of iridescent films, *etc.* Their abundant hydroxyl groups provide potential for surface functionalization that can be used to tailor them for desired applications. The following thesis focuses on studying the application of cellulose nanocrystals in coating technologies. Utilising core concepts in physical and colloidal chemistry, we try to achieve nano-structured coatings using CNCs that are tailored for different applications. Inspired by the wrinkling technology to align cellulose nanocrystals, we follow the same process of aligning cellulose nanocrystals discussed by Nystrom, *et al.*<sup>[123]</sup> in Chapter 2, and try to achieve the efficient transfer of CNCs as well as robust aligned CNC surfaces on substrates with cationic polyelectrolytes. The application of such aligned CNC surfaces is examined in Chapters 3 and 4. A fundamental study into the stability of CNCs using salts and surfactants is presented in Chapter 1.

## 1.5 References

- [1] H. H. Nimz, *Eur. J. Wood Wood Prod.* **1984**, 42, 314-314.
- [2] H. Yang, R. Yan, H. Chen, D. H. Lee, C. Zheng, *Fuel* **2007**, 86, 1781-1788.
- [3] R. H. Marchessault, S. L. Malhotra, A. Y. Jones, A. Perovic, *Wood Agric. Residues*, Academic Press **1983**, 401-413.
- [4] T.-C. Chang, H.-T. Chang, C.-L. Wu, S.-T. Chang, *Polym. Degrad. Stab.* **2010**, 95, 516-521.
- [5] N. Gralen, S. The, *Nature* **1943**, 152, 625.
- [6] Y. Habibi, L. A. Lucia, O. J. Rojas, *Chem. Rev.* **2010**, 110, 3479-3500.



- [7] Z. Huang, V. S. Raghuwanshi, G. Garnier, *Front. Bioeng. Biotechnol.* **2017**, 5, 41.
- [8] R. H. Atalla, D. L. Vanderhart, *Science* **1984**, 223, 283-285.
- [9] A. F. Turbak, F. W. Snyder, K. R. Sandberg, *Microfibrillated cellulose, a new cellulose product: properties, uses, and commercial potential*, ; ITT Rayonier Inc., Shelton, WA, **1983**.
- [10] K. Dieter, K. Friederike, M. Sebastian, L. Tom, A. Mikael, G. Derek, D. Annie, *Angew. Chem. Int. Ed.* **2011**, 50, 5438-5466.
- [11] L. Wågberg, G. Decher, M. Norgren, T. Lindström, M. Ankerfors, K. Axnäs, *Langmuir* **2008**, 24, 784-795.
- [12] Y. Nishiyama, J. Sugiyama, H. Chanzy, P. Langan, *J. Am. Chem. Soc.* **2003**, 125, 14300-14306.
- [13] Y. Nishiyama, P. Langan, H. Chanzy, *J. Am. Chem. Soc.* **2002**, 124, 9074-9082.
- [14] G. I. Williams, R. P. Wool, *Appl. Compos. Mater.* **2000**, 7, 421-432.
- [15] K. Van de Velde, P. Kiekens, *Compos. Struct.* **2001**, 54, 355-360.
- [16] A. K. Bledzki, J. Gassan, *Angew. Makromol. Chem.* **1996**, 236, 129-138.
- [17] A. Alemdar, M. Sain, *Compos. Sci. Technol.* **2008**, 68, 557-565.
- [18] T. Zimmermann, N. Bordeanu, E. Strub, *Carbohydr. Polym.* **2010**, 79, 1086-1093.
- [19] W. Bei, S. Mohini, *Polym. Int.* **2007**, 56, 538-546.
- [20] K. Susheel, K. B.S., K. Inderjeet, *Polym. Eng. Sci.* **2009**, 49, 1253-1272.
- [21] S. Kalia, B. S. Kaith, S. Sharma, B. Bhardwaj, *Fibers Polym.* **2008**, 9, 416-422.
- [22] M. S. Sreekala, M. G. Kumaran, S. Joseph, M. Jacob, S. Thomas, *Appl. Compos. Mater.* **2000**, 7, 295-329.
- [23] D. Ray, B. K. Sarkar, A. K. Rana, N. R. Bose, *Bull. Mater. Sci.* **2001**, 24, 129-135.
- [24] S. J. Eichhorn, A. Dufresne, M. Aranguren, N. E. Marcovich, J. R. Capadona, S. J. Rowan, C. Weder, W. Thielemans, M. Roman, S. Renneckar, W. Gindl, S. Veigel, J.

- Keckes, H. Yano, K. Abe, M. Nogi, A. N. Nakagaito, A. Mangalam, J. Simonsen, A. S. Benight, A. Bismarck, L. A. Berglund, T. Peijs, *J. Mater. Sci.* **2009**, *45*, 1.
- [25] M. Pommet, J. Juntaro, J. Y. Y. Heng, A. Mantalaris, A. F. Lee, K. Wilson, G. Kalinka, M. S. P. Shaffer, A. Bismarck, *Biomacromolecules* **2008**, *9*, 1643-1651.
- [26] M. Shoda, Y. Sugano, *Biotechnol. Bioprocess Eng.* **2005**, *10*, 1.
- [27] S. J. Eichhorn, *Soft Matter* **2011**, *7*, 303-315.
- [28] A. Kumar, Y. S. Negi, V. Choudhary, N. K. Bhardwaj, *J. Mater. Phys. Chem.* **2014**, *2*, 1-8.
- [29] T. Koshizawa, *Jpn. TAPPI J.* **1960**, *14*, 455-458,475.
- [30] M. Usuda, O. Suzuki, J. Nakano, N. Migita, *J. Soc. Chem. Ind., Jpn.* **1967**, *70*, 349-352.
- [31] H. Sadeghifar, I. Filpponen, S. P. Clarke, D. F. Brougham, D. S. Argyropoulos, *J. Mat. Sci.* **2011**, *46*, 7344-7355.
- [32] J. Araki, M. Wada, S. Kuga, T. Okano, *J. Wood Sci.* **1999**, *45*, 258-261.
- [33] M. Roman, W. T. Winter, *Biomacromolecules* **2004**, *5*, 1671-1677.
- [34] N. Wang, E. Ding, R. Cheng, *Langmuir* **2008**, *24*, 5-8.
- [35] N. Wang, E. Ding, R. Cheng, *Polym.* **2007**, *48*, 3486-3493.
- [36] D. Bondeson, A. Mathew, K. Oksman, *Cellulose* **2006**, *13*, 171.
- [37] K. Oksman, M. Sain, *Cellulose Nanocomposites, Vol. 938*, American Chemical Society, **2006**, 2-8.
- [38] X. M. Dong, J.-F. Revol, D. G. GRAY, *Cellulose* **1998**, *5*, 19-32.
- [39] P. Lu, Y.-L. Hsieh, *Carbohydr. Polym.* **2010**, *82*, 329-336.
- [40] W. Li, J. Yue, S. Liu, *Ultrason. Sonochem.* **2012**, *19*, 479-485.
- [41] S. Cui, S. Zhang, S. Ge, L. Xiong, Q. Sun, *Ind. Crops Prod.* **2016**, *83*, 346-352.
- [42] Y. Tang, S. Yang, N. Zhang, J. Zhang, *Cellulose* **2014**, *21*, 335-346.

- [43] J. Guo, X. Guo, S. Wang, Y. Yin, *Carbohydr. Polym.* **2016**, *135*, 248-255.
- [44] W. Li, R. Wang, S. Liu, *BioResources* **2011**, *6*, 4259-4270.
- [45] Q. Lu, L. Tang, F. Lin, S. Wang, Y. Chen, X. Chen, B. Huang, *Cellulose* **2014**, *21*, 3497-3506.
- [46] H. Yu, Z. Qin, B. Liang, N. Liu, Z. Zhou, L. Chen, *J. Mater. Chem. A* **2013**, *1*, 3938-3944.
- [47] S. Camarero Espinosa, T. Kuhnt, E. J. Foster, C. Weder, *Biomacromolecules* **2013**, *14*, 1223-1230.
- [48] K. N. Mohd Amin, P. K. Annamalai, I. C. Morrow, D. Martin, *RSC Adv.* **2015**, *5*, 57133-57140.
- [49] V. Favier, H. Chanzy, J. Y. Cavaille, *Macromol.* **1995**, *28*, 6365-6367.
- [50] M. A. S. Azizi Samir, F. Alloin, J.-Y. Sanchez, A. Dufresne, *Polym.* **2004**, *45*, 4149-4157.
- [51] M. A. S. Azizi Samir, L. Chazeau, F. Alloin, J. Y. Cavaillé, A. Dufresne, J. Y. Sanchez, *Electrochim. Acta* **2005**, *50*, 3897-3903.
- [52] A. Junior de Menezes, G. Siqueira, A. A. S. Curvelo, A. Dufresne, *Polym.* **2009**, *50*, 4552-4563.
- [53] H. Qi, J. Cai, L. Zhang, S. Kuga, *Biomacromolecules* **2009**, *10*, 1597-1602.
- [54] L. Petersson, A. P. Mathew, K. Oksman, *J. Appl. Polym. Sci.* **2009**, *112*, 2001-2009.
- [55] S. Dong, M. Roman, *J. Am. Chem. Soc.* **2007**, *129*, 13810-13811.
- [56] M. L. Auad, M. A. Mosiewicki, T. Richardson, M. I. Aranguren, N. E. Marcovich, *J. Appl. Polym. Sci.* **2010**, *115*, 1215-1225.
- [57] I. Kvien, B. S. Tanem, K. Oksman, *Biomacromolecules* **2005**, *6*, 3160-3165.
- [58] J. K. Pandey, C. S. Lee, S. H. Ahn, *J. Appl. Polym. Sci.* **2010**, *115*, 2493-2501.

- [59] K. Shanmuganathan, J. R. Capadona, S. J. Rowan, C. Weder, *J. Mater. Chem.* **2010**, *20*, 180-186.
- [60] H. Liu, D. Liu, F. Yao, Q. Wu, *Bioresour. Technol.* **2010**, *101*, 5685-5692.
- [61] J. P. de Mesquita, C. L. Donnici, F. V. Pereira, *Biomacromolecules* **2010**, *11*, 473-480.
- [62] H. Wang, M. Roman, *Biomacromolecules* **2011**, *12*, 1585-1593.
- [63] J. K. Jackson, K. Letchford, B. Z. Wasserman, L. Ye, W. Y. Hamad, H. M. Burt, *Int. J. Nanomed.* **2011**, *6*, 321-330.
- [64] S. Dong, H. J. Cho, Y. W. Lee, M. Roman, *Biomacromolecules* **2014**, *15*, 1560-1567.
- [65] M. Hasani, E. D. Cranston, G. Westman, D. G. Gray, *Soft Matter* **2008**, *4*, 2238-2244.
- [66] M. Salajkova, L. A. Berglund, Q. Zhou, *J. Mater. Chem.* **2012**, *22*, 19798-19805.
- [67] H. Yuan, Y. Nishiyama, M. Wada, S. Kuga, *Biomacromolecules* **2006**, *7*, 696-700.
- [68] (a) Y. Habibi, H. Chanzy, M. R. Vignon, *Cellulose* **2006**, *13*, 679-687; (b) L. Jasmani, S. Eyley, C. Schütz, H. Van Gorp, S. De Feyter, W. Thielemans, *Cellulose* **2016**, *23*, 3569-3576; (c) S. Eyley, W. Thielemans, *Nanoscale* **2014**, *6*, 7764-7779.
- [69] T. Folda, H. Hoffmann, H. Chanzy, P. Smith, *Nature* **1988**, *333*, 55.
- [70] G. Oster, *J. Gen. Physiol.* **1950**, *33*, 445-473.
- [71] F. Livolant, A. Leforestier, *Prog. Polym. Sci.* **1996**, *21*, 1115-1164.
- [72] J. F. Revol, H. Bradford, J. Giasson, R. H. Marchessault, D. G. Gray, *Int. J. Biol. Macromol.* **1992**, *14*, 170-172.
- [73] J. Araki, S. Kuga, *Langmuir* **2001**, *17*, 4493-4496.
- [74] J. Araki, M. Wada, S. Kuga, T. Okano, *Langmuir* **2000**, *16*, 2413-2415.
- [75] D. Viet, S. Beck-Candanedo, D. G. Gray, *Cellulose* **2007**, *14*, 109-113.
- [76] J. F. Revol, R. H. Marchessault, *Int. J. Biol. Macromol.* **1993**, *15*, 329-335.
- [77] L. Heux, G. Chauve, C. Bonini, *Langmuir* **2000**, *16*, 8210-8212.
- [78] S. Beck, J. Bouchard, R. Berry, *Biomacromolecules* **2011**, *12*, 167-172.

- [79] R. Bardet, N. Belgacem, J. Bras, *ACS Appl. Mater. Interfaces* **2015**, 7, 4010-4018.
- [80] P. R. M., G. Giulia, W. C. A., Z. Tianheng, N. Aurimas, V. Silvia, F. P. Bruno, *Adv. Mater.* **2018**, 30, 1704477.
- [81] M. Roman, D. G. Gray, *Langmuir* **2005**, 21, 5555-5561.
- [82] W. J. Orts, L. Godbout, R. H. Marchessault, J. F. Revol, *Macromolecules* **1998**, 31, 5717-5725.
- [83] T. Ebeling, M. Paillet, R. Borsali, O. Diat, A. Dufresne, J. Y. Cavail  , H. Chanzy, *Langmuir* **1999**, 15, 6123-6126.
- [84] R. A. Chowdhury, S. X. Peng, J. Youngblood, *Cellulose* **2017**, 24, 1957-1970.
- [85] A. D. Haywood, V. A. Davis, *Cellulose* **2017**, 24, 705-716.
- [86] T. O'Connor, *Philos. Explor.* **2009**, 12, 119-125.
- [87] A. R. Reising, R. Moon, J. Youngblood, *J. Sci. Technol. For. Prod. Processes* **2012**, 2, 32-41.
- [88] P. J. Hyun, N. JungHyun, S. Christina, S. A. German, S. Giusy, B. Lennart, L. P. F. Jan, *ChemPhysChem* **2014**, 15, 1477-1484.
- [89] M. Alizadehgiashi, A. Khabibullin, Y. Li, E. Prince, M. Abolhasani, E. Kumacheva, *Langmuir* **2018**, 34, 322-330.
- [90] K. M. O. H  kansson, A. B. Fall, F. Lundell, S. Yu, C. Krywka, S. V. Roth, G. Santoro, M. Kvik, L. Prahl Wittberg, L. W  gberg, L. D. S  derberg, *Nat. Commun.* **2014**, 5, 4018.
- [91] C. Zhou, R. Chu, R. Wu, Q. Wu, *Biomacromolecules* **2011**, 12, 2617-2625.
- [92] L. Sanchez-Botero, A. V. Dimov, R. Li, D.-M. Smilgies, J. P. Hinestroza, *Langmuir* **2018**, 34, 5263-5272.
- [93] I. Hoeger, O. J. Rojas, K. Efimenko, O. D. Velev, S. S. Kelley, *Soft Matter* **2011**, 7, 1957-1967.

- [94] T. Pullawan, A. N. Wilkinson, S. J. Eichhorn, *Biomacromolecules* **2012**, *13*, 2528-2536.
- [95] D. Li, Z. Liu, M. Al-Haik, M. Tehrani, F. Murray, R. Tannenbaum, H. Garmestani, *Polym. Bull.* **2010**, *65*, 635-642.
- [96] P. Dhar, A. Kumar, V. Katiyar, *ACS Appl. Mater. Interfaces* **2016**, *8*, 18393-18409.
- [97] J. Sugiyama, H. Chanzy, G. Maret, *Macromol.* **1992**, *25*, 4232-4234.
- [98] F. Kimura, T. Kimura, M. Tamura, A. Hirai, M. Ikuno, F. Horii, *Langmuir* **2005**, *21*, 2034-2037.
- [99] J. Kim, Y. Chen, K.-S. Kang, Y.-B. Park, M. Schwartz, *J. Appl. Phys.* **2008**, *104*, 096104.
- [100] J.-F. Revol, L. Godbout, X.-M. Dong, D. G. Gray, H. Chanzy, G. Maret, *Liq. Cryst.* **1994**, *16*, 127-134.
- [101] C. D. Edgar, D. G. Gray, *Cellulose* **2001**, *8*, 5-12.
- [102] I. Kvien, K. Oksman, *Appl. Phys. A* **2007**, *87*, 641-643.
- [103] E. D. Cranston, D. G. Gray, *Sci. Technol. Adv. Mater.* **2006**, *7*, 319-321.
- [104] K. Yamamoto, S. Akita, Y. Nakayama, *Jpn. J. Appl. Phys.* **1996**, *35*, L917.
- [105] B. M. I. van der Zande, G. J. M. Koper, H. N. W. Lekkerkerker, *J. Phys. Chem. B* **1999**, *103*, 5754-5760.
- [106] J. Kerr, *London, Edinburgh Dublin Philos. Mag. J. Sci.* **1875**, *50*, 337-348.
- [107] D. Bordel, J.-L. Putaux, L. Heux, *Langmuir* **2006**, *22*, 4899-4901.
- [108] Y. Habibi, T. Heim, R. Douillard, *J. Polym. Sci., Part B: Polym. Phys.* **2008**, *46*, 1430-1436.
- [109] L. Csoka, I. C. Hoeger, P. Peralta, I. Peszlen, O. J. Rojas, *J. Colloid Interface Sci.* **2011**, *363*, 206-212.
- [110] B. Frka-Petesic, B. Jean, L. Heux, in *APS March Meeting Abstracts*, **2012**.

- [111] P. Munier, K. Gordeyeva, L. Bergström, A. B. Fall, *Biomacromolecules* **2016**, *17*, 1875-1881.
- [112] S. Huan, G. Liu, W. Cheng, G. Han, L. Bai, *Biomacromolecules* **2018**, *19*, 1037-1046.
- [113] W. Song, D. Liu, N. Prempeh, R. Song, *Biomacromolecules* **2017**, *18*, 3273-3279.
- [114] E. D. Cranston, D. G. Gray, *Colloids Surf., A* **2008**, *325*, 44-51.
- [115] J. Lefebvre, D. G. Gray, *Cellulose* **2005**, *12*, 127-134.
- [116] J. M. Dugan, J. E. Gough, S. J. Eichhorn, *Biomacromolecules* **2010**, *11*, 2498-2504.
- [117] E. D. Cranston, D. G. Gray, *Biomacromolecules* **2006**, *7*, 2522-2530.
- [118] B. Jean, F. Dubreuil, L. Heux, F. Cousin, *Langmuir* **2008**, *24*, 3452-3458.
- [119] Y. Habibi, I. Hoeger, S. S. Kelley, O. J. Rojas, *Langmuir* **2010**, *26*, 990-1001.
- [120] Y. Habibi, L. Foulon, V. Aguié-Béghin, M. Molinari, R. Douillard, *J. Colloid Interface Sci.* **2007**, *316*, 388-397.
- [121] C. Lu, H. Mohwald, A. Fery, *Soft Matter* **2007**, *3*, 1530-1536.
- [122] A. Schweikart, A. Horn, A. Böker, A. Fery, *Complex Macromolecular Systems I*, Springer Berlin Heidelberg, Berlin, Heidelberg, **2010**, pp. 75-99.
- [123] G. Nyström, A. B. Fall, L. Carlsson, L. Wågberg, *Cellulose* **2014**, *21*, 1591-1599.

## Preface for Chapter 2

This chapter focuses on the basic instruments and methods used for the thesis work. Among the different characterization techniques used, atomic force microscopy (AFM), contact angle measurements (CA) and dynamic light scattering systems (DLS) with a special insight to phase analysis light scattering (PALS) for zeta potential measurements will be discussed in detail. These instruments have been used extensively in the thesis work, and hence an understanding of their basic principles and operation is necessary. The actual measurement conditions for all techniques are mentioned in the chapters where they are used. The cellulose nanocrystals used in Chapter 3 were synthesised in our laboratory, and their full characterization is discussed therein. For the remaining Chapters, cellulose nanocrystals were purchased from University of Maine, US and their characterization and specifications are as follows:

- a) Appearance: white, odourless.
- b) Solid content: 11.5–12.5 wt% aqueous gel
- c) Fiber dimensions: 5–20 nm wide, 150–200 nm long
- d) Density: 1 g/cm<sup>3</sup> aqueous gel
- e) Surface property: hydrophilic



## Chapter 2: Methods and Instruments

### 2.1 Atomic force microscopy (AFM)

Atomic force microscopy (AFM) allows us to examine the surface morphology of samples under investigation, whether soft samples like human cells or hard samples like ceramic particles.<sup>[1]</sup> The technique employs a probe which scans over the surface to acquire the sample topography. A micro-machined cantilever with a sharp tip at the end constitutes the probe which interacts with the sample surface, and the position of the cantilever tip is monitored by a laser using the optical lever technique. Based on the cantilever displacement, precise measurements are carried out to determine the interaction between the sample and the tip apex. To preserve the tip-sample force at a constant level during imaging, a feedback control loop is applied. A number of different forces may be experienced by the cantilever tip such as Van der Waals forces, surface tension, electrostatic forces, *etc.*, based on the sample and tip interactions.<sup>[2]</sup> In order to image samples using AFM, it is very important to understand the different modes of AFM operation: primarily contact mode and oscillation modes (intermittent contact mode and non-contact mode).<sup>[3]</sup> In contact mode, the sample is in continual direct contact with the cantilever tip. Among all the topographic imaging modes used, contact mode serves as the fastest, as the topography of the sample is directly reflected by the deflection of the cantilever, where no analysis of oscillation measurements is required. However, contact mode suffers from certain limitations. The sample may get damaged easily due to the repulsive forces acting between the sample and the tip which may also damage the tip too. Lateral forces are experienced by both the sample and the probe, in addition to the normal forces experienced due to the direct contact of the tip with the sample. The main advantage in imaging in this mode is its high resolution compared to other modes. Contact mode is typically used to image samples with delicate structures where sub-molecular resolution is required.

To reduce the force between the probe and the sample during imaging, oscillating modes such as intermittent contact mode or tapping mode and non-contact mode is used. In this thesis, we use tapping mode to image cellulosic and polymeric substrates. In tapping mode, the tip-sample interaction forces reach a repulsive regime after passing through the zero-force and attractive (Van der Waals) regime as seen in **Fig. 2.1**. The feedback generally used in this mode is basic amplitude modulation. As the tip passes through the repulsive regime, it may be prone to contamination and can also become damaged. However, the lateral forces that affect imaging in contact mode do not affect tapping mode due to the minimal contact time between the tip and the surface. The oscillation of the tip occurs in an amplitude range of 1-100 nm.<sup>[3]</sup> Due to the intermittent contact of the sample with the tip, the amplitude is reduced from its free space value and hence the user sets up an amplitude set-point which determines how strongly the tip interacts with the surface. This imaging mode is widely used in imaging samples in air as well as in liquid.<sup>[3]</sup> From the AFM image captured, we can analyse several parameters including surface roughness, the dimensions of the sample such as the diameter of cellulose nanocrystals, perform Fourier transform analysis, *etc.*

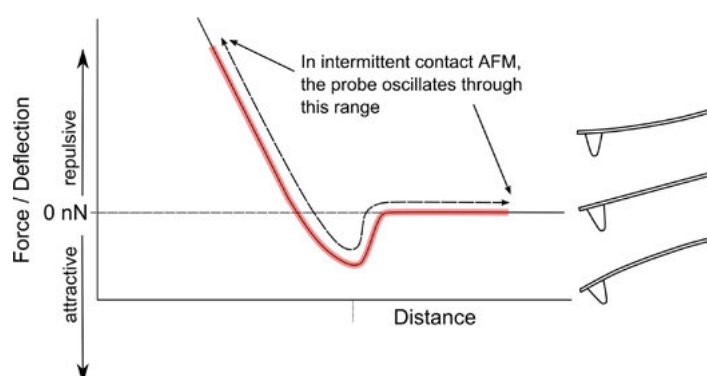


**Figure 2.1.** Force-distance curve of an AFM operating in tapping or intermittent contact mode. Reproduced with permission from reference 3. Copyright © 2018 Oxford University Press.

A typical AFM consists of three systems: a) computer software for data acquisition and processing; b) electronic controller that controls all the functions of the sample scanner using

electric signals, and c) control stage, comprising sample stage, optical microscope and scanner (**Fig. 2.2**).<sup>[4]</sup> A position sensitive photodiode detector receives a laser signal that is reflected from the back of the cantilever. This detector measures the bending of cantilever when either the tip is scanned over the sample (tip-scanning AFM), or the sample is scanned underneath a fixed cantilever (sample-scanning AFM). The response of the feedback control loop to the measured cantilever deflections are used to generate a map of the surface topography.

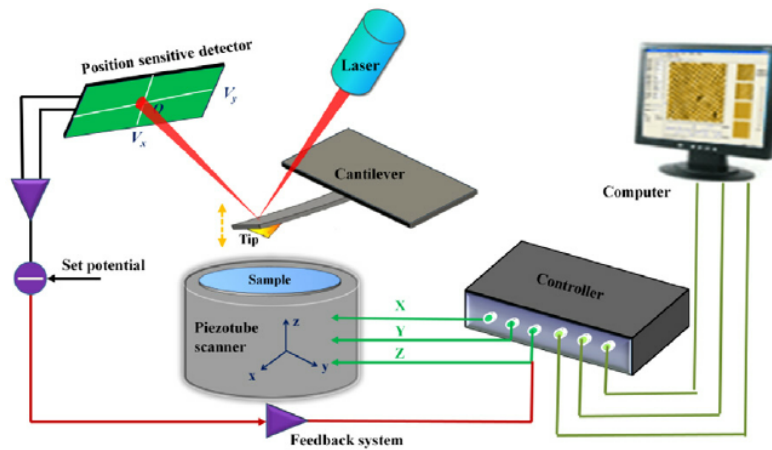


**Figure 2.2.** Schematic diagram of AFM instrumentation. Reproduced with permission from reference 4. Copyright © 2014 IOP Publishing Ltd.

The resolution of images using AFM can be  $\sim 0.1$  nm in usual conditions, which is far superior to scanning electron microscopy (SEM).<sup>[2]</sup> Cantilever tips are typically made of pure silicon, or silicon nitride. The tip-geometry (size and shape of its apex), oscillatory parameters like resonance frequency, cantilever stiffness and shape all affect the performance of the AFM probe, which is reflected in the end image.<sup>[5]</sup> The cantilever operates based on Hooke's law (**Equation 1**), wherein the cantilever acts as a spring.<sup>[6]</sup>

$$F = -kx \quad \text{(Equation 1)}$$

where  $k$  is the spring constant,  $x$  is the displacement of cantilever and  $F$  is the force acting on the cantilever. The cantilever bends in response to surface forces, and the deflection of the cantilever is then monitored.

## 2.2 Contact angle measurements (CA)

It is important to understand the basic principles behind contact angle measurements before understanding the instrumentation itself, so as to analyse the results in a concise manner. When a liquid drop comes in contact with a solid substrate, the angle measured through the droplet at the three phase contact line (where liquid, solid and vapour meet) is termed the contact angle, and is usually expressed in degrees ( $^{\circ}$ ).<sup>[7]</sup> The wettability of liquids on solid surfaces is governed by several factors including the chemical composition and geometrical structure of the substrate, surface roughness of the substrate, surface tension of the liquid used, droplet size, environmental conditions, *etc.*<sup>[7]</sup> Young's equation models the contact angle as:

$$\cos \theta_c = (\gamma_{SV} - \gamma_{SL})/\gamma_{LV} \quad \text{(Equation 2)}$$

where S, L, V represents the solid, liquid and vapour phase respectively,  $\gamma$  represents the surface energy and  $\theta_c$  represents the contact angle.<sup>[8]</sup>

When using water as the liquid for measuring contact angle, if  $\theta_c$  is greater than  $90^{\circ}$ , the surface is termed hydrophobic, meaning water-repelling.<sup>[9]</sup> If the  $\theta_c$  is greater than  $150^{\circ}$ , the surface is referred to as ultrahydrophobic or superhydrophobic.<sup>[10]</sup> Similarly, if  $\theta_c$  is less than  $90^{\circ}$ , the surface is referred to as hydrophilic<sup>[9]</sup> and the surface is termed as ultrahydrophilic or superhydrophilic,<sup>[10]</sup> if  $\theta_c \sim 0^{\circ}$ . Contact angle hysteresis (CAH) is a typical value measured

while analysing the wettability of different substrates. If the water moves on a substrate inclined at a certain angle, the front angle is termed the advancing ( $\theta_A$ ) angle and the angle formed at rear is termed the receding angle ( $\theta_R$ ). The contact angle hysteresis value is calculated as the difference between advancing and receding angles.<sup>[11]</sup> If CAH is high, the droplet tends to stick on the surface, whereas the droplets roll off when CAH is low.<sup>[12]</sup> Nevertheless, if the substrate is not inclined, it is possible to measure the CAH by growing a sessile droplet to calculate the advancing angle until the contact line moves; withdrawing the droplet allows us to obtain the receding angle. The dependence of contact angle value on the surface roughness is explained via two models: the Wenzel and Cassie Baxter models (**Fig. 2.3**).<sup>[13]</sup> According to the Wenzel model, the water droplet has intimate contact with the substrate and fully wets it at all points beneath the drop, wherein the surface roughness ( $r$ ) tends to be greater than unity according to the equation below:

$$\cos \theta_w = r \cos \theta \quad \text{(Equation 3)}$$

where  $\theta_w$  is the Wenzel contact angle,  $r$  is the surface roughness factor and  $\theta$  is the contact angle formed by the water droplet on a perfectly flat solid surface of the same material. According to Cassie-Baxter model, air is trapped between the water droplet and the micro-structured surface, thereby minimizing their interaction, and typically forming spherical droplets that experience low hysteresis values.

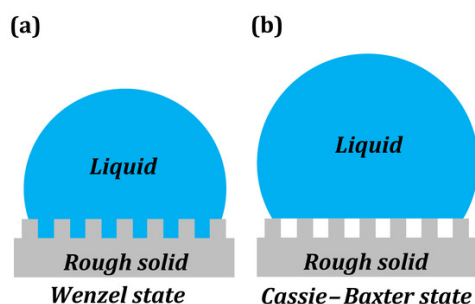


**Figure 2.3.** Wettability models explaining the dependence of contact angle on surface roughness: a) Wenzel state, and b) Cassie-Baxter state. Reproduced with permission from reference 13. Copyright @ MDPI open access.

The sessile drop analysis technique (**Fig. 2.4**) is the most commonly used method to measure the contact angle of liquids on substrates.<sup>[14]</sup> The method relies on measurement of the tangential angle at the three-phase intersection point of the liquid on the substrate surface. The measurement can be made using an automated system such as a goniometer, which employs a camera to view the droplet profile with the help of a background light source.<sup>[15]</sup> In this thesis work, we used both a commercial goniometer system as well as a customized set-up using an open source software named ‘Conan’ to measure contact angle. The substrate with the liquid droplet is first viewed using an imaging software known as Flycap<sup>[16]</sup> after which the tangent method of evaluating the contact angle is employed by running the Conan software. A rectangular box is drawn over the liquid with the substrate in contact, wherein the software automatically locates the droplet and substrate interfaces, and fits tangent lines as seen in **Fig. 2.4**. The method is very reliable and easy to use, especially when measuring the contact angle of biological fluids like blood, where evaporation can limit precise measurement of the contact angle. With the help of Conan software, captured images using Flycap could be run independently at any point in time, thereby facilitating quick and precise contact angle measurement. The needle used to dispense liquids may be hydrophobised using a suitable

organic silane reagent to avoid the liquid adhesion to the tip of the needle, rather favouring dispensing onto the substrate.

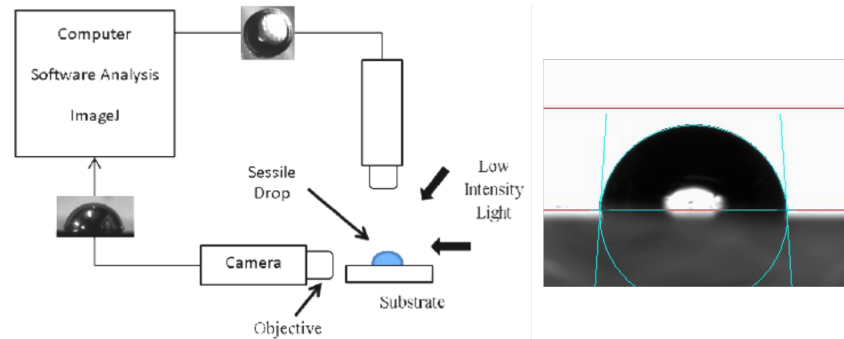


**Figure 2.4.** Sessile drop analysis technique (left side) for measuring contact angle of a liquid droplet on a solid substrate using tangent fitting (right side). Adapted from reference 14. Copyright © 2015 The Authors. Published by Elsevier Ltd.

### 2.3 Dynamic light scattering systems (DLS) - measuring zeta potential

Dynamic light scattering (DLS) facilitates the measurement of particle sizes down to 1 nm diameter, which makes it the most widely used among light scattering systems.<sup>[17]</sup> The technique is used in a wide range of applications including emulsions, colloids, proteins, *etc.*<sup>[18],[19]</sup> Fluctuations in the intensity of a laser beam scattered by the colloidal sample are detected by a photon detector at a particular scattering angle ‘ $\theta$ ’. The particle sizing is carried out using the Stokes-Einstein equation (**Equation 4**), in which the particle radius is calculated from the diffusion coefficient ‘ $D$ ’ of the particles undergoing Brownian motion obtained from the autocorrelation function, calculated by the instrument.<sup>[20]</sup>

$$D = \frac{k_B T}{6\pi\eta R} \quad \text{(Equation 4)}$$

$k_B$  is the Boltzmann constant,  $T$  is the temperature,  $\eta$  is the absolute viscosity and  $R$  is the hydrodynamic radius. The diffusion coefficient, ' $D$ ' is usually calculated by computing the intensity correlation function.<sup>[20]</sup> Incoming data is processed in real time with a digital signal processing device known as a correlator, and the autocorrelation function as a function of delay time,  $\tau$ , is extracted. The decay of this function is used to extract particle size. Faster decays correspond to smaller particles. It should be noted that the system assumes the particles to be spherical and sufficiently dilute as to be non-interacting, and hence the measurement of diffusion coefficient using auto correlation function is accurate only for truly dilute, non-interacting particles. DLS systems can also be employed to calculate the stability of colloidal systems using zeta potential measurements.<sup>[21]</sup>

To understand the significance of zeta potential, the basic concept of electrical double layer (**Fig. 2.5**) is required.<sup>[21]</sup> Surface charge is developed when a solid is immersed in an electrolyte solution. To neutralize the effect of these charges, counter ions of opposite charges are attracted by the surface, and are distributed non-homogeneously due to competing forces including entropic forces, Brownian motion and electrostatic forces. As the distance from the surface increases, the concentration of these counter ions decreases. Such inhomogeneous distribution of ions creates the so called electrical double layer, which consists of two layers: the Stern layer and the Gouy-Chapman layer (diffuse double layer), separated by the Helmholtz plane.<sup>[22]</sup> The electric potential drops linearly in the Stern layer, whereas beyond the Helmholtz plane, it decays gradually until the counter ions reach their average bulk concentration in the solvent. The slipping plane separates the tightly bound liquid layer from the bulk liquid. The potential measured at this slipping plane or shear plane under the influence of an electric field is termed the zeta potential.<sup>[23]</sup> Zeta potential modulates the colloidal stability of particle dispersions and is generally affected by the concentration of the particles used, the surface



charge of particles, pH, *etc.*<sup>[24]</sup> A colloidal particle system with a zeta potential value greater than  $\pm 25$  mV is generally considered to be stable.

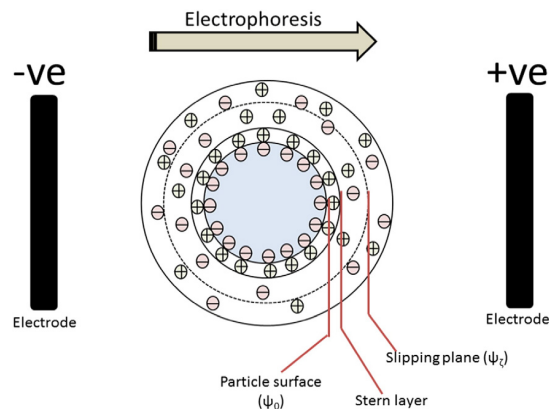


**Figure 2.5.** Schematic representation of electrical double layer developed during electrophoresis. Reproduced with permission from reference 21. Copyright © 2016 Elsevier B.V. All rights reserved.

A conventional zeta potential measuring instrument uses electrophoretic light scattering to evaluate the colloidal stability of particle dispersions.<sup>[25]</sup> Scattering of the laser illuminating the mobile particles occurs, resulting in a frequency shift ( $\Delta f$ ) of the original laser, which is proportional to the particle velocity ( $v$ ) at a particular wavelength of incident laser  $\lambda$  (**Equation 5**), known as a Doppler shift.<sup>[26]</sup>

$$\Delta f = 2v \sin\left(\frac{\theta}{2}\right)/\lambda \quad (\text{Equation 5})$$

To determine the Doppler shift, scattered light from the sample is combined with a reference beam. Zeta potential ( $\zeta$ ) is then calculated (**Equations 6 and 7**) by measuring the particle velocity ( $v$ ), deduced from this Doppler shift.<sup>[27]</sup> In a phase-analysis light scattering system (PALS), an additional frequency shift is made by applying phase modulation to the reference beam.<sup>[28]</sup> In PALS, the phase shift is measured instead of the frequency shift, which is

proportional to the displacement of the particles. The PALS technique is 100 times more sensitive compared to the use of other electrophoretic measurement techniques.<sup>[29]</sup> Samples of high conductivity, where the risk of Joule heating is high, can be carefully handled by the PALS system, wherein only low voltages are applied for measurements.<sup>[30]</sup> Also, samples with high viscosity and low particle mobility can be accurately measured using PALS. The electrophoretic mobility,  $\mu_e$  is calculated by measuring the particle velocity ( $v$ ) under the influence of electric field,  $E$  as shown in **Equation 6**.

$$\mu_e = \frac{v}{E} \quad \text{(Equation 6)}$$

**Equation 7** is known as Smoluchowski equation and is applied for the calculation of zeta potential where the double layer thickness is far less than the particle radius.<sup>[27]</sup>

$$\mu_e = \epsilon_r \epsilon_o \zeta / \eta \quad \text{(Equation 7)}$$

where  $\epsilon_r, \epsilon_o$  are the relative and vacuum permittivities respectively and  $\eta$  is the viscosity. The Smoluchowski theory is a very good approximation for highly charged systems with short Debye length, but may break down for very low charges and large Debye length systems. It is however the most appropriate approximation model to use here, as other variations are highly contentious, and a complete analytical solution does not yet exist.

A Brookhaven Zeta PALS system (**Fig. 2.6**) uses a laser beam, which is split into a reference beam and a scattering beam.<sup>[28]</sup> The reference beam is then processed by a piezo-modulator, where phase modulation is carried out across the frequency range 62.5-2000 Hz. The phase modulated reference beam is then combined with the scattered beam, forming a homodyne signal. The homodyne signal generated is detected by a photomultiplier and then

passes through a data buffer, where the phase analysis is carried out. The signal passed through the data buffer can also be analysed for particle size using a digital correlator.

In order to perform the physical measurement, an electrode plugged into a cell is carefully immersed in the sample solution, which creates a reversible electric field in the colloidal dispersion. For conductive colloidal dispersions, palladium electrodes are preferably used. A host PC is connected to the above-mentioned set-up that controls the whole instrument. An additional electronic module containing a slave digital signal processor is used for the phase analysis. From the measured zeta potential (approximating the surface potential,  $\psi_o$ , as the slipping plane is assumed to be close in proximity to the Stern layer for the colloidal system under investigation) using electrophoretic mobility  $\mu_e$ , the surface charge density,  $\sigma$  of the colloidal particles can be calculated using Grahame's equation,<sup>[31]</sup> shown below:

$$\sigma = \sqrt{8c_o \epsilon_o \epsilon_r RT} \sinh\left(\frac{ze\psi_o}{2k_B T}\right) \quad \text{(Equation 8)}$$

where  $c_o$  is the bulk electrolyte concentration,  $R$  is the gas constant,  $T$  is the absolute temperature,  $z$  is valence of the ion,  $e$  is the fundamental charge and  $\psi_o$  is the surface potential. Grahame's equation is derived from Gouy-Chapman theory<sup>[22]</sup> by assuming the electro-neutrality condition, which states that the total charge of the double-layer must be equal to the negative charge of the surface charge.

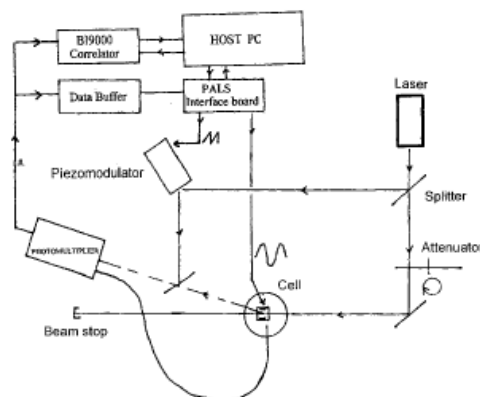


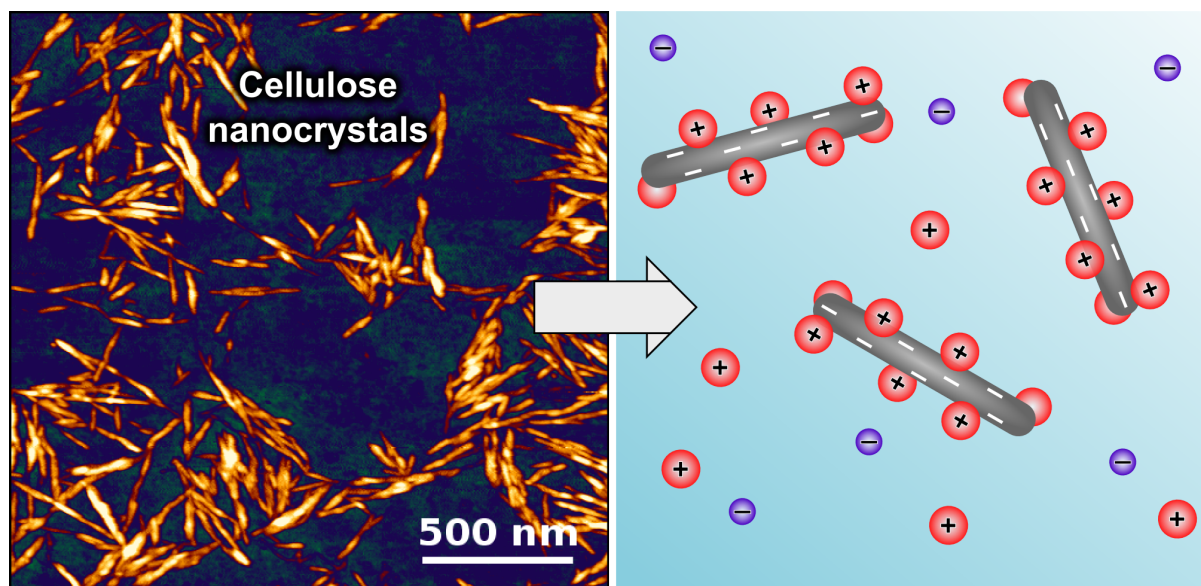
**Figure 2.6.** Schematic representation of the instrumentation of the Brookhaven Zeta PALS system. Reproduced with permission from reference 28. Copyright © 2001 Optical Society of America.

## 2.4 References

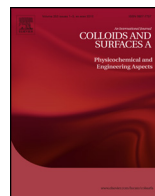
- [1] G. Binnig, C. F. Quate, C. Gerber, *Phys. Rev. Lett.* **1986**, *56*, 930-933.
- [2] S. Alexander, L. Hellemans, O. Marti, J. Schneir, V. Elings, P. K. Hansma, M. Longmire, J. Gurley, *J. Appl. Phys.* **1989**, *65*, 164-167.
- [3] P. Eaton, P. West, *Atomic Force Microscopy*, Oxford University Press, USA, **2010**.
- [4] G. Dan, X. Guoxin, L. Jianbin, *J. Phys. D: Appl. Phys.* **2014**, *47*, 013001.
- [5] S. J. O'Shea, M. E. Welland, *Langmuir* **1998**, *14*, 4186-4197.
- [6] A. E. Moyer, *Isis* **1977**, *68*, 266-275.
- [7] P. Ragesh, V. Anand Ganesh, S. V. Nair, A. S. Nair, *J. Mater. Chem. A* **2014**, *2*, 14773-14797.
- [8] R. J. Good, *J. Adhes. Sci. Technol.* **1992**, *6*, 1269-1302.
- [9] S. H. Lee, P. J. Rossky, *J. Chem. Phys.* **1994**, *100*, 3334-3345.
- [10] S. Taolei, W. Guojie, F. Lin, L. Biqian, M. Yongmei, J. Lei, Z. Daoben, *Angew. Chem.* **2004**, *116*, 361-364.
- [11] T. D. Blake, J. M. Haynes, *Prog. Surf. Membr. Sci.* **1973**, *6*, 125-138.
- [12] Z. Yoshimitsu, A. Nakajima, T. Watanabe, K. Hashimoto, *Langmuir* **2002**, *18*, 5818-5822.
- [13] R. Ramachandran, M. Nosonovsky, *Biomimetics* **2016**, *1*, 4.
- [14] J. M. Schuster, C. E. Schvezov, M. R. Rosenberger, *Procedia Mater. Sci.* **2015**, *8*, 742-751.

- [15] D. Y. Kwok, T. Gietzelt, K. Grundke, H. J. Jacobasch, A. W. Neumann, *Langmuir* **1997**, *13*, 2880-2894.
- [16] J. C. Ramirez-San-Juan, C. Regan, B. Coyotl-Ocelotl, B. Choi, *J. Biomed. Opt.* **2014**, *19*, 106009.
- [17] H. Xie, K. L. Gill-Sharp, D. P. O'Neal, *Nanomedicine* **2007**, *3*, 89-94.
- [18] D. G. Dalgleish, F. R. Hallett, *Food Res. Int.* **1995**, *28*, 181-193.
- [19] B. Jachimska, M. Wasilewska, Z. Adamczyk, *Langmuir* **2008**, *24*, 6866-6872.
- [20] M. Kaszuba, D. McKnight, M. T. Connah, F. K. McNeil-Watson, U. Nobbmann, *J. Nanopart. Res.* **2008**, *10*, 823-829.
- [21] S. Bhattacharjee, *J. Controlled Release* **2016**, *235*, 337-351.
- [22] K. B. Oldham, *J. Electroanal. Chem.* **2008**, *613*, 131-138.
- [23] H. Ohshima, *Colloids Surf., A* **1995**, *103*, 249-255.
- [24] S. Patil, A. Sandberg, E. Heckert, W. Self, S. Seal, *Biomaterials* **2007**, *28*, 4600-4607.
- [25] T. Toshio, *Electrophoresis* **1993**, *14*, 1255-1256.
- [26] Y. Takeda, *Int. J. Heat Fluid Flow* **1986**, *7*, 313-318.
- [27] A. Sze, D. Erickson, L. Ren, D. Li, *J. Colloid Interface Sci.* **2003**, *261*, 402-410.
- [28] W. W. Tscharnuter, *Appl. Opt.* **2001**, *40*, 3995-4003.
- [29] J. D. Clogston, A. K. Patri, *Characterization of Nanoparticles Intended for Drug Delivery* (Ed.: S. E. McNeil), Humana Press, Totowa, NJ, **2011**, 63-70.
- [30] F. McNeil-Watson, W. Tscharnuter, J. Miller, *Colloids Surf., A* **1998**, *140*, 53-57.
- [31] I. Borukhov, D. Andelman, H. Orland, *Phys. Rev. Lett.* **1997**, *79*, 435-438.

## Preface for Chapter 3



In this Chapter, we explore the fundamental stability of cellulose nanocrystals (CNCs) using zeta potential measurements in different pH and electrolyte conditions. To develop an understanding of the effects of ion identity on CNC stability, we used salts of different types: ionic and hydrophobic salts along with cationic and anionic surfactants. Another aspect of the study focuses on engineering the cast CNC film, investigating the relation between the surface roughness and their zeta potential. The salt amount versus surface groups with  $\text{Ca}^{2+}$  corresponds to 10 000, 125, 17 and 4 ions per charge for  $\text{Ca}^{2+}$  concentrations of 0.1 M, 0.01 M, 0.001 M and 0.0001 M respectively. We find significantly more  $\text{Ca}^{2+}$  ions than surface charge, hence no bridging effect of  $\text{Ca}^{2+}$  ions occur, explaining the perhaps unexpected levels of stability in this divalent salt.



# Modulating the zeta potential of cellulose nanocrystals using salts and surfactants



Ragesh Prathapan<sup>a</sup>, Rajiv Thapa<sup>a</sup>, Gil Garnier<sup>b,\*</sup>, Rico F. Tabor<sup>a,\*</sup>

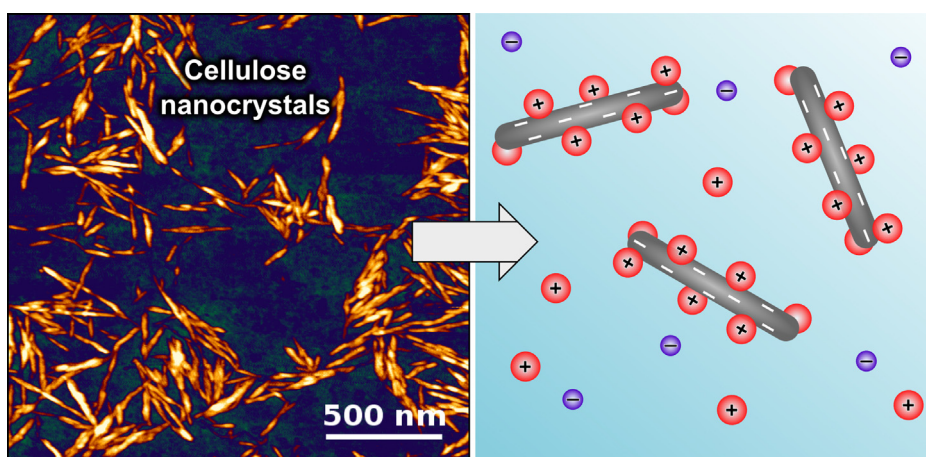
<sup>a</sup> School of Chemistry, Monash University, Clayton, VIC 3800, Australia

<sup>b</sup> Bioreources Processing Research Institute of Australia (BioPRIA), Department of Chemical Engineering, Monash University, Clayton, VIC 3800, Australia

## HIGHLIGHTS

- Zeta potential of cellulose nanocrystals is explored as a function of additives.
- Hofmeister-type specific ion effects modulate ion adsorption.
- Surfactant adsorption can increase or reverse surface charge.
- Film roughness from cellulose nanocrystals depends on suspension zeta potential.

## GRAPHICAL ABSTRACT



## ARTICLE INFO

### Article history:

Received 18 June 2016

Received in revised form 26 August 2016

Accepted 28 August 2016

Available online 30 August 2016

### Keywords:

Nanocellulose crystals (NCC)

Zeta potential

Colloidal stability

Hofmeister effect

Film roughness

## ABSTRACT

The zeta potential of cellulose nanocrystal (CNC) aqueous dispersions was studied as a function of solution conditions, including changing pH and different electrolyte identities and concentrations. A range of electrolytes that spans typical Hofmeister/hydrophobic effects was explored, along with both cationic and anionic surfactants. A subtle interplay of electrostatic and hydrophobic effects in ion adsorption was uncovered, including evidence of charge reversal and supercharging when hydrophobic surfactants are added to aqueous CNC dispersions. The apparent effects of zeta potential on dispersion stability were explored by using atomic force microscopy (AFM) to determine the roughness of resulting CNC films. The root mean square roughness (RMS) of these cellulose films was unaffected by the presence of surfactants (achieving a constant value of  $\sim 9$  nm), but scaled inversely and non-linearly with the zeta potential of the CNC suspension while using the ionic salts from  $\sim 2$  nm to 10 nm, indicating a facile method for the control of cellulose film roughness.

© 2016 Elsevier B.V. All rights reserved.

**Abbreviations:** NCC, nanocellulose crystals; AFM, atomic force microscopy; RMS, root mean square; MCC, microcrystalline cellulose; cmc, critical micelle concentration.

\* Corresponding authors.

E-mail addresses: [ragesh.prathapan@monash.edu](mailto:ragesh.prathapan@monash.edu) (R. Prathapan), [rajiv.thapa@monash.edu](mailto:rajiv.thapa@monash.edu) (R. Thapa), [gil.garnier@monash.edu](mailto:gil.garnier@monash.edu) (G. Garnier), [rico.tabor@monash.edu](mailto:rico.tabor@monash.edu) (R.F. Tabor).

<http://dx.doi.org/10.1016/j.colsurfa.2016.08.075>

0927-7757/© 2016 Elsevier B.V. All rights reserved.



## 1. Introduction

Cellulosic nanomaterials – including cellulose nanocrystals (CNC), cellulose nanofibres (CNF) [1,2] along with their composites are promising materials for many novel applications [3–5] owing to their unique properties that include excellent mechanical strength [6], self-assembly, liquid crystalline behavior [7,8] and optical properties ranging from transparent to translucent [9]. Controlled acid hydrolysis of native cellulose sources using sulfuric acid is commonly used to synthesise rod-shaped cellulose nanocrystals [10], which are electrostatically stabilized [11] by the sulfate ester moieties [12] on their surfaces. The acid hydrolysis typically results in the formation of cellulose nanocrystals of width 5–10 nm and length 100–300 nm [13].

In aqueous handling of colloidal dispersions, the electrical-double layer [14] is a key feature controlling stability; the extent of the electrical double-layer – modulated by particle surface charge and screening effects – is much affected by the concentration of counter-ions and the nature of the electrolytes used. This important component in the colloidal stability of aqueous suspensions can be determined by zeta potential measurements [15,16]. However, the addition of salts and electrolytes may also affect the amount and distribution of charge on particle surfaces, and even the hydrophobic/hydrophilic ratio, depending on the nature of the salt added [17].

Several studies have reported the effect of added salt concentration on the colloidal stability of CNC. For example, Zhong et al. [18] studied the effect of simple electrolytes like NaCl and  $\text{CaCl}_2$  on the colloidal stability of CNC. They showed that the zeta potential of CNC became less negative upon addition of  $\text{Na}^+$  and  $\text{Ca}^{2+}$  counter-ions, attributed to an electrostatic screening effect. They also studied the effect of anionic surfactants like sodium dodecyl sulfate (SDS) and polymers such as sodium carboxymethyl cellulose (NaCMC) on the zeta potential of CNC, and found that the zeta potential became more negative. Yu et al. [19] highlighted that polymer concentration, ionic strength and pH influence the colloidal stability when studying polystyrene sulfate latex particles with comparable surface chemistry. Dhar, Au, Berry & Tam [20] studied the interaction between CNC and tetradecyltrimethylammonium bromide (TTAB) – a cationic surfactant. Upon increasing the TTAB concentration, a charge reversal from negative to positive was observed. Jackson et al. [21] studied the effect of another cationic surfactant, CTAB (cetyltrimethylammonium bromide) concentration on the zeta potential of CNC. At higher CTAB concentrations, flocculation was observed, indicating a clear interaction between CTAB and CNC. The binding interaction between CNC and CTAB was also confirmed by the increasingly positive zeta potential of CNC upon increasing the CTAB concentration. A cationic substituent EPTMAC (2,3-epoxypropyl-trimethylammonium chloride) was used to surface functionalize CNC, yielding cationic hydroxypropyl-trimethylammonium chloride groups on the CNC surface [22]. After treatment with EPTMAC, a charge reversal from –39 mV to +30 mV was observed in the CNC zeta-potential.

From these studies, a complex picture emerges in which salt and surfactant interactions can have varied roles on the dispersion stability of CNC, motivating a systematic study to account for the effects at play. In this work, the primary objective is to systematically quantify and understand the effect that salt identity and concentration has on the zeta potential of CNC dispersions. The salt characteristics of most interest are the valency, charge and hydrophobicity of the ions. The second objective is to determine the importance that CNC zeta potential has on engineering applications – specifically film formation. For this study, we examine the effect of CNC zeta potential on the roughness of cellulose films formed by spin coating CNC suspensions of various inherent zeta potential.

## 2. Experimental

### 2.1. Materials

Sodium chloride (NaCl), calcium chloride ( $\text{CaCl}_2 \cdot 2\text{H}_2\text{O}$ ), potassium iodide (KI) and anhydrous sodium acetate (NaOAc) were from Merck (analysis grade) and used as received. Tetramethylammonium bromide (reagent grade) was from Sigma-Aldrich, and cetyltrimethylammonium bromide (CTAB, >99%) and sodium dodecyl sulfate (SDS, >90%) were purchased from ChemSupply, SA and used as received. For pH adjustment, sodium hydroxide (NaOH, 99%) and hydrochloric acid (HCl) were used. For the preparation of cellulose nanocrystals, microcrystalline cellulose (MCC, type 101, Sigma-Aldrich) was used along with sulfuric acid (95–98%). Water used was from a Millipore Direct-Q 5, with a minimum resistivity of 18.4 M $\Omega$  cm.

### 2.2. CNC preparation

Preparation of CNC was performed as per the method described by Bondeson, Mathew & Oksman [23]. Firstly, 2 g of microcrystalline cellulose was dispersed in 22.5 mL deionized (DI) water. The suspension was then placed in an ice bath with stirring for about 10–15 min at 500 rpm. Drop-wise addition of sulfuric acid (21.5 mL) was made to the above suspension, after which it was heated to 45 °C, and maintained at this temperature with stirring for 2 h at 500 rpm. The suspension was diluted with cold water (200 mL) to quench the reaction. Using centrifugation (30 min, 5000 rpm, 20 °C), the solid was isolated and resuspended in 50 mL DI water. Repeated centrifugations followed by ultrasonication (Digitech, 100 W ultrasonic cleaner) in between were carried out so as to isolate the CNC from dissolved impurities. For further purification, dialysis (regenerated Fisher brand cellulose dialysis membrane, with molecular weight cut off 12,000–14,000 Da) of recovered supernatants against distilled water was carried out for 5–6 days at room temperature. The water used for dialysis was changed every 6 h. Ultrasonication of the resultant colloidal dispersion was used to ensure full redispersion, and the CNC were then freeze-dried (FreeZone Plus 4.5) for 4–5 days to obtain the solid CNC. For zeta potential measurements, 1 mg mL<sup>–1</sup> of freeze-dried CNC was redispersed in the required solution via ultrasonication. For AFM measurements, the pre freeze-dried CNC (concentration 0.53 mg mL<sup>–1</sup>) was used.

### 2.3. Instrumentation techniques

Zeta potential of CNC dispersions was measured using the phase analysis light scattering (PALS) mode on a dynamic light scattering system (DLS, NanoBrook Omni, Brookhaven Corporation). The pH of the suspensions was examined before and after measurements, and HCl and NaOH were used to adjust the pH to required values. Atomic force microscopy (AFM, JPK Nanowizard 3) was used (in alternating contact, AC mode) to obtain images of CNC morphology, along with particle size and root mean square (RMS) roughness analysis. For obtaining the particle size of the CNC, 200 individual crystals were analysed, and the average length and height (i.e. thickness) was calculated. To explore the chemical functionality and crystallinity of the synthesised CNC, Fourier transform infrared spectroscopy (Cary 630 FTIR, Agilent technologies) and powder X-ray diffraction (Eco D8 Advance, Bruker) were used. For FTIR measurements, the single-reflection diamond attenuated total reflectance (ATR) sampling accessory of the instrument was used. The spectra shown are an average of 20 scans; no further manipulation of the data was made. The powder X-ray spectra were collected using a 1 kW Cu source and SSD160 ultrafast 1-dimensional detector; the source



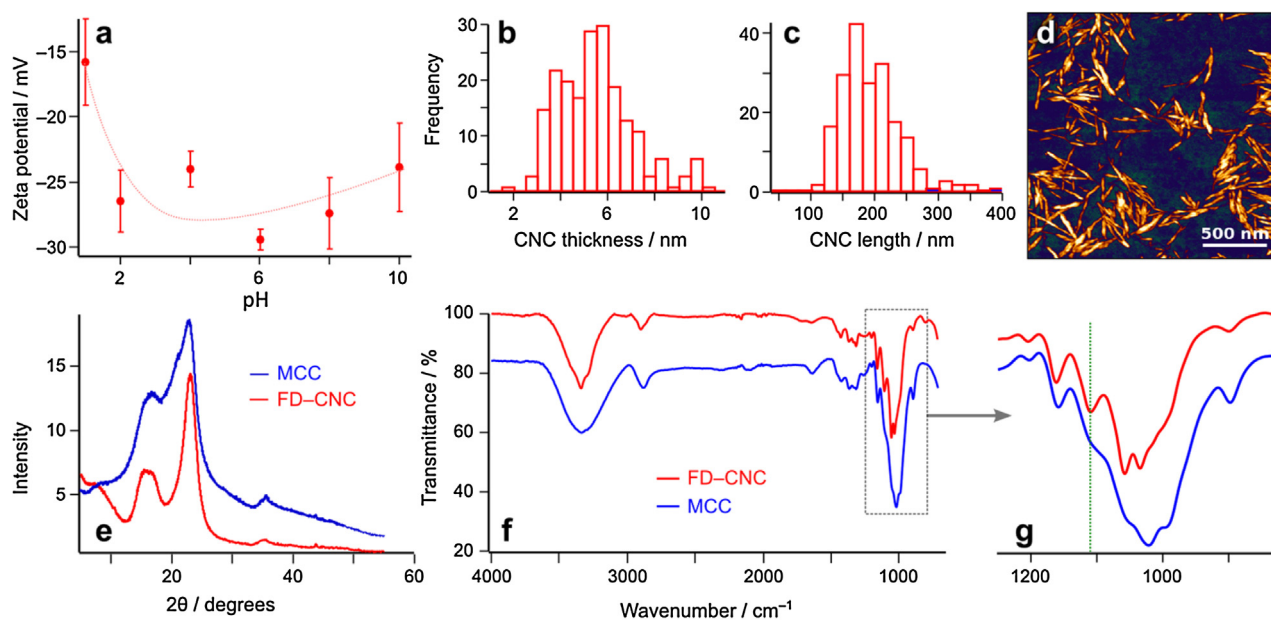


**Fig. 1.** (a) The effect of pH on the zeta potential of CNC; no background electrolyte was added, so the ionic strength of these samples arises from the pH determining ions. (b and c) Width and length histograms of CNC (sample size  $n = 200$ ). (d) AFM image of pre freeze-dried CNC. (e) XRD comparison of freeze-dried CNC and precursor MCC. (f) FTIR-ATR comparison of MCC and freeze-dried (FD) CNC. (g) The expanded axis of dotted region of (f) showing the region in which the typical stretching vibration due to sulfate moieties is seen.

wavelength was 0.154 nm and the goniometer was driven at a rate of  $0.5^\circ \text{ min}^{-1}$ .

#### 2.4. AFM sample preparation

Glass microscope slides (1.0–1.2 mm thick) were first cleaned thoroughly in DI water, then ethanol, and finally in a UV-ozone chamber (PSD series, Digital UV-ozone, Novascan, 120 min) so as to degrade any organic contaminants. The colloidal suspensions were coated onto these slides using a spin coater (Laurell technologies, WS-400BZ-6NPP/LITE) at 2000–2300 rpm for 1 or 2 min.

### 3. Results and discussions

To ensure the crystalline nature of CNC produced by acid hydrolysis, powder X-ray diffraction (XRD) was carried out, and to explore the chemical groups present within the CNC, Fourier transform infrared spectroscopy (FTIR) in attenuated total reflectance (ATR) mode was used. For both freeze dried CNC and the precursor microcrystalline cellulose (MCC), similar FTIR spectra (Fig. 1f and g) were observed. The main characteristic stretching vibrations found common to both of them are: O–H stretching vibrations in the range  $3600\text{--}3000 \text{ cm}^{-1}$ ; C–H stretching at  $2900 \text{ cm}^{-1}$ ; –C–6  $\text{CH}_2$ – bending near  $1400 \text{ cm}^{-1}$  and out-of plane bending near  $700 \text{ cm}^{-1}$ . The spectral features that separate the two samples however are the stretching attributed to sulfate moieties near  $1100 \text{ cm}^{-1}$ , found in CNC, and the stretching corresponding to water adsorption near  $1600 \text{ cm}^{-1}$  in MCC. These observations were consistent with the results reported by Lu and Hsieh [24]. From the XRD results (Fig. 1e), the characteristic peaks for crystalline cellulose corresponding to  $2\theta$  values of  $10^\circ$ ,  $17^\circ$  and  $26^\circ$  were seen. Tellingly, the peaks were more sharply resolved for CNC compared to MCC, which is expected given the presence of amorphous cellulose in the latter. Peak width has been shown previously by Garvey et al. to be related to the lateral dimension of cellulose fibres [25], although this effect would not fully explain the spectra seen here. From the diffraction data it is also theoretically possible to assign the cellulose allomorph present in the precursor microcrystalline cellulose sample. According to

the idealized X-ray powder diffraction patterns provided by French [26], the data here correspond most closely with the Iβ allomorph when randomly oriented.

An atomic force microscopy (AFM) height image of the pre-freeze dried CNC deposited at low concentration demonstrated the presence of well-resolved, individual crystals (Fig. 1d). From topographical information obtained using the AFM, size analysis of the pre freeze-dried CNC samples was carried out. For this, 200 individual crystals were analyzed using AFM, and their length and width values were calculated, as displayed in the histograms seen in Fig. 1b and Fig. 1c. The measured height from AFM imaging was used to determine their width (thickness) to avoid tip convolution effects due to their small dimensions. The average length and width of the CNC were found to be 175 nm and 5 nm, respectively. From these values and assuming an average cellulose density of  $1.5 \text{ g cm}^{-3}$ , the specific surface area was calculated to be on the order of  $465 \text{ m}^2 \text{ g}^{-1}$ , which is within the range reported in literature [27].

As a benchmark with which to contextualise the effects of different additives on CNC zeta potential, the effect of pH on the zeta potential of cellulose nanocrystals (CNC) aqueous suspensions was first measured (Fig. 1a). The pH was controlled by HCl or NaOH addition. Varying pH across a wide range from 2 to 10 (and ionic strength, in these measurements arising only from the pH-determining ions) had little effect on CNC zeta potential. However at pH 1, a considerable reduction in zeta potential was observed. As the  $\text{pK}_a$  of the covalently bound sulphate ester groups is very low ( $\text{pK}_a = 1.9$ ) [12], the change in pH (in the range of 2–10) does not significantly alter their dissociation state and they remain almost fully dissociated. However at pH 1, protonation of the sulfonic acids starts to occur, decreasing the net charge on the CNC surfaces, which is reflected as a decrease in the magnitude of the zeta potential. Throughout the study, we use the Smoluchowski equation to calculate zeta potential,  $\zeta$  from electrophoretic mobility,  $\mu$  [14]:

$$\mu = \frac{\epsilon \epsilon_0 \zeta}{\eta}$$

where  $\epsilon$  and  $\epsilon_0$  are the relative and vacuum permittivities respectively and  $\eta$  is the viscosity. Although some small deviation in the Henry factor could be expected at the lowest electrolyte

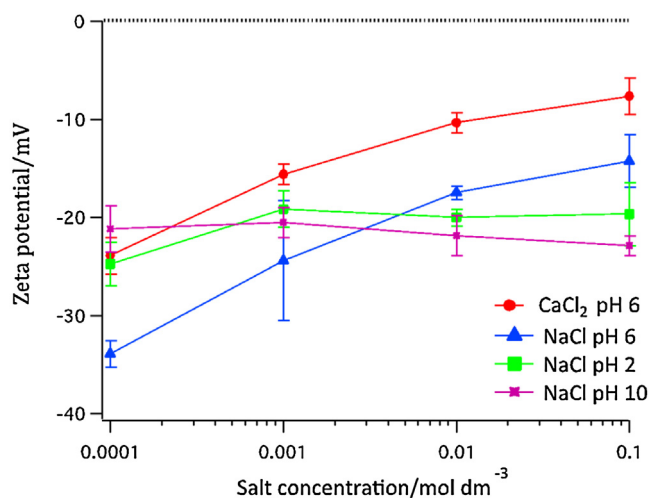


**Fig. 2.** The effect of NaCl and  $\text{CaCl}_2$  concentration on the zeta potential of CNC at different pH conditions. Calculated ionic strengths and Debye lengths at which these data were obtained are presented in Supplementary material. Measurements were carried out at a pH of 6.

concentrations used [28], this choice is maintained for consistency. This also facilitates better understanding the relationship between changes in surface potential/charge density and the measured zeta potential, especially as compression of the electrical double-layer and knowledge of the location of the slipping plane becomes important.

The effect of simple ionic electrolytes on CNC stability (Fig. 2) was explored, showing a gradual reduction in the zeta potential with increasing salt concentration (both  $\text{Na}^+$  and  $\text{Ca}^{2+}$  ions). This is because the Debye-Huckel screening strength is increased upon increasing the salt concentration and therefore the Debye length decreases. This encourages adsorption of ions and ion pairs to the CNC surface and the increase in adsorption of ions is directly facilitated by the compression of the double layer. As expected,  $\text{Ca}^{2+}$  ions showed more screening strength than  $\text{Na}^+$  ions, as seen by a greater reduction in CNC zeta potential. A similar study on the effect of divalent counterions on the electrophoretic mobility of sulfate latex particles showed a reduction in absolute mobility with an increase in concentration of divalent counterions [29]. However, the effect of the divalent ion for CNCs was significantly less dramatic than expected from, for example the Schulze-Hardy prediction [14].

To determine the interplay of pH and electrolyte effects, the effect of  $\text{Na}^+$  ions at low (pH 2) and high pH (pH 10) was studied (Fig. 2). There is considerably less change in zeta potential when the pH of the CNC/NaCl solution is significantly acidic or basic. This may be due to a constant potential condition arising with change in surface charge density so as to maintain ion adsorption equilibrium [30]. The contribution of the  $\text{Na}^+$  and  $\text{Cl}^-$  used to control pH (from NaOH and HCl) are expected to play a negligible role, except in determining the ionic strength of the medium. In each case, the increased overall ionic strength results in a significantly compressed double-layer – as evidenced by the much shorter Debye lengths, on the order of 3 nm or less for NaCl experiments at pH 2 – see Supplementary material.

To understand whether any specific ion effects exist for CNCs, in addition to the simple electrolyte effects explored above, the effect of hydrophobic anions and cations on the zeta potential of CNC suspensions was studied (Fig. 3). We assume that the surface charge of CNCs is dominated by the covalent sulphate ester groups on the CNC surfaces, which have a very low  $\text{pK}_a$  value and are therefore dissociated down to extremely low pH values. This is corroborated by the insensitivity of the measured zeta potential to pH when salts

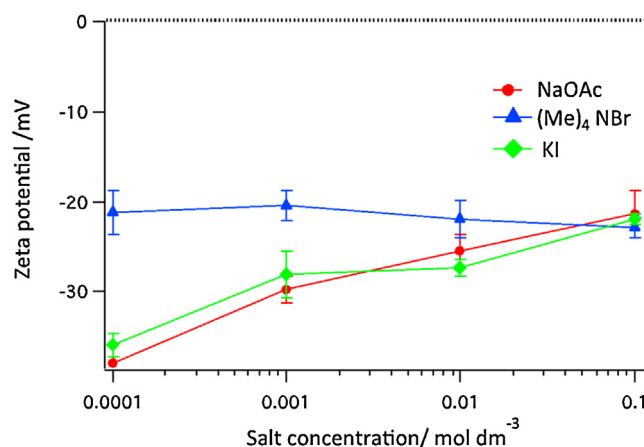


**Fig. 3.** The effect of hydrophobic ions on the zeta potential of CNC. Calculated ionic strengths and Debye lengths at which these data were obtained are presented in Supplementary material. Measurements were carried out at a pH of 6.

are not present, and this result also indicates that the application of the Smoluchowski and Grahame equations (see below) to convert mobility to zeta potential and surface charge respectively [14] are valid approximations for the CNC system. However, it is well known for other interfaces that have some hydrophobic characteristics – air/water, oil/water, gold/water, for example – that surface charge arises from the spontaneous adsorption of ions from solution – likely hydroxide in the case where no electrolyte is present [31]. It is therefore a logical question as to whether cellulose – known to have hydrophobic adsorption sites [32] – can also experience this phenomenon in addition to any charges arising from the surface-bound sulfate ester groups. If hydrophobic anions adsorb, we would expect to see a tendency to more negative zeta potentials, and if hydrophobic cations adsorb, we would see a move to more positive zeta potential values.

The salts KI, NaOAc and TMAB were selected to explore the potential for such specific ion adsorption effects. Iodide ions are well known for their hydrophobic nature [33]. Iodide ions are considered to be weakly hydrated anions whereas acetate ions are moderately hydrated anions and TMAB ions are weakly hydrated cations. A typical method for categorizing the hydrophobicity/hydrophilicity of these ions is the Hofmeister series [34,35], which was developed originally to explain the unexpected effects that different ions had on the rate of protein crystallization. Recently, the same theory was used to explain a host of other colloidal effects. For example, according to the Hofmeister series, weakly hydrated anions tend to destabilize macromolecules. However, the Hofmeister series becomes active only at relatively high salt concentrations, which is reflected in the observed zeta potentials for CNC with added KI and NaOAc. At low salt concentration, the electrolytes behave similarly to the simple salts explored (e.g. NaCl), however at higher salt concentrations, the reduction in the magnitude of the zeta potential is markedly less when hydrophobic anions are used. This could indicate that due to their added drive to adsorb through hydrophobic interactions, these ions preferentially locate at the CNC surface, increasing the surface charge density and thus the overall zeta potential. This effect is counterbalanced however by the fact that these ions still experience a strong electrostatic repulsion from the sulfate groups on the CNC surface. The physical reason for adsorption of hydrophobic (or poorly hydrated) ions to the CNC surface is assumed to be entropic in origin: by adsorbing, these ions release ordered water molecules from their hydration layers, increasing the water entropy of the system, and outweighing the decreased entropy of the ions themselves.

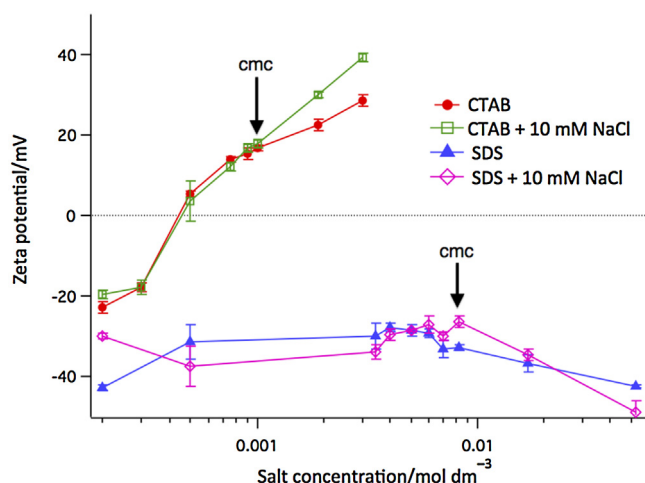


**Fig. 4.** Zeta potential measurements for CNC as a function of anionic (SDS) and cationic surfactant (CTAB) concentration, with and without 10 mM NaCl. For pure CTAB, the ionic strength of the systems under scrutiny ranges from  $2 \times 10^{-4}$  mol dm $^{-3}$  to  $3 \times 10^{-3}$  mol dm $^{-3}$ ; with 10 mM NaCl present, the range is from  $\sim 0.010$  mol dm $^{-3}$  to  $0.013$  mol dm $^{-3}$ , i.e. essentially constant. For pure SDS, the ionic strength range of the samples is from  $2 \times 10^{-4}$  mol dm $^{-3}$  to  $0.052$  mol dm $^{-3}$ ; with 10 mM NaCl present, the range is from  $\sim 0.010$  mol dm $^{-3}$  to  $0.062$  mol dm $^{-3}$ . In all instances, complete dissociation of the surfactant is assumed for these calculations. Measured pH of the CTAB systems was 4, and of the SDS systems was 5.

Further insight into the effects of ion adsorption can be obtained by using the measured surface potential values (obtained from electrophoretic mobility) in order to calculate the surface charge density. The surface charge density,  $\sigma$  can be calculated from the measured surface potential using the Grahame equation [14]:

$$\sigma = \sqrt{8c_0 \epsilon \epsilon_0 RT} \sinh \left( \frac{ze\psi_0}{2k_B T} \right)$$

where  $c_0$  is the bulk electrolyte concentration,  $\epsilon$  is the relative permittivity of the medium and  $\epsilon_0$  is the permittivity of free space,  $R$  is the gas constant,  $T$  is the absolute temperature,  $z$  is the valence of the ion,  $e$  is the fundamental charge,  $\psi_0$  is the surface potential and  $k_B$  is Boltzmann's constant. For the purposes of these simple analyses, we assume that surface and zeta potentials are equivalent.

For CNCs with no added salt (data in Fig. 1a), the average density of negative surface charges from ionised sulfate moieties is  $14.1$  nm $^2$ /charge, this corresponds to an average inter-charge distance of  $4.2$  nm. For  $0.1$  M KI and NaOAc, this inter-charge distance drops to  $3.6$  nm, indicating adsorption of additional negative ions, in line with the lower zeta potentials and expectation from specific adsorption of hydrophobic anions.

When moving to a salt bearing a hydrophobic cation in the form of TMAB, these effects are much more pronounced. For the same entropic reasons above, there is an additional drive for these cations to adsorb to the CNC surface, thus reducing the magnitude of the surface potential. However in this case, the net electrostatic charge experienced by the TMA ion is also attractive, and so the difference between the behaviour of this ion and, for example, sodium is clear. The relatively constant zeta potential with increasing TMAB concentration could indicate a balance between these hydrophobic and electrostatic interactions that is maintained with the increased screening as further salt is added.

Having explored simple electrolytes with weakly hydrophobic ions, a logical step is to investigate CNC stability in the presence of ionic surfactants; surfactants can be seen as electrolytes with a highly hydrophobic ion. The effect of cationic and anionic surfactants on the stability of CNC (Fig. 4) was therefore investigated. CTAB was selected as a model cationic surfactant and SDS as an anionic surfactant with critical micelle concentration (cmc)

values of  $1$  mM [36] and  $8.2$  mM [37], respectively. Concentrations above and below the surfactant's cmc values were analyzed. Upon addition of CTAB at low concentrations, the cationic surfactant ion binds strongly to the CNC surface, resulting in a significant increase in surface potential, thereby reducing the magnitude of the zeta potential; this is as expected. The resulting hydrophobicity due to CTAB adsorption tends to make the sample aggregate even at low surfactant concentrations, revealing an induced colloidal instability. However, as CTAB concentration increases, the zeta potential reverses and the surface of the CNC becomes positively charged. This indicates that charge is no longer the driving force for surfactant adsorption in this regime, and we postulate that hydrophobic interactions now dominate, for the same entropic reasons as the hydrophobic salt ions explored above. The pre-adsorbed CTAB clearly increases the effective hydrophobicity of the CNC, increasing the drive for further surfactant adsorption.

Even though there is an electrostatic repulsion between the SDS molecules and the negative CNC surface (due to the presence of dissociated sulfate moieties), SDS appears to also adsorb onto CNC by a hydrophobic effect. SDS molecules can adsorb onto the less charged regions of the CNC surface due to hydrophobic interactions that release water entropy, resulting in a favourable net reduction in the Gibbs free energy. Concomitant with their adsorption is a moderate increase in the magnitude of the CNC zeta potential; this 'supercharging' effect has been seen before for silica particles and SDS [38]. In the case of the data presented here, it is evident that SDS adsorption onto the CNC surfaces below and around the cmc is minimal, as evidenced by only very slight changes in surface potential, and that significant adsorption only occurs at high concentrations. The adsorption of SDS onto the CNC surfaces indicates that the energy and entropy balance between dissolved SDS and SDS adsorbed onto CNC favours adsorption only past a certain threshold. Interestingly, little change in zeta potential values was observed with SDS/CNC in the region of the cmc, possibly indicating that the adsorption and micellization thermodynamics result in similar energy balances, and that considerable concentration (i.e. chemical potential) of SDS is required to drive adsorption and overcome charge attractions.

For both CTAB and SDS experiments, the CNC zeta potential was also measured in  $10$  mM NaCl solutions with varying surfactant concentration. For CTAB, there is negligible difference between the two systems, again emphasising that hydrophobic interactions rather than charge effects are dominating adsorption in this regime. Indeed, the fact that ionic strength is essentially constant for all samples as a function of CTAB concentration when  $10$  mM NaCl is added indicates that charge screening has little effect on adsorption, and again points to a hydrophobic mechanism for adsorption. At the highest CTAB concentrations measured, the presence of background electrolyte did result in a slight increase in zeta potential, implying an increase in surfactant adsorption. This can be rationalised by increased screening between the charged head-groups of adsorbing surfactant and pre-adsorbed surfactant ions on the CNC surfaces. A previous study on negatively charged latex particles also observed this charge reversal phenomenon [39]. For SDS, the addition of background electrolyte induced small changes in zeta potential, indicating the possibility of moderate screening effects influencing the balance of hydrophobic and charge-based adsorption.

Interestingly, although addition of  $10$  mM background electrolyte would be expected to decrease the cmc of the two surfactants significantly, there is very little difference in adsorption between the cases with and without added sodium chloride. This likely indicates that the hydrophobically driven adsorption of the surfactants is independent of the aggregation state of the bulk surfactants – i.e., that the thermodynamic partitioning between adsorbed and non-adsorbed surfactant is unaffected by electrolyte



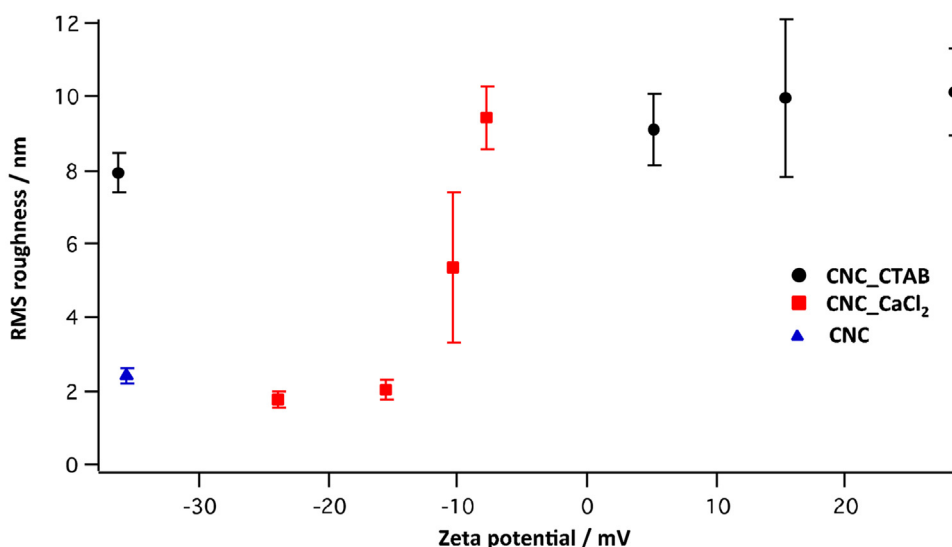


**Fig. 5.** Effect of CNC zeta potential on the RMS roughness of cellulose films. Specific zeta potential values were obtained by addition of CTAB or CaCl<sub>2</sub> before spin coating film samples.

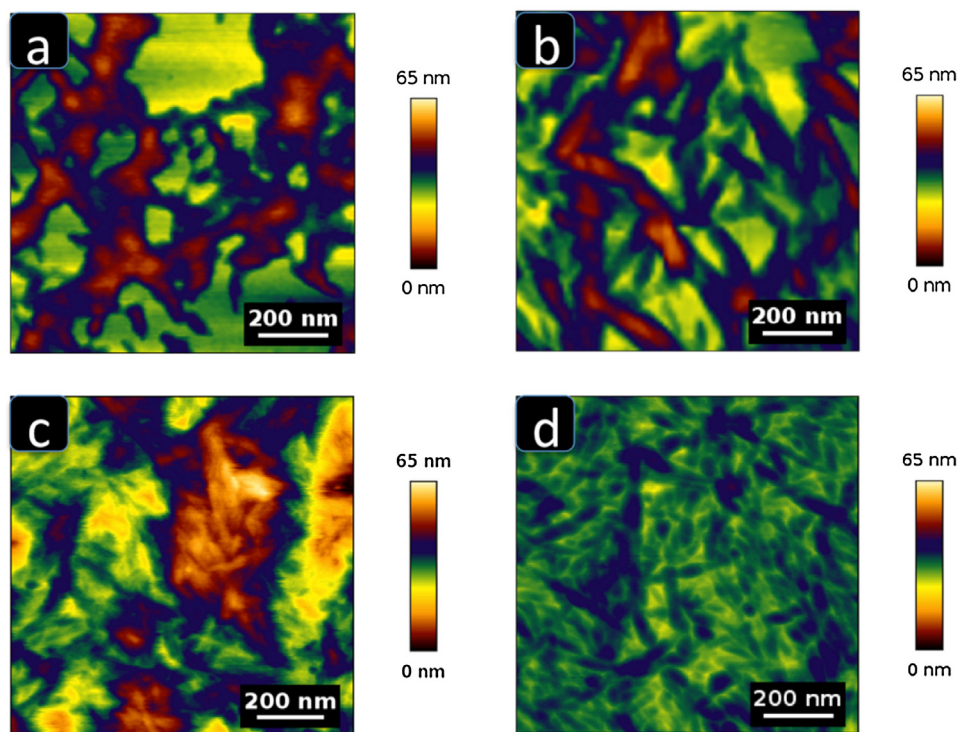


**Fig. 6.** AFM images of cellulose nanocrystals (CNC) with cetyltrimethylammonium bromide (CTAB) at concentrations a) 3.02 mM and b) 0.05 mM; c) AFM image of CNC with 0.1 mol dm<sup>-3</sup> calcium chloride (CaCl<sub>2</sub>); d) AFM image of precursor 0.5 mg/mL CNC sample. All the samples were spin-coated (2000–2300 rpm, 1–2 min) onto a glass slide to form a coating, which was then analyzed for roughness parameter using AFM. The color scheme for the z-dimension (height) is chosen to best emphasize differences between the samples.

or micellisation. As there are no stark effects at the cmc in each case, this is perhaps unsurprising.

In order to further explore the effects of zeta potential and bulk dispersion state on processing properties of CNCs, we explored films formed from precursor CNC dispersions where the zeta potential had been modified by additives of different types. Thus to determine the importance of zeta potential (and hence colloidal stability) on the morphology of CNC films, the average RMS roughness of CNC/CaCl<sub>2</sub> and CNC/CTAB spin coated films was measured using atomic force microscopy (AFM, Fig. 6). When dispersed in salt

solutions, the freeze-dried CNC samples used had a ‘shampoo-like’ optical texture as seen before [40], indicating local alignment and potentially aggregation in the dispersion. The roughness data presented in Fig. 5 indicate a strong inverse correlation between the CNC zeta potential and resultant film roughness: as the concentration of CaCl<sub>2</sub> increased, the RMS roughness of the CNC films also increased.

When using a hydrophobic surfactant, CTAB, to modify the zeta potential of the precursor CNC dispersion, different behaviour is seen. Interestingly, across a wide range of CTAB concentrations that

straddle the cmc of the surfactant – resulting in a large spectrum of measured CNC zeta potentials (see Fig. 5) from  $\sim -30$  mV to  $+30$  mV – there is essentially no effect on the surface roughness of films cast from these CNCs. This likely indicates a different format of the precursor CNC dispersion in this instance, with greater aggregation in dispersion induced by the hydrophobic nature of the adsorbed surfactant. In each case, the limiting roughness is around 10 nm RMS, indicating a ‘saturation’ in the roughness of films that is no longer dependent on the properties of the precursor suspension. This is likely limited by the radial dimensions of the crystals themselves.

These results indicate that the zeta potential of a precursor CNC suspension can be used at least semi-quantitatively in predicting the resulting roughness of a film made from the suspension. Further investigation into the role of the underlying substrate chemistry and film preparation method could lead to a fully quantitative prediction of these effects. Moreover, the mechanism by which zeta potential is implicated in resultant film morphology is likely more complex than simply corresponding to the dispersion quality of the precursor dispersion. In the assembly and drying process of the film, strong capillary interactions act between the surface and CNCs and between neighbouring CNCs. For anisotropic particles such as CNCs, shape-dependent capillary forces become important, further complicating this process [41]. It is likely that adsorbed surfactants modulate and disrupt these interactions more so than do simple adsorbed ions, resulting in both steric and hydrophobic effects during the drying process. Such hydrophobic interactions are short-range but very strong [42], potentially contributing to the random orientation of fibres on the substrate and thereby increasing film roughness.

#### 4. Conclusions

A systematic study of the zeta potential of cellulose nanocrystals (CNC) aqueous suspensions in different pH conditions and with different concentrations of inorganic salts, organic salts and surfactants was undertaken. To understand the implications of zeta potential to engineering outcomes for nanocellulose, roughness analysis was carried out using AFM measurements of spin-coated CNC samples.

Zeta potential measurements indicated significant differences between salts that could not be explained by valence alone, and instead indicate Hofmeister type specific ion effects. These findings can be explained by considering a subtle balance between electrostatic, hydration and hydrophobic effects. On moving to more hydrophobic ions in the form of surfactants, charge reversal and supercharging effects could be seen, again indicating a significant role for hydrophobic interactions in ion adsorption to CNC surfaces.

AFM analysis of the roughness of films made from CNC dispersions with different zeta potentials with ionic salts indicates an inverse relationship between zeta potential and film roughness, offering a simple method for controlling the morphology of CNC films. Modifying zeta potential using a hydrophobic surfactant however resulted in almost no change in surface roughness, potentially indicating different forces at play during film formation. Overall, these results indicate that ion and electrolyte choice offer a subtle and useful way to control CNC zeta potential, intimately linked to stability and the quality of films made from nanocrystal dispersions.

#### Acknowledgement

R. P. thanks the State Government of Victoria for the award of a Victoria India Doctoral Scholarship.

#### Appendix A. Supplementary data

Supplementary data associated with this article can be found, in the online version, at <http://dx.doi.org/10.1016/j.colsurfa.2016.08.075>.

#### References

- [1] C. Aulin, E. Karabulut, A. Tran, L. Wa<sup>o</sup>berg, T. Lindström, Transparent nanocellulosic multilayer thin films on polylactic acid with tunable gas barrier properties, *ACS Appl. Mater. Interfaces* 5 (2013) 7352–7359, <http://dx.doi.org/10.1021/am401700n>.
- [2] C. Aulin, S. Ahola, P. Josefsson, T. Nishino, Y. Hirose, M. Österberg, L. Wa<sup>o</sup>berg, Nanoscale cellulose films with different crystallinities and mesostructures – their surface properties and interaction with water, *Langmuir* 25 (2009) 7675–7685, <http://dx.doi.org/10.1021/la900323n>.
- [3] J. George, A.S. Bawa, Synthesis and characterization of bacterial cellulose nanocrystals and their PVA nanocomposites, *Adv. Mater. Res.* 123 (2010), <http://dx.doi.org/10.4028/www.scientific.net/AMR.123-125.383>, 123–125, 383–386.
- [4] N. Ljungberg, C. Bonini, F. Bortolussi, C. Boisson, L. Heux, J. Cavallé, New nanocomposite materials reinforced with cellulose whiskers in atactic polypropylene: effect of surface and dispersion characteristics, *Biomacromolecules* 6 (2005) 2732–2739, <http://dx.doi.org/10.1021/bm050222v>.
- [5] M.A.S.A. Samir, F. Alloin, A. Dufresne, Review of recent research into cellulosic whiskers, their properties and their application in nanocomposite field, *Biomacromolecules* 6 (2005) 612–626, <http://dx.doi.org/10.1021/bm0493685>.
- [6] A. Šturcová, G.R. Davies, S.J. Eichhorn, Elastic modulus and stress-transfer properties of tunicate cellulose whiskers, *Biomacromolecules* 6 (2005) 1055–1061, <http://dx.doi.org/10.1021/bm049291k>.
- [7] E.D. Cranston, D.G. Gray, Morphological and optical characterization of polyelectrolyte multilayers incorporating nanocrystalline cellulose, *Biomacromolecules* 7 (2006) 2522–2530, <http://dx.doi.org/10.1021/bm060288>.
- [8] Y. Habibi, L.A. Lucia, O.J. Rojas, Cellulose nanocrystals: chemistry, self-assembly, and applications, *Chem. Rev.* 110 (2010) 3479–3500, <http://dx.doi.org/10.1021/cr900339w>.
- [9] K.E. Shpopsowitz, H. Qi, W.Y. Hamad, M.J. MacLachlan, Free-standing mesoporous silica films with tunable chiral nematic structures, *Nature* 468 (2010) 422–425, <http://dx.doi.org/10.1038/nature09540>.
- [10] S. Elazzouzi-Hafraoui, Y. Nishiyama, J. Putaux, L. Heux, F. Dubreuil, C. Rochas, The shape and size distribution of crystalline nanoparticles prepared by acid hydrolysis of native cellulose, *Biomacromolecules* 9 (2007) 57–65, <http://dx.doi.org/10.1021/bm700769p>.
- [11] X.M. Dong, D.G. Gray, Effect of counterions on ordered phase formation in suspensions of charged rodlike cellulose crystallites, *Langmuir* 13 (1997) 2404–2409, <http://dx.doi.org/10.1021/la960724h>.
- [12] D. Klemm, F. Kramer, S. Moritz, T. Lindström, M. Ankerfors, D. Gray, A. Dorris, Nanocelluloses: a new family of nature-based materials, *Angew. Chem. Int. Ed.* 50 (2011) 5438–5466, <http://dx.doi.org/10.1002/anie.201001273>.
- [13] Y. Boluk, R. Lahiji, L. Zhao, M.T. McDermott, Suspension viscosities and shape parameter of cellulose nanocrystals (CNC), *Colloids Surf. A* 377 (2011) 297–303, <http://dx.doi.org/10.1016/j.colsurfa.2011.01.003>.
- [14] R.J. Hunter, *Foundations of Colloid Science*, Oxford University Press, New York, 2001.
- [15] Y. Leong, B. Ong, Critical zeta potential and the Hamaker constant of oxides in water, *Powder Technol.* 134 (2003) 249–254, <http://dx.doi.org/10.1016/j.powtec.2003.08.054>.
- [16] S. Wang, W.J. Wei, Electrokinetic properties of nanosized SiC particles in highly concentrated electrolyte solutions, *J. Am. Ceram. Soc.* 84 (2001) 1411–1414, <http://dx.doi.org/10.1111/j.1151-2916.2001.tb00852.x>.
- [17] N. Bizmark, M.A. Ioannidis, Effects of ionic strength on the colloidal stability and interfacial assembly of hydrophobic ethyl cellulose nanoparticles, *Langmuir* 31 (2015) 9282–9289, <http://dx.doi.org/10.1021/acs.langmuir.5b01857>.
- [18] L. Zhong, S. Fu, X. Peng, H. Zhan, R. Sun, Colloidal stability of negatively charged cellulose nanocrystalline in aqueous systems, *Carbohydr. Polym.* 90 (2012) 644–649, <http://dx.doi.org/10.1016/j.carbpol.2012.05.091>.
- [19] W. Yu, F. Bouyer, M. Borkovec, Polystyrene sulfate latex particles in the presence of poly(vinylamine): absolute aggregation rate constants and charging behavior, *J. Colloid Interface Sci.* 241 (2001) 392–399, <http://dx.doi.org/10.1006/jcis.2001.7751>.
- [20] N. Dhar, D. Au, R.C. Berry, K.C. Tam, Interactions of nanocrystalline cellulose with an oppositely charged surfactant in aqueous medium, *Colloids Surf. A* 415 (2012) 310–319, <http://dx.doi.org/10.1016/j.colsurfa.2012.09.010>.
- [21] J.K. Jackson, K. Letchford, B.Z. Wasserman, L. Ye, W.Y. Hamad, H.M. Burt, The use of nanocrystalline cellulose for the binding and controlled release of drugs, *Int. J. Nanomed.* 6 (2011) 321–330, <http://dx.doi.org/10.2147/IJN.S16749>.
- [22] M. Hasani, E.D. Cranston, G. Westman, D.G. Gray, Cationic surface functionalization of cellulose nanocrystals, *Soft Matter* 4 (2008) 2238–2244, <http://dx.doi.org/10.1039/B806789A>.

- [23] D. Bondeson, A. Mathew, K. Oksman, Optimization of the isolation of nanocrystals from microcrystalline cellulose by acid hydrolysis, *Cellulose* 13 (2006) 171–180, <http://dx.doi.org/10.1007/s10570-006-9061-4>.
- [24] P. Lu, Y. Hsieh, Preparation and properties of cellulose nanocrystals: rods, spheres, and network, *Carbohydr. Polym.* 82 (2010) 329–336, <http://dx.doi.org/10.1016/j.carbpol.2010.04.073>.
- [25] C.J. Garvey, I.H. Parker, G.P. Simon, On the interpretation of X-ray diffraction powder patterns in terms of the nanostructure of cellulose I fibres, *Macromol. Chem. Phys.* 206 (2005) 1568–1575, <http://dx.doi.org/10.1002/macp.200500008>.
- [26] A.D. French, Idealized powder diffraction patterns for cellulose polymorphs, *Cellulose* 21 (2013) 885–896, <http://dx.doi.org/10.1007/s10570-013-0030-4>.
- [27] G. Siqueira, J. Bras, A. Dufresne, Luffa cylindrica as a lignocellulosic source of fiber: microfibrillated cellulose and cellulose nanocrystals, *BioResources* 5 (2010) 727–740.
- [28] H. Oshima, *Electrophoresis in Wiley Encyclopedia of Biomedical Engineering*, Wiley, New York, 2006.
- [29] M. Kobayashi, Electrophoretic mobility of latex spheres in the presence of divalent ions: experiments and modeling, *Colloid Polym. Sci.* 286 (2008) 935–940, <http://dx.doi.org/10.1007/s00396-008-1851-9>.
- [30] T. Cosgrove, *Colloid Science: Principles, Methods and Applications*, Blackwell Publishing, UK, 2005.
- [31] R.F. Tabor, F. Grieser, R.R. Dagastine, D.Y.C. Chan, Measurement and analysis of forces in bubble and droplet systems using AFM, *J. Colloid Interface Sci.* 371 (2012) 1–14, <http://dx.doi.org/10.1016/j.jcis.2011.12.047>.
- [32] S. Paria, C. Manohar, K.C. Khilar, Kinetics of adsorption of anionic, cationic, and nonionic surfactants, *Ind. Eng. Chem. Res.* 44 (2005) 3091–3098, <http://dx.doi.org/10.1021/ie049471a>.
- [33] D. Horinek, A. Herz, L. Vrbka, F. Sedlmeier, S.I. Mamatkulov, R.R. Netz, Specific ion adsorption at the air/water interface: the role of hydrophobic solvation, *Chem. Phys. Lett.* 479 (2009) 173–183, <http://dx.doi.org/10.1016/j.cplett.2009.07.077>.
- [34] M. Cacace, E. Landau, J. Ramsden, The Hofmeister series: salt and solvent effects on interfacial phenomena, *Q. Rev. Biophys.* 30 (1997) 241–277, <http://dx.doi.org/10.1017/S0033583597003363>.
- [35] K.D. Collins, M.W. Washabaugh, The Hofmeister effect and the behaviour of water at interfaces, *Q. Rev. Biophys.* 18 (1985) 323–422, <http://dx.doi.org/10.1017/S0033583500005369>.
- [36] A. Murphy, G. Taggart, A comparison of predicted and experimental critical micelle concentration values of cationic and anionic ternary surfactant mixtures using molecular-thermodynamic theory and pseudophase separation theory, *Colloids Surf. A* 205 (2002) 237–248, [http://dx.doi.org/10.1016/S0927-7757\(02\)00019-5](http://dx.doi.org/10.1016/S0927-7757(02)00019-5).
- [37] A. Cifuentes, J.L. Bernal, J.C. Diez-Masa, Determination of critical micelle concentration values using capillary electrophoresis instrumentation, *Anal. Chem.* 69 (1997) 4271–4274, <http://dx.doi.org/10.1021/ac970696n>.
- [38] S. Ahualli, G. Iglesias, W. Wachter, M. Dulle, D. Minami, O. Glatter, Adsorption of anionic and cationic surfactants on anionic colloids: supercharging and destabilization, *Langmuir* 27 (2011) 9182–9192, <http://dx.doi.org/10.1021/la201242d>.
- [39] M. Finessi, P. Sinha, I. Szilagyi, I. Popa, P. Maroni, M. Borkovec, Charge reversal of sulfate latex particles by adsorbed linear poly (ethylene imine) probed by multiparticle colloidal probe technique, *J. Mater. Chem. B* 115 (2011) 9098–9105, <http://dx.doi.org/10.1021/jp203514r>.
- [40] S. Beck, J. Bouchard, R. Berry, Dispersibility in water of dried nanocrystalline cellulose, *Biomacromolecules* 13 (2012) 1486–1494, <http://dx.doi.org/10.1021/bm300191k>.
- [41] P.J. Yunker, T. Still, M.A. Lohr, A.G. Yodh, Suppression of the coffee-ring effect by shape-dependent capillary interactions, *Nature* 476 (2011) 308–311, <http://dx.doi.org/10.1038/nature10344>.
- [42] R.F. Tabor, C. Wu, F. Grieser, R.R. Dagastine, D.Y.C. Chan, Measurement of the hydrophobic force in a soft matter system, *J. Phys. Chem. Lett.* 4 (2013) 3872–3877, <http://dx.doi.org/10.1021/jz402068k>.

# Modulating the zeta potential of cellulose nanocrystals using salts and surfactants

## Supplementary Material

Ragesh Prathapan,<sup>a</sup> Rajiv Thapa,<sup>a</sup> Gil Garnier<sup>b\*</sup> and Rico F. Tabor<sup>a\*</sup>

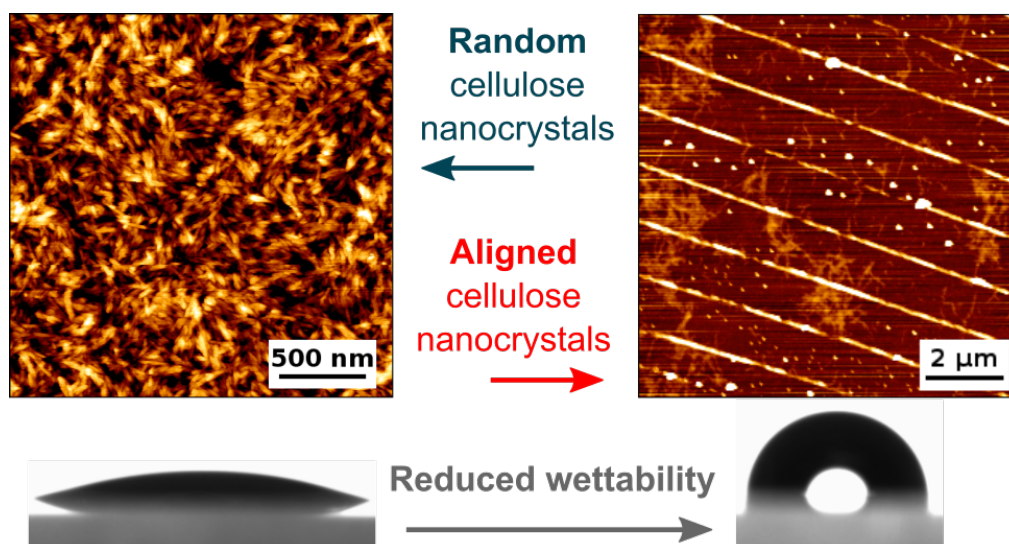
*a: School of Chemistry, Monash University, Clayton VIC, Australia 3800*

*b: Bioresources Processing Research Institute of Australia (BioPRIA), Department of Chemical Engineering, Monash University, Clayton VIC, Australia 3800*

**Table S1:** Calculated ionic strength and Debye length for the experiments in which the mobility of CNCs was measured in the presence of salt.

Figure in main paper	pH	Salt identity	Added salt conc <sup>n</sup> mol dm <sup>-3</sup>	Ionic strength mol dm <sup>-3</sup>	Debye length nm
Fig. 1	1	none	0	0.1	0.96
	2		0	0.01	3.03
	4		0	1×10 <sup>-4</sup>	30.35
	6		0	1×10 <sup>-6</sup>	303.48
	8		0	1×10 <sup>-6</sup>	303.48
	10		0	1×10 <sup>-4</sup>	30.35
Fig. 2	6	CaCl <sub>2</sub>	1×10 <sup>-4</sup>	4×10 <sup>-4</sup>	14.31
			1×10 <sup>-3</sup>	4.5×10 <sup>-3</sup>	4.52
			0.01	0.045	1.43
			0.1	0.45	0.45
	6	NaCl	1×10 <sup>-4</sup>	1×10 <sup>-4</sup>	30.35
			1×10 <sup>-3</sup>	1×10 <sup>-3</sup>	9.60
			0.01	0.01	3.03
			0.1	0.1	0.96
	2	NaCl	1×10 <sup>-4</sup>	0.010	3.02
			1×10 <sup>-3</sup>	0.011	2.89
			0.01	0.02	2.15
			0.1	0.11	0.92
	10	NaCl	1×10 <sup>-4</sup>	2×10 <sup>-4</sup>	21.46
			1×10 <sup>-3</sup>	1.1×10 <sup>-3</sup>	9.15
			0.01	0.02	3.02
			0.1	0.1	0.96
Fig. 3	6	NaOAc	1×10 <sup>-4</sup>	1×10 <sup>-4</sup>	30.35
			1×10 <sup>-3</sup>	1×10 <sup>-3</sup>	9.60
			0.01	0.01	3.03
			0.1	0.1	0.96
	6	(Me) <sub>4</sub> NBr	1×10 <sup>-4</sup>	1×10 <sup>-4</sup>	30.35
			1×10 <sup>-3</sup>	1×10 <sup>-3</sup>	9.60
			0.01	0.01	3.03
			0.1	0.1	0.96
	6	KI	1×10 <sup>-4</sup>	1×10 <sup>-4</sup>	30.35
			1×10 <sup>-3</sup>	1×10 <sup>-3</sup>	9.60
			0.01	0.01	3.03
			0.1	0.1	0.96

## Preface for Chapter 4



As seen in Chapter 1, different methods have been reported to surface functionalize CNCs to disperse them as nano-fillers in various nanocomposites. But these functionalization methods affect the surface chemistry of cellulose nanocrystals. In this Chapter, we explore a fascinating technology inspired by nature in the form of wrinkling, in order to align cellulose nanocrystals. Wrinkles are ubiquitous in nature, and in this work, could be achieved using plasma oxidation of a strained elastomeric substrate followed by slow relaxation, resulting in wrinkles perpendicular to the applied strain. Determination of the wettability of aligned CNC using water-contact angle measurements was then carried out to understand whether surface structuring has any influence on the wettability of CNCs. The oil contact angle of aligned CNCs under water is later studied for anti-fouling applications.



# Decreasing the Wettability of Cellulose Nanocrystal Surfaces Using Wrinkle-Based Alignment

Ragesh Prathapan,<sup>†</sup> Joseph D. Berry,<sup>‡</sup> Andreas Fery,<sup>§</sup> Gil Garnier,<sup>||</sup> and Rico F. Tabor<sup>\*,†,‡</sup>

<sup>†</sup>School of Chemistry, Monash University, Clayton, Victoria 3800, Australia

<sup>‡</sup>Department of Chemical and Biomolecular Engineering and the Particulate Fluids Processing Centre, University of Melbourne, Parkville, Victoria 3010, Australia

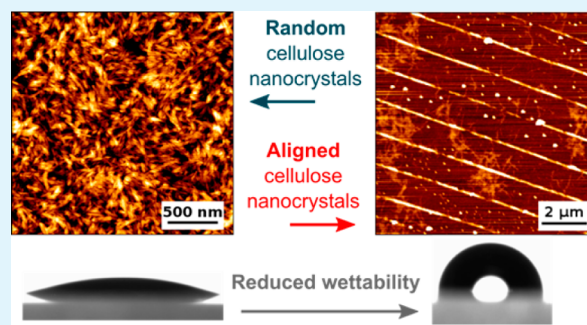
<sup>§</sup>Institute for Physical Chemistry and Polymer Physics, Leibniz-Institut für Polymerforschung Dresden e.V., 01069 Dresden, Germany

<sup>||</sup>Bioresources Processing Research Institute of Australia (BioPRIA), Department of Chemical Engineering, Monash University, Clayton, Victoria 3800, Australia

## Supporting Information

**ABSTRACT:** Cellulose nanocrystals (CNCs) are a particularly appealing format of the natural biopolymer due to their exceptional strength, nanoscale dimensions, and needle-like shape anisotropy. However, CNCs are hydrophilic and hence their wettability makes them impractical for many coating applications, with various approaches using chemical functionalization to overcome this. Here we show that CNC-coated surfaces can be rendered hydrophobic by alignment of the native CNCs using a wrinkled template-mediated printing process. We present a novel and simple method allowing full release of the CNCs from the template and their permanent adsorption into fine patterns onto the surface, thus preventing CNC repositioning during wetting. The aligned CNCs induce strong pinning effects that capture and retain water droplets with high contact angle and large roll-off angles, without becoming susceptible to oil contamination. The fabrication process for these coatings could be achieved by large-scale printing, making them a practical and cost-effective solution to hydrophobic coatings from raw cellulosic materials.

**KEYWORDS:** cellulose nanocrystals, wettability, pinning, alignment, hydrophobicity



## 1. INTRODUCTION

Research into cellulose nanocrystals (CNCs) has become an increasingly active area owing to their widespread potential applications in wound dressings, composites, coatings, medical implants, and so forth.<sup>1</sup> The unique combination of properties exhibited by CNCs, such as optical transparency,<sup>2</sup> high elastic modulus,<sup>3</sup> biocompatibility, and tunable surface chemistry,<sup>4</sup> makes their use appealing in a range of fields. The hydroxyl groups (and sulfate esters often present from synthesis by acid hydrolysis) on the CNC surfaces render them hydrophilic, which is suited to some but not all applications.<sup>5</sup> Active research has focused on hydrophobizing cellulose nanocrystals using various types of chemical functionalization, so that their dispersion in hydrophobic polymer materials or matrixes could be improved.<sup>6</sup> However, such surface functionalization methods are expensive and necessarily affect the surface chemistry of cellulose nanocrystals. Thus, a method for achieving hydrophobic coatings from CNCs without changing their surface chemistry is highly desirable. Moreover, the concept of a surface composed of hydrophilic materials, but that can behave in a hydrophobic manner, is particularly appealing, as it avoids many conventional issues of hydrophobic surfaces such as their

rapid contamination by adsorption of hydrophobic impurities and fouling by oils.

The patterning of surfaces has been studied extensively in the literature, in order to achieve enhanced surface properties such as special wetting characteristics or self-cleaning.<sup>7</sup> For example, the assembly of 3D colloidal crystals could be achieved using periodic patterns<sup>8–12</sup> and such patterning has been achieved either using a bottom-up approach (e.g., self-assembly) or a top-down approach (lithography). Even though both approaches have their specific benefits, they suffer from certain limitations. For example, the bottom-up approach is more vulnerable to defects even though it allows for smaller periodicities, whereas lateral resolution in periodicity is a limiting factor for the top-down approach.<sup>7</sup>

The mechanical wrinkling of surfaces is an alternative and efficient way that can be used to create periodic patterns ranging from <100 nm to several microns in characteristic spacing. Wrinkles are omnipresent in nature in membranes, human skin, fruits, and so forth<sup>13</sup> and wrinkled substrates are

**Received:** March 3, 2017

**Accepted:** April 12, 2017

**Published:** April 12, 2017

promising for use as diffraction gratings, microfluidic sieves, templates for cell proliferation, and so forth. Buckling instabilities are observed when membranes are subjected to compressive strains, resulting in wrinkles that form perpendicular to the direction of applied stress.<sup>14</sup> Controlled wrinkling can be achieved through various techniques such as plasma or UV/ozone exposure,<sup>15</sup> sputter coating,<sup>16</sup> or evaporation,<sup>17</sup> on elastomeric surfaces.

The majority of wrinkling studies conducted on polymeric surfaces thus far use polydimethylsiloxane (PDMS)<sup>18</sup> as an elastomeric substrate onto which tensile strain is applied, and the strain is subsequently relaxed (often after surface treatment) to achieve the wrinkles. Bowden et al.<sup>19</sup> recognized the potential of metal evaporation onto PDMS for structural modification. After the PDMS surface was thermally expanded, the surface was coated with metal particles, and after thermal shrinkage of the PDMS while cooling to room temperature, wrinkles were created on the surface. In further work,<sup>20</sup> the same concept of thermal shrinkage was used wherein the PDMS surface was oxidized using a plasma treatment. Around 50% of the topmost layer of PDMS was converted into silica (SiO<sub>2</sub>) that resists thermal shrinkage upon cooling the underlying PDMS to room temperature. Periodicities of  $\sim 10\ \mu\text{m}$  were reported with some cracks owing to the presence of the brittle silica material at the surface. Genzer et al.<sup>21</sup> demonstrated the application of a custom-built stretching apparatus to avoid the need for thermal expansion/contraction and instead to take advantage of controlled, unidirectional mechanical stretching, and relaxation. A strain of 30–50% was applied to PDMS that was clamped onto the experimental setup, and periodic wrinkles perpendicular to the applied strain were observed after the stretched PDMS was surface-oxidized and relaxed. Lu et al.<sup>22</sup> demonstrated wrinkle formation by applying uniaxial plastic deformation on polymer films deposited by layer-by-layer assembly on soft elastomeric substrates. The polymer films with wrinkles were then used as a template whereby colloidal particles of  $\sim 380\ \text{nm}$  were deposited to align with the template. Horn et al.<sup>23</sup> demonstrated the alignment of tobacco mosaic virus (TMV) on wrinkled surfaces. Spin coating was utilized to align the virus onto the wrinkled PDMS substrate. The aligned TMVs could be used as a template system to similarly align anisotropic particles via further spin coating. Nystrom et al.<sup>24</sup> studied the alignment of cellulose nanocrystals on wrinkled PDMS substrates. The aligned CNC was transferred to a silica substrate coated with polyethylene imine (PEI) via wet stamping, resulting in the production of highly ordered surfaces.

However, due to the anisotropic nature of CNCs, other methods have also been utilized to achieve alignment in the bulk or at surfaces. Habibi et al.<sup>25</sup> demonstrated the orientation of cellulose nanocrystals using an electric field, wherein the orientation was controlled by the strength and frequency of the applied electric field. Munier et al.<sup>26</sup> studied the alignment of cellulose nanocrystals using unidirectional freezing of nanocellulose dispersions, which produced rod-shaped aligned cellular foams with alignment in the freezing direction. Local orientation of cellulose nanocrystals were studied by Wanasekara et al.<sup>27</sup> using electrospun poly(styrene)–poly(vinyl alcohol) nanofibers with CNC. CNC alignment in dry films was investigated by Reising et al.<sup>28</sup> using shear-based casting methods. Magnetic alignment of CNC's has been extensively studied<sup>29–32</sup> although high fields are required to achieve

significant alignment. Recently, orientation of CNCs using a low magnetic field was achieved by adsorbing a high concentration of iron-oxide nanoparticles ( $\sim 51\ \text{wt}\%$ ) onto CNCs.<sup>33</sup>

The present work focuses on alignment of CNCs using wrinkled PDMS substrates, initially via a process similar to that reported by Nystrom et al.<sup>24</sup> Both micron-scale and submicron-scale wrinkle-aligned CNCs are explored on glass substrates, aided by adsorbed cationic polyelectrolytes. Extensive wetting studies show that by alignment using wrinkled templates, the CNC surface wettability could be tuned from hydrophilic to hydrophobic, crucially without altering or affecting the CNC surface chemistry. The concept of using physical surface topology rather than chemical functionalization to control wetting offers significant advantages, particularly in retaining the native hydrophilicity of the CNCs. This noncovalent and scalable method of surface hydrophobization using biore-sourced particles may find applications in printing, device manufacture, and coating, where the control of surface wettability is central.

## 2. EXPERIMENTAL SECTION

**2.1. Materials.** Cellulose nanocrystals (CNC, 12.2 wt %) were obtained from the University of Maine Process Development Center as a dispersion in water (with sulfur content 1–2%). Poly(ethylene oxide) (PEO, average molecular weight ( $M_v$ ) 400 000 g mol<sup>-1</sup>) was purchased from Sigma-Aldrich, U.S.A. Poly(amidoamine) epichlorohydrin (PAE, 33.5 wt %) was purchased from Nopco Chemical. Polyethylenimine (PEI, average molecular weight 25 000 g mol<sup>-1</sup> by LS) was purchased from Sigma-Aldrich, Germany. Sylgard 184 Silicone elastomer curing agent and Sylgard 184 Silicone elastomer base (Dow Corning Corporation, U.S.A.) were used to synthesize polydimethylsiloxane (PDMS). 1-Bromodecane (98%, Sigma-Aldrich, U.S.A.) was used as the test liquid for oil contact angle measurements.

**2.2. Instrumental Techniques.** Atomic force microscopy (AFM, JPK Nanowizard 3) was used in alternating contact, AC mode to obtain images representing the morphology of PDMS templates, aligned CNC, and random CNC. A spin coater (Laurell technologies, WS-400BZ-6NPP/LITE) was used to prepare CNC/PEO on PDMS as well as for coating random CNC on PAE/PEI and PAE surfaces. For creating the PDMS wrinkled substrates, an air plasma chamber (Model PDC 002, Harrick Scientific Corporation, U.S.A.) with 30 W plasma power was used. The wettability studies were made using a contact angle-measuring setup (Dataphysics, OCA35). The oil contact angle measurements were performed using a customized setup discussed below.

**2.3. PDMS Preparation.** PDMS was prepared by mixing the Sylgard 184 silicone elastomer base and Sylgard 184 silicone elastomer-curing agent in the prescribed ratio of 10:1. The mixture was well mixed using a glass rod, poured into a polystyrene Petri dish, and kept at room temperature (RT) for around 24 h, after which it was baked for 2 h at 60 °C. It was then allowed to cool down and small pieces of PDMS of dimension 50 × 20 mm<sup>2</sup> were cut for carrying out experiments.

**2.4. Aligned CNC Preparation.** The PDMS was initially stretched using a custom-built apparatus. The strain applied on PDMS to make templates for the alignment of CNC on PEI was 20%, whereas to make smaller wrinkles (0.495  $\mu\text{m}$ ) and larger wrinkles (1.37  $\mu\text{m}$ ), the strain was 16% and 29%, respectively. To obtain 637 nm wrinkles, a strain of 22% was applied to the PDMS. The stretched PDMS was then put into an air–plasma chamber and the plasma was generated for 9 min with a power of 30 W. The PDMS was then cooled for around 15 min and then relaxed to its original position. The relaxation creates wrinkles perpendicular to the direction of applied strain, which produces characteristic iridescent coloration of the surface via interaction of light with the wrinkles. The wrinkled PDMS was again placed in air-plasma for 2–3 min to activate the surface for

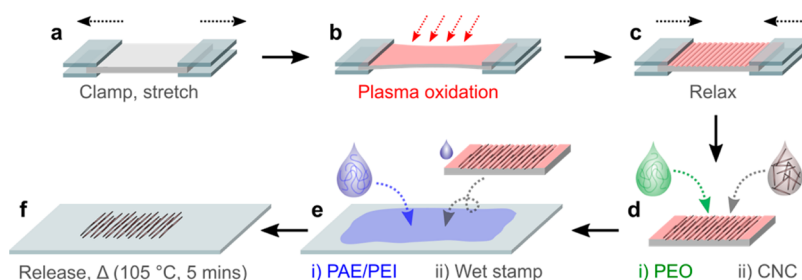


**Figure 1.** Fabrication of aligned CNC surfaces: (a) A section of PDMS elastomer is clamped and stretched such that it is under extensional tension. (b) The surface of the PDMS is oxidized using an air plasma, to generate a thin film of silica. (c) Strain relaxation results in the formation of regular wrinkles on the PDMS surface due to the inelasticity of the generated silica layer. (d) The template is spin coated with PEO solution followed by CNC dispersion. (e) The CNC-coated template is wet stamped onto a glass slide that has been pretreated with cationic polyelectrolyte(s). (f) After release of the template, the surface is heat cured when PAE is used.

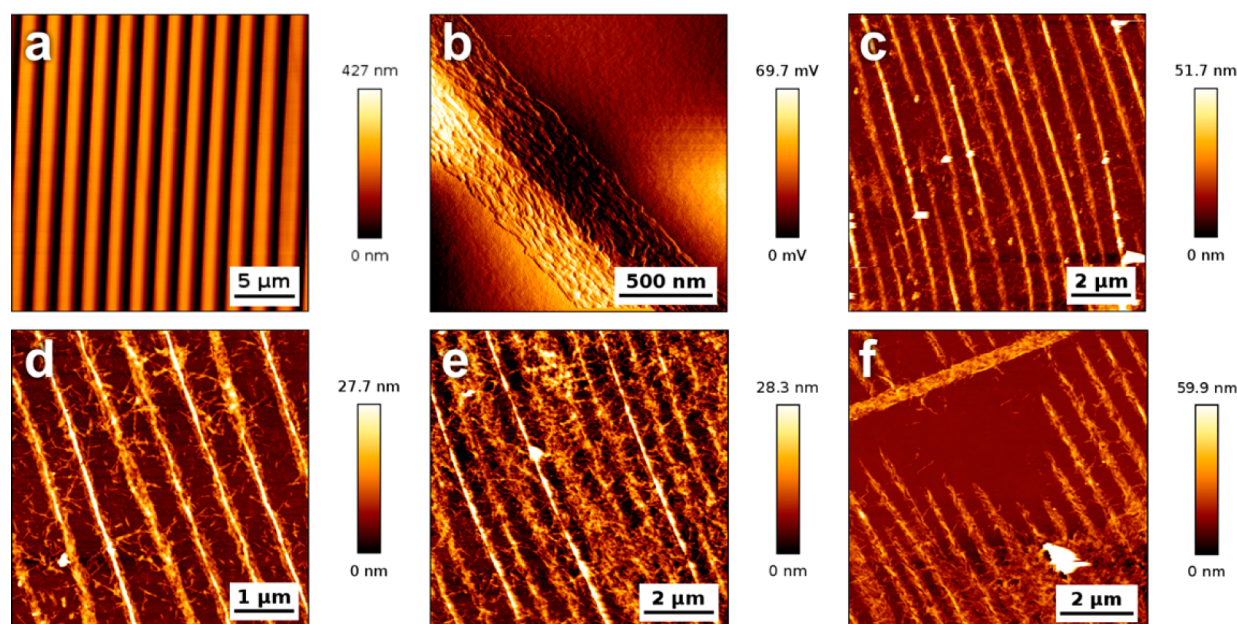


**Figure 2.** Atomic force microscopy (AFM) images of (a) Topology of PDMS template with CNC spin coated into its grooves. (b) Amplitude trace to better emphasize the presence of CNC within the PDMS grooves. (c) CNC stamped onto a glass slide coated with PEI. (d) As (c) but smaller scan area to better emphasize the local orientation of the CNCs. (e) CNC/PEI stamped surface showing the spreading of CNCs caused by water wetting and (f) Distorted CNC alignment due to water wetting on a stamped CNC/PEI surface.

deposition of PEO (1 wt %) and then CNC ( $5 \text{ mg mL}^{-1}$ ) using a spin coater (2500 rpm, 1 min). PEO solution and CNC dispersion ( $20 \mu\text{L}$  each) were applied to create aligned CNC using the  $0.495 \mu\text{m}$  wrinkled substrate, whereas PEO ( $20 \mu\text{L}$ ) and CNC ( $60 \mu\text{L}$ ) were used with the larger period wrinkles. Microscope glass slides were cleaned thoroughly with soap solution, ethanol and then deionized water. The glass slide was then exposed to air–plasma for 5–10 min to remove any organic contaminants and to make the surface more hydrophilic in nature. To create the initial sample of aligned CNC on PEI surface, PEI ( $1 \text{ g L}^{-1}$ , pH 8) was poured onto the glass slide and left for around 10 min. For use with the  $495 \text{ nm}$  wrinkled substrate, PAE ( $0.5 \text{ wt } \%$ ) was poured onto the cleaned glass slide. Similarly, for the  $1.37 \mu\text{m}$  wrinkled substrate, a 1:1 mixture of PAE ( $0.5 \text{ wt } \%$ ) and PEI ( $1 \text{ g L}^{-1}$ ) was coated onto the glass slide. The glass slide was then dried with nitrogen gas for 10 min. The prepared PDMS was then stamped on the glass surface with the help of a water droplet ( $1 \mu\text{L}$ ), facilitating water-mediated contact printing. The PDMS was left in contact with the glass surface until the water evaporated, and then the PDMS was carefully peeled off, resulting in aligned CNC on PEI or PAE or PAE/PEI coated glass substrates. The glass thus coated with CNC/PAE and CNC/PAE/PEI was then heated to  $105 \text{ }^{\circ}\text{C}$  for about 5 min, facilitating the covalent bonding of PAE with CNC.

**2.5. Control Sample Preparation.** As discussed in the above section, the glass slides were cleaned using ethanol, soap solution, and deionized water and exposed to an air–plasma. Onto the prepared PAE and PAE/PEI glass slides, randomly distributed CNC ( $5 \text{ mg mL}^{-1}$ ,  $120 \mu\text{L}$ ) was deposited using a spin-coater (2500 rpm, 1 min). The resulting samples were then heated to  $105 \text{ }^{\circ}\text{C}$  for about 5 min, thus yielding random CNC/PAE/PEI and random CNC/PAE on glass substrates.

**2.6. Measuring Contact Angle and Roll-Off Angle.** To analyze the contact angle of the aligned CNC as well as other control samples, a sessile drop of water ( $3 \mu\text{L}$ ) was used. The advancing angle was measured by growing the water drop (from  $3 \mu\text{L}$ ) in increments until the contact line changed, whereas the receding angle was measured by withdrawing water (from an  $8 \mu\text{L}$  drop, gradually decreasing to around  $0.5 \mu\text{L}$ ). This method of sessile volume drop analysis was carried out to obtain the contact angle hysteresis, which is the difference between the advancing and receding angle. To measure the roll-off angle, a tiltable platform was used. The intended sample was secured firmly on the platform using adhesive tape. A water drop ( $3 \mu\text{L}$ ) was placed on the sample surface, and the platform was tilted until the droplet rolled off the surface, so as to measure the critical roll-off angle. At least 6 trials were performed for each sample to obtain the average critical roll-off angle.



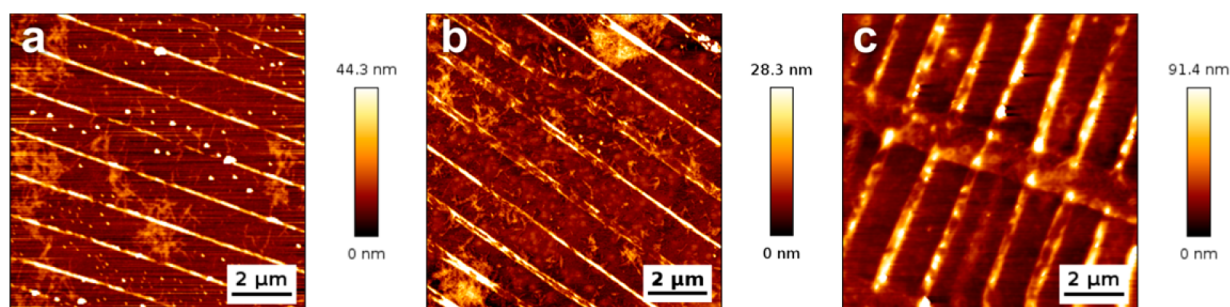


**Figure 3.** AFM images of (a) Slides spin coated with 1 wt % PAE followed by stamping with a 5 mg/mL CNC dispersion on a glass substrate. (b) The sample shown in (a) after water stability testing, showing little CNC movement. (c) Slides spin coated with 0.5 wt % PAE followed by stamping with a 5 mg/mL CNC dispersion on a glass substrate.

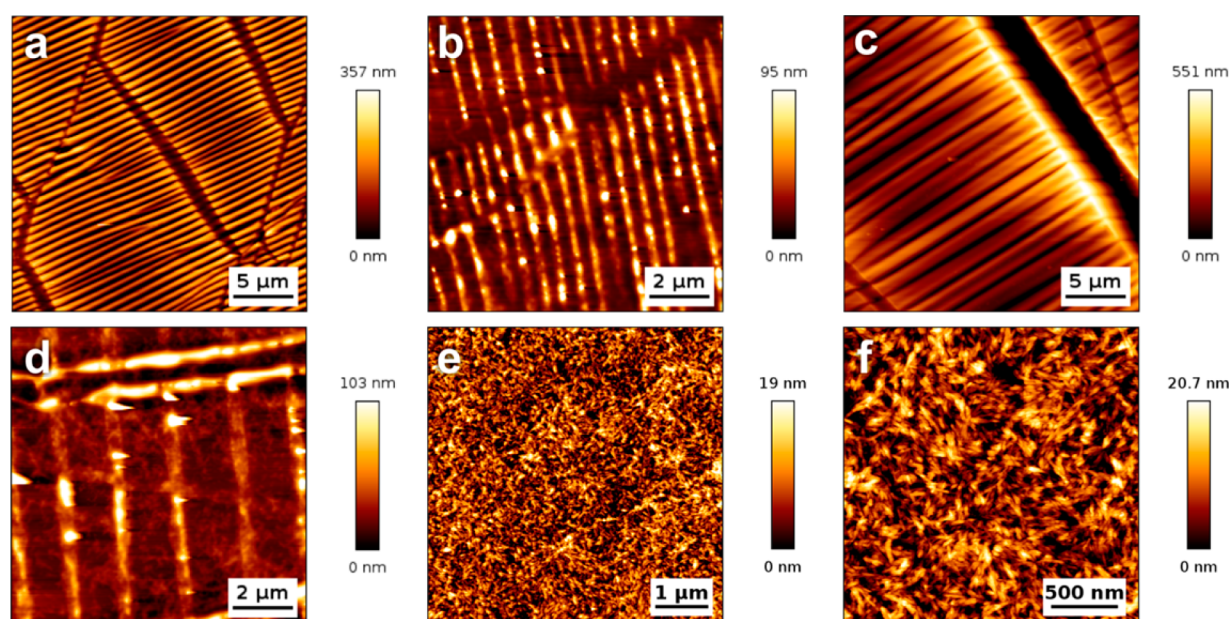


**Figure 4.** (a) AFM height image of wrinkled PDMS substrate (periodicity 704 nm) with PEO/CNC in the wrinkles. (b) AFM height image of a PAE/PEI coated glass substrate after the template in (a) has been stamped onto it. (c) AFM height image of wrinkled PDMS (periodicity 1.37 μm) with CNC/PEO. (d) AFM height image of a PAE/PEI coated glass substrate after the template in (c) has been stamped onto it. (e) and (f) Random CNC spin-coated on PAE/PEI glass substrate.

### 3. RESULTS AND DISCUSSION

**3.1. Stamping Process and Optimization of the Transfer Polymers.** Initially, a similar approach developed by Nystrom et al.<sup>24</sup> was followed to create aligned CNC surfaces. The process of making aligned CNC is depicted as a sequential process (further details in the [Experimental Section](#)) in [Figure 1](#).

Aligned CNC on PEI coated glass substrate was fabricated ([Figure 2a–c](#)) following the method of Nystrom et al.,<sup>24</sup> whereby CNCs were transferred from a wrinkled PDMS substrate to a glass slide that had been spin-coated with a cationic polyelectrolyte, poly(ethylene imine), via wet stamping. To alleviate the problem of low transfer efficiencies of the CNCs, we added an additional step wherein the PDMS wrinkled stamp was first spin coated with poly(ethylene oxide) to act as a release agent. This resulted in considerably increased transfer efficiencies during the wet stamping process. It can be seen in [Figure 2c,d](#) that the aligned CNC surfaces thus created show high levels of order and an excellent recreation of the aligned features of the PDMS template.

However, when testing the wettability properties of these surfaces with water, it is seen that significant spread of the CNCs ([Figure 2e,f](#)) occurred when 10 μL of deionized water was flushed onto the CNC/PEI surface. This indicates that the surface is not robust when wetted by water, thus motivating the exploration of an alternative cationic polymer on the glass substrate to bond the CNCs in place.

Poly(amidoamine) epichlorohydrin (PAE) bonds covalently with CNC when heated to >100 °C,<sup>34</sup> thus enhancing the stability of CNCs on a glass surface that has been precoated with this polymer. Aligned CNC was hence fabricated on glass substrates that had been spin coated with a 1 wt % PAE solution ([Figure 3a,b](#)). The level of CNC alignment and the replication of the template features are retained, as for the samples prepared with PEI.

The stability of the PAE-mediated surfaces against flushing with water (10 μL) was tested, and it could be observed that although the CNCs take on some water (hence the apparent swelling and decrease in image quality in [Figure 3c](#)), distortions were not seen when compared to the CNC/PEI surface and the aligned patterning remained intact. This indicates that PAE is a better choice for achieving CNC patterned surfaces that are

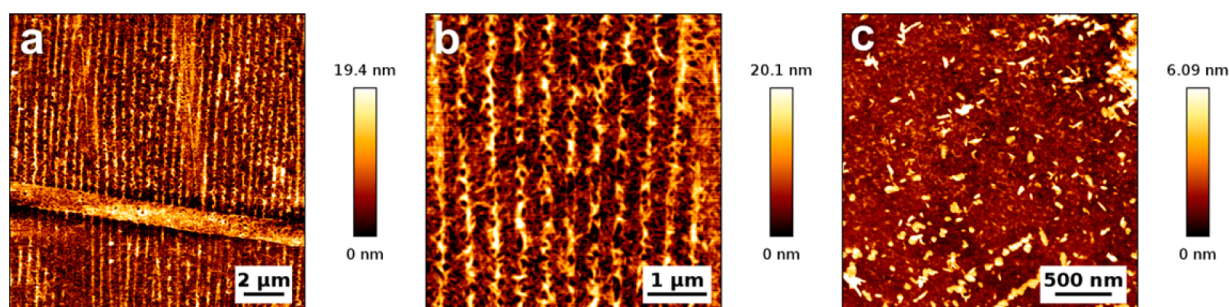


**Figure 5.** (a), (b) AFM height images showing the alignment of CNCs on a PAE-coated glass slide from a PDMS wrinkled template with periodicity 444 nm. The broad horizontal line in (a) is a defect caused by the strain relaxation. (c) AFM image of random CNC on a PAE-coated glass slide.

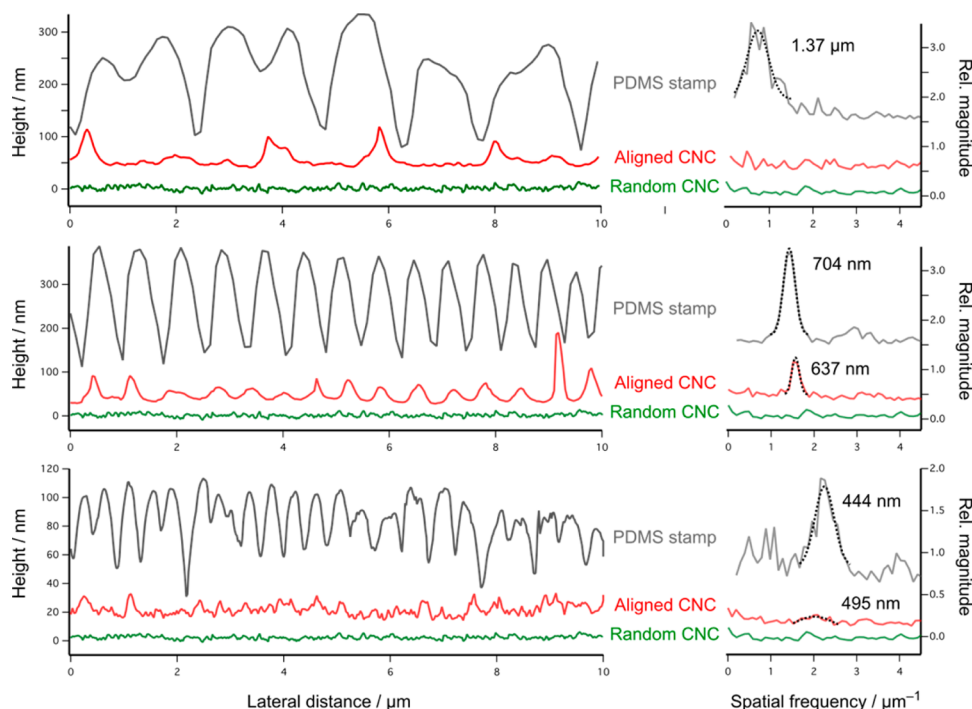


**Figure 6.** Graphs on the left show AFM height cross sections for different wrinkled surfaces, and the graphs on the right depict the corresponding spatial Fourier transform (FT), allowing comparison of the periodicity for wrinkled PDMS and stamped surfaces along with random CNC surfaces.

stable to water. A high concentration of PAE makes the surface appear “stickier” (as evidenced by AFM imaging) potentially through increased hygroscopicity; a concentration of 0.5 wt % PAE was found to be optimal (Figure 3c).

**3.2. Periodicity, Defects, and Ordering.** One of the most appealing characteristics of the PDMS wrinkling procedure for template formation is that the periodicity of the wrinkles can be readily controlled by the stretching<sup>22</sup> and oxidation conditions.<sup>23</sup> To better understand the relationship between template periodicity, CNC transfer and surface properties, PDMS “stamps” with a range of periodicities were prepared and utilized. CNC was spin-coated on a wrinkled PDMS substrate with a periodicity of 704 nm (Figure 4a) and the stamped aligned CNC on a PAE/PEI coated surface can be seen in Figure 4b, with a periodicity of 637 nm. In this instance, we used a combination of the two above studied cationic polyelectrolytes, PAE and PEI, because using PAE alone produced a surface that was much “stickier” and with inconsistent reproduction of the template periodicity. Hence to optimize the surface chemistry, PEI was combined with PAE, which facilitates the adsorption of CNC onto the glass surface

using covalent bonding as well as electrostatic interactions. Reproduction of the template features is generally quite good, and the level of order (quantified below) is high.

When moving to larger wrinkle periodicities, different behavior is seen. Micrometre-scale wrinkled PDMS coated with CNC (Figure 4c) with a periodicity of 1.37  $\mu\text{m}$  (almost exactly twice the wavelength of the previous wrinkles) was stamped onto a PAE/PEI coated glass substrate to obtain aligned CNC (Figure 4d). Although the overall transfer efficiency is comparable to that obtained using the 704 nm templates, the level of order of the final CNC surface is quite low, and it can be seen that nonaligned CNCs coexist with the aligned crystals on the substrate.

For comparison, randomly distributed CNC surfaces were prepared by spin coating CNC onto the same polymer-coated slides. The randomness of CNC could be seen on the glass substrate (Figure 4e,f) coated with PAE/PEI where CNC was just spin-coated (i.e., in the absence of template-mediated transfer). At the low concentrations of CNC used, there is no evidence of local alignment due to the packing of crystals or the shear field induced during spin coating, and a completely



random distribution of the CNC is obtained. This is a useful “blank” for comparing the properties of the aligned CNC surfaces to a randomly oriented CNC surface with the same underlying chemistry. This is discussed in more detail in the sections below.

A pertinent question for the alignment of CNCs concerns the conditions when the periodicity is of the same order as the crystal length (typically  $\sim 175$  nm for our materials).<sup>35</sup> To this end, aligned CNCs were fabricated on glass surfaces coated with 0.5 wt % PAE from a wrinkled stamp with a periodicity of  $\sim 450$  nm (Figure 5a,b). Two interesting features are evident from these measurements. First, as the wrinkles are naturally much more shallow for surfaces with lower wavelength, the alignment of CNCs within the template grooves is much poorer, and as a result, the CNCs on the surface after transfer show much lower levels of ordering (Figure 5b). The CNCs are still concentrated within lines that correspond to the wrinkles of the template, but their orientation is somewhat random. Second, the defect features introduced by the slight anisotropy of the stretching process—that lie perpendicular to the wrinkles—are reproduced on the stamped surface (Figure 5a). These defects result from the slight contraction/expansion in the axis perpendicular to the stretching axis during the template preparation procedure.<sup>36</sup>

For comparison, Figure 5c shows CNCs spin coated onto an identical PAE coated slide without the influence of a template, and a truly random distribution of the crystals is seen.

The periodicity and level of ordering of the precursor wrinkled PDMS templates and the stamped surfaces were explored using a Fourier transform (FT) analysis. For this, line profiles were extracted from AFM images for each type of wrinkled substrate and surface as described above (Figure 6, LHS) and the corresponding spatial frequency FT was calculated (Figure 6, RHS). For each of the surfaces created, periodicities before stamping and after stamping were almost the same with slight differences, which was also seen for the work reported by Nystrom et al.<sup>24</sup>

When comparing the three different periodicities, it is clear that the 704 nm wrinkled PDMS gave the strongest ordering of aligned CNCs, creating 637 nm aligned CNC surfaces. The highly regular wrinkling of the surface is evident in the line profile of the PDMS template, and the strong and clearly resolved peaks in the Fourier transform of both the template and stamped surface indicate strong ordering. For the smaller periodicity ( $\sim 450$  nm), the level of order for the stamped surface, as indicated by the Fourier transform, is much lower. This corroborates the AFM imaging in Figure 5, where the shallow stamp features result in weak local alignment of the CNCs. The template with the largest wavelength ( $1.37 \mu\text{m}$ ) showed the poorest ordering, in both the PDMS stamp itself, and the aligned CNC surface created. It is clear from the line profile of the PDMS that the wrinkles are not regular, presumably because the relaxation from such a large strain was locally nonuniform. This results in poorly ordered surfaces after stamping, and the Fourier transform of the stamped surface does not show a peak for the periodicity of the aligned CNCs, at least over the same length-scale as for the other surfaces ( $10 \mu\text{m}$ ). From these data, we see that the level of alignment generated is indeed sensitive to the initial template dimensions and their relationship to the dimensions of the CNCs.

**3.3. Wetting and Contact Angle Hysteresis.** In order to understand how the alignment of CNCs affects their wetting

properties when used in coatings, contact angle measurements were carried out. For the smallest wavelength of aligned CNC ( $495$  nm), the advancing contact angle of a  $3 \mu\text{L}$  sessile water droplet was measured to be  $81.5 \pm 5.7^\circ$  when the profile was measured in the direction parallel to the alignment axis of the CNC on PAE, and  $84.8 \pm 2.6^\circ$  perpendicular to the direction of alignment (see Supporting Information, Figure S1). Given how many CNC features the droplet interacts with on the surface (and the fact that a  $3 \mu\text{L}$  water droplet in air is far below its capillary length and hence difficult to deform), it is unsurprising that the contact angle is essentially the same when measured parallel and perpendicular to the axis of alignment.

To contextualize the measured contact angle, it is important to also examine a series of control samples. These control samples (see Figure S2) consist of random CNC on PAE-coated glass, PEO on glass, and PAE on glass. These are required to determine whether the alignment has an effect on the wettability of CNC, and whether the polymers used for transfer and release of the CNCs from the template/to the surface confer any effect. It was found that random CNCs had an advancing contact angle of  $19.75 \pm 6.8^\circ$ , indicating that alignment has a huge effect on the wettability of CNC-coated surfaces. The polymer used to aid release of the CNCs from the template, PEO had a contact angle of  $11.8 \pm 1^\circ$ , and PAE prepared as for the coated surfaces (i.e., including the thermal reaction step) showed a contact angle of  $23.91 \pm 1.4^\circ$ . It is therefore clear that the polymers used do not hydrophobize the surface compared to the random CNCs, and we can be confident that any effect on the wettability is due to alignment of the CNCs, rather than any specific component used.

The results significantly demonstrate that just by aligning CNCs, the wettability of a coated surface can be decreased prominently without altering the chemical structure of the CNCs themselves. Such a drastic difference in the contact angle is attributed to a contact line pinning effect, which has been reported earlier in other kinds of structured surfaces.<sup>37–40</sup> To further explore the pinning effect, contact angle hysteresis (CAH) analysis was carried out (Figure 7a). For these measurements, droplets were grown and shrunk in precise increments to observe the contact angle of the advancing and receding contact line. It can be seen that there is comparatively large difference between the advancing and receding contact angles for the aligned CNC surface ( $495$  nm periodicity) on a PAE coated glass substrate, and again no statistically significant difference was detected when measuring in the direction and perpendicular to the axis of alignment. These data demonstrate strong evidence for pinning of the contact line, which results in a large hysteresis between the advancing and receding contact angle. Such pinning effects are characterized by the jumping of the contact line from one pinned position to the next, which is sensitive to surface patterning and the free energy barrier that impedes contact line motion.<sup>41</sup>

To determine whether any chemically specific effects other than simple geometrical pinning are seen on the aligned CNC/PAE surface, a thin layer of gold around  $5$  nm thick was coated on the top of the surface using a sputter-coater, and contact angle analysis was again carried out (Figure 7b). It could be seen that apart from the slight increase in average contact angle in the advancing series (due to the moderately hydrophobic gold present, which has a typical contact angle of  $84^\circ$  for a freshly prepared, smooth sputtered surface),<sup>42</sup> the hysteresis profile showed no other deviation in behavior. The advancing angles were relatively consistent as the droplet was grown,

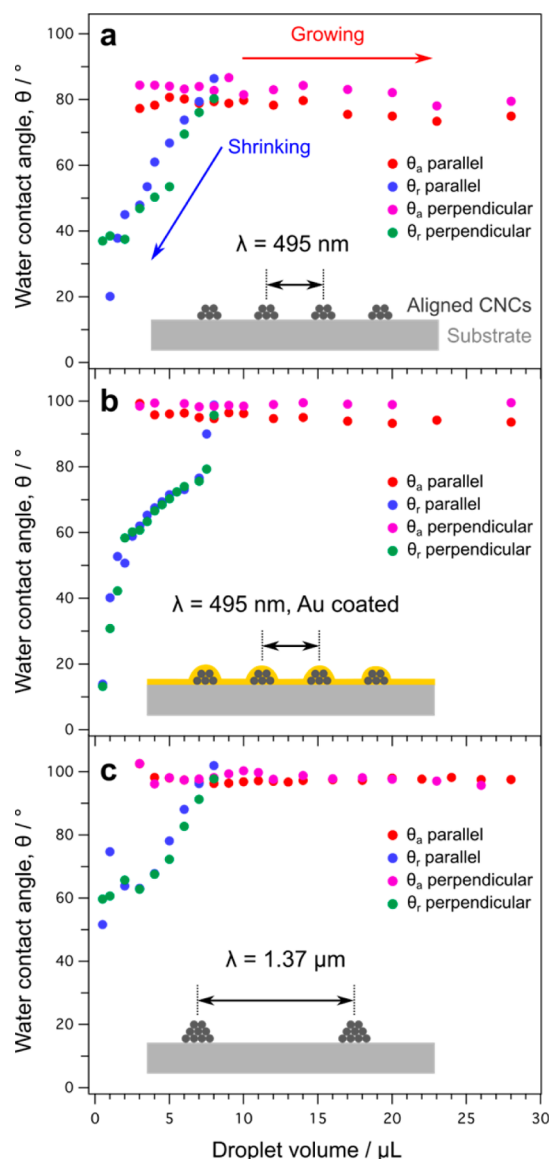


**Figure 7.** Contact angle hysteresis plots of (a) Aligned nanowrinkled CNC on PAE coated glass surface. (b) Gold sputtered aligned nanowrinkled CNC on PAE surface. (c) Aligned microwrinkled CNC on PAE/PEI coated glass surface. In all cases, the large difference in advancing and receding angle or the contact angle hysteresis is attributed to heavy pinning effects. The inset shows the spacing between the CNC features;  $\theta_a$  refers to the advancing angle, and  $\theta_r$  refers to the receding angle.

whereas a gradual decrease in contact angle was seen for receding angles.

As a result of large contact angle hysteresis, water droplets tend to stick on the surface, which is reflected in the average critical roll-off angles measured to be  $42.5 \pm 2.2^\circ$  and  $44.3 \pm 2.2^\circ$  in the direction and perpendicular to the aligned CNC on PAE coated glass surface, respectively. Unlike contact angle measurement, roll-off angle measurements tend to be very dependent on droplet size, as the balance of gravity against the critical pinning energy determines the point at which roll-off occurs. In these measurements, a  $3 \mu\text{L}$  water droplet was used to calculate the roll-off angle, so it would be expected that smaller drops would show a higher critical angle.

Having determined that alignment appears to strongly affect the wetting behavior of CNC coatings, we explored whether periodicity had a role to play. The contact angle hysteresis plot (Figure 7c) for CNC aligned with a period of  $1.37 \mu\text{m}$  shows the large difference between advancing and receding angles, both in the direction (parallel) and perpendicular to the aligned CNC on a PAE/PEI coated glass substrate. As for the smaller wavelength aligned CNCs, the contact line does not change significantly in the advancing profile, whereas it gradually decreases when the contact line is receding. The heavy pinning effects that result in this were also evidenced with high average critical roll-off angles measured to be  $40.8 \pm 4.3^\circ$  and  $40.0 \pm 3.7^\circ$  in the direction and perpendicular to the aligned CNC on the PAE/PEI coated surface, respectively. The maximum advancing angle was slightly higher for the CNCs aligned with larger spacing, which corroborates the AFM imaging showing poorer average orientational alignment for the smaller wavelength surface.

The aligned CNC sample with intermediate spacing that showed the highest level of ordering ( $637 \text{ nm}$ ) gave a similar hysteresis profile to that of the  $1.37 \mu\text{m}$  aligned CNC surface, with average critical roll-off angles of  $43.8 \pm 3.6^\circ$  and  $44.6 \pm 2.7^\circ$  parallel and perpendicular to the aligned CNC on a PAE/PEI coated surface, respectively. The results of these tests are summarized graphically in Figure 8a.

It has been shown previously that water droplets are seldom “sticky” (i.e., strongly adhered to surfaces, characterized by high roll-off angles) even at high contact angles, when pinning defects are not present.<sup>43</sup> Conversely, pinning can be strongly induced by defects in surface topology or chemistry. In our case, in addition to the aligned CNCs that we assume are responsible for most of the pinning effects that result in contact angle hysteresis, defects are also caused by the rate at which the strain was relaxed after plasma treatment. Slower strain rates during relaxation tend to result in fewer defects.<sup>36</sup>

The summarized contact angle and roll-off angle data shown for the aligned surfaces and control samples in Figure 8a shows that the contact angle hysteresis is comparatively lower for the control samples: PAE/PEI, PAE, random CNC on PAE and PAE/PEI surfaces, where pinning effects are not significant. The pinning effects are most extreme for the aligned CNC surfaces with larger periodicities, and interestingly, the lower level of order at the largest feature wavelength ( $1.37 \mu\text{m}$ ) does not inhibit the pinning process, and may even enhance it.

The hypothesized pinning effects were visualized by taking photos of the plan view of a drying droplet using a simple optical microscope at one second intervals in time. The droplet contact line on the substrate was electronically extracted and consolidated to form a single image profile (Figure 8b). The figure depicts the pinning effects that act on the edge of the water droplet on the aligned CNC ( $1.37 \mu\text{m}$ )/PAE/PEI surface. It is clear that the contact line does not move smoothly, indicating strong pinning, and the later profiles clearly show where the contact line disconnects from pinning points. This again emphasizes that the apparent hydrophobicity of these aligned CNC surfaces arises from a physical phenomenon related purely to surface morphology, and is not a result of chemical hydrophobization. This mechanism is very different from, for example, the superhydrophobic surfaces generated using hydrophobic materials to achieve a Cassie–Baxter wetting state. Here our surfaces are wholly within the Wenzel wetting regime—whereby the surface is fully wetted by water, but pinning effects result in a high contact angle for the advancing

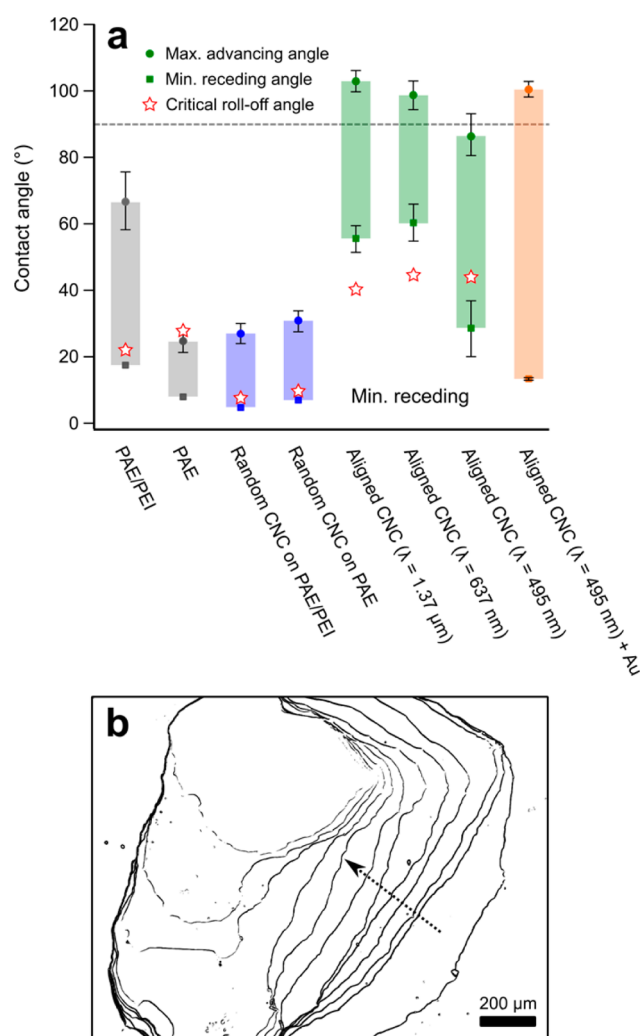


**Figure 8.** (a) The maximum advancing and minimum receding contact angles represented in the form of bar diagram along with critical roll-off angle values. The first four bar diagrams from left represents the control samples and the rest main samples. (b) Edge profiles obtained from micrography of a water droplet drying on the 637 nm aligned CNC surface, demonstrating stick-slip type contact line motion, characteristic of strong pinning effects.

contact line. Using interference contrast microscopy, no evidence for air–water interface or bubbles beneath the drops could be found, confirming the pinned Wenzel hypothesis.

**3.4. Oil Contact Angle and Hysteresis Studies on Aligned CNC Surfaces in Water.** Having explored water contact angles on aligned CNC surfaces and finding such significant effects due to alignment, we sought to analyze how oil droplets behave on such surfaces under water, which may potentially give paths to explore oil–water separation and soil cleaning applications. For this, a customized setup was used (see Figure S3) wherein the surface was placed in a small tank filled with water, and a glass needle was used to generate an oil droplet (2  $\mu\text{L}$ ) underwater on the surface (inset of Figure 9).

As the largest contact angle hysteresis was observed for the aligned CNC on PAE/PEI surface with wavelength 1.37  $\mu\text{m}$ , this was selected as the sample for oil contact angle analysis. The oil contact angle of the blank glass slide was measured to be  $131.7 \pm 9.1^\circ$ , which is expected due to the hydrophilic nature of the silica surface. The glass slide coated with random CNC/PAE/PEI gave an oil contact angle of  $138.9 \pm 6.5^\circ$ . This

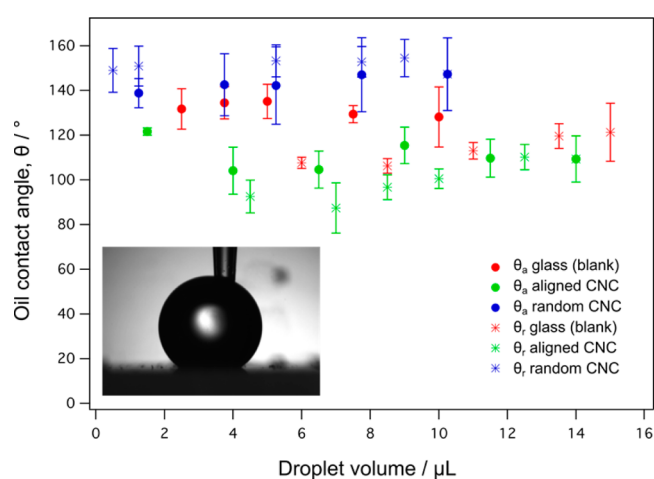


**Figure 9.** Oil contact angle hysteresis plot of aligned microwrinkled CNC on PAE/PEI coated glass surface, random CNC on PAE/PEI surface and the blank glass slide. The difference in advancing and receding angle or the oil contact angle hysteresis was found to be much lower, proving such surfaces to be used potentially for oil–water separation applications. The inset shows how the sessile droplet of oil resides on the surface in water.  $\theta_a$  refers to advancing angle and  $\theta_r$  refers to receding angle.

modest increase can be attributed to the random CNC being slightly more hydrophilic than the glass substrate, thus increasing the oil contact angle. An oil-in-water contact angle value of  $121.6 \pm 1.7^\circ$  was observed for aligned CNC on the PAE/PEI coated glass surface. As the CNC is aligned and covers less of the surface, the hydrophilic regions will be much smaller compared to the random CNC sample, hence resulting in lower oil contact angle value.

To determine the oil-in-water contact angle hysteresis, advancing and receding oil contact angles were plotted as a function of oil droplet size (Figure 9). It can be seen that all the samples showed very little contact angle hysteresis with oil droplets, indicating that alignment has little impact on the oil wettability of CNC surfaces. Darmanin et al.<sup>44</sup> also observed that maximum oil contact angles could not be achieved with micro patterned surfaces, where oils of low surface tension showed only slight changes in their contact angles.

Our results here indicate two important features: first, the innate hydrophilicity of the surface components is retained, evidenced by their very high contact angle with oil under water. It is more favorable for the surfaces to be wet by water than oil, again emphasizing the fact that the apparent surface hydrophobicity in air arises from the surface structure rather than the surface chemistry. Second, this implies that such surfaces will resist fouling by oil under water—a traditional disadvantage of chemically hydrophobized surfaces, whereby the lower surface energies result in effective wetting by oils. We thus have a unique set of surface properties, that make this method of hydrophobization appealing for a range of applications.

## 4. CONCLUSIONS

Surfaces comprising regularly aligned cellulose nanocrystals (CNCs) were prepared via the use of wrinkled poly-(dimethylsiloxane), PDMS “stamps” as templates, using cationic polyelectrolytes to facilitate the transfer of CNCs from the template to a glass surface, combined with poly(ethylene oxide), PEO as a release agent. The use of poly(amidoamine) epichlorohydrin (PAE)/polyethylenimine



(PEI) complexes as a surface coating to aid transfer was shown to provide surfaces that were more stable to water compared to poly(ethylene imine) PEI coatings. Wettability studies using contact angle measurements showed that without changing the chemical structure of CNC, the wettability could be altered just by alignment. CNC in micron-scale patterns showed a significantly higher average contact angle ( $\sim 100^\circ$ ) than a surface of randomly oriented CNCs ( $\sim 30^\circ$ ). The greatest degree of ordering of CNCs was achieved using a PDMS stamp with wavelength 704 nm.

The stark increase in contact angle on alignment of the CNCs is attributed to strong pinning effects, visualized directly for drying droplets on the surfaces, and which were reflected in large contact angle hysteresis and high average roll-off angles. In contrast, the contact angle hysteresis of an oil droplet in water was very low, indicating that the surfaces would not be prone to oil fouling if used as underwater coatings.

It has thereby been shown that through simple alignment, the wettability of a surface coated with CNCs can be dramatically reduced, and the ability to retain water (as evidenced by the large roll-off angles) is increased. Significantly, the template and polymer-mediated fabrication method lends itself to rotogravure style printing, offering wide scope for scalable and cheap application using full roll-to-roll technology.

Such aligned CNC surfaces could find uses in coatings, as they are transparent and have the unique wettability characteristics described above. The template itself could be used to align other materials such as biomacromolecules for sensor applications. A particularly appealing feature is that these surfaces would facilitate high-resolution printing, as the high advancing contact angle of liquid droplets means that incident drops do not spread; such spreading results in the "bleeding" of ink that currently limits printing resolution. Further avenues of investigation could include changing the underlying substrate chemistry to further optimize the wettability characteristics and surface properties.

## ■ ASSOCIATED CONTENT

### ■ Supporting Information

The Supporting Information is available free of charge on the ACS Publications website at DOI: 10.1021/acsami.7b03094.

Contact angle images of aligned nanowrinkled and microwrinkled CNC, contact angle images of control samples, and oil contact angle images including the measuring setup (PDF)

## ■ AUTHOR INFORMATION

### ■ Corresponding Author

\*Tel: [REDACTED] E-mail: [REDACTED]  
(R.F.T.).

### ■ ORCID

Rico F. Tabor: 0000-0003-2926-0095

### ■ Funding

This work was supported in part by the award of an ARC Future Fellowship to R.F.T.

### ■ Notes

The authors declare no competing financial interest.

## ■ ACKNOWLEDGMENTS

R.P. acknowledges State Government of Victoria for the award of Victoria India Doctoral Scholarship, and the Monash Centre

for Atomically Thin Materials for a top-up scholarship. This work was supported in part by a Future Fellowship (R.F.T.) grant from the Australian Research Council (FT160100191).

## ■ ABBREVIATIONS

CNCs, cellulose nanocrystals  
PEO, poly(ethylene oxide)  
PAE, poly(amidoamine) epichlorohydrin  
PEI, polyethylenimine  
PDMS, polydimethylsiloxane  
AFM, atomic force microscopy  
FT, Fourier transform

## ■ REFERENCES

- (1) Lagerwall, J. P. F.; Schutz, C.; Salajkova, M.; Noh, J.; Hyun Park, J.; Scalia, G.; Bergstrom, L. Cellulose Nanocrystal-Based Materials: from Liquid Crystal Self-Assembly and Glass Formation to Multifunctional Thin Films. *NPG Asia Mater.* **2014**, *6*, e80.
- (2) Shopsowitz, K. E.; Qi, H.; Hamad, W. Y.; MacLachlan, M. J. Free-Standing Mesoporous Silica Films with Tunable Chiral Nematic Structures. *Nature* **2010**, *468*, 422–425.
- (3) Šturcová, A.; Davies, G. R.; Eichhorn, S. J. Elastic Modulus and Stress-Transfer Properties of Tunicate Cellulose Whiskers. *Biomacromolecules* **2005**, *6*, 1055–1061.
- (4) Dhar, N.; Au, D.; Berry, R. C.; Tam, K. C. Interactions of Nanocrystalline Cellulose with an Oppositely Charged Surfactant in Aqueous Medium. *Colloids Surf., A* **2012**, *415*, 310–319.
- (5) Habibi, Y.; Lucia, L. A.; Rojas, O. J. Cellulose Nanocrystals: Chemistry, Self-Assembly, and Applications. *Chem. Rev.* **2010**, *110*, 3479–3500.
- (6) Salajkova, M.; Berglund, L. A.; Zhou, Q. Hydrophobic Cellulose Nanocrystals Modified with Quaternary Ammonium Salts. *J. Mater. Chem.* **2012**, *22*, 19798–19805.
- (7) Schweikart, A.; Horn, A.; Böker, A.; Fery, A. Controlled Wrinkling as a Novel Method for the Fabrication of Patterned Surfaces. *Adv. Polym. Sci.* **2009**, *227*, 75–99.
- (8) Hoogenboom, J. P.; Rétif, C.; de Bres, E.; van de Boer, M.; van Langen-Suurling, A. K.; Romijn, J.; van Blaaderen, A. Template-Induced Growth of Close-Packed and Non-Close-Packed Colloidal Crystals during Solvent Evaporation. *Nano Lett.* **2004**, *4*, 205–208.
- (9) Hoogenboom, J. P.; van Langen-Suurling, A. K.; Romijn, J.; van Blaaderen, A. Hard-Sphere Crystals with Hcp and Non-Close-Packed Structure Grown by Colloidal Epitaxy. *Phys. Rev. Lett.* **2003**, *90*, 138301.
- (10) Hoogenboom, J. P.; van Langen-Suurling, A. K.; Romijn, J.; van Blaaderen, A. Epitaxial Growth of a Colloidal Hard-Sphere Hcp Crystal and the Effects of Epitaxial Mismatch on Crystal Structure. *Phys. Rev. E* **2004**, *69*, 051602.
- (11) Hynninen, A.-P.; Thijssen, J. H. J.; Vermolen, E. C. M.; Dijkstra, M.; van Blaaderen, A. Self-Assembly Route for Photonic Crystals with a Bandgap in the Visible Region. *Nat. Mater.* **2007**, *6*, 202–205.
- (12) van Blaaderen, A. Colloids Under External Control. *MRS Bull.* **2004**, *29*, 85–90.
- (13) Cerda, E.; Mahadevan, L. Geometry and Physics of Wrinkling. *Phys. Rev. Lett.* **2003**, *90*, 074302.
- (14) Glatz, B. A.; Tebbe, M.; Kaoui, B.; Aichele, R.; Kuttner, C.; Schedl, A. E.; Schmidt, H.-W.; Zimmermann, W.; Fery, A. Hierarchical Line-Defect Patterns in Wrinkled Surfaces. *Soft Matter* **2015**, *11*, 3332–3339.
- (15) Rodríguez-Hernández, J.; del Campo, A. Fabrication of Hierarchical Wrinkled Morphologies Through Sequential UVO Treatments. *J. Appl. Polym. Sci.* **2015**, *132*, 41863.
- (16) Watanabe, M. Wrinkles Formed on a Thin Gold Film Deposited onto Stretched Elastic Substrates. *Polym. Adv. Technol.* **2005**, *16*, 744–748.

- (17) Martin, G. C.; Su, T. T.; Loh, I. H.; Balizer, E.; Kowel, S. T.; Kornreich, P. The Metallization of Silicone Polymers in the Rubbery and the Glassy State. *J. Appl. Phys.* **1982**, *53*, 797–799.
- (18) Hedden, R. C.; Saxena, H.; Cohen, C. Mechanical Properties and Swelling Behavior of End-Linked Poly(diethylsiloxane) Networks. *Macromolecules* **2000**, *33*, 8676–8684.
- (19) Bowden, N.; Brittain, S.; Evans, A. G.; Hutchinson, J. W.; Whitesides, G. M. Spontaneous Formation of Ordered Structures in Thin Films of Metals Supported on an Elastomeric Polymer. *Nature* **1998**, *393*, 146–149.
- (20) Bowden, N.; Huck, W. T. S.; Paul, K. E.; Whitesides, G. M. The Controlled Formation of Ordered, Sinusoidal Structures by Plasma Oxidation of an Elastomeric Polymer. *Appl. Phys. Lett.* **1999**, *75*, 2557–2559.
- (21) Genzer, J.; Efimenko, K. Creating Long-Lived Superhydrophobic Polymer Surfaces Through Mechanically Assembled Monolayers. *Science* **2000**, *290*, 2130–2133.
- (22) Lu, C.; Mohwald, H.; Fery, A. A Lithography-Free Method for Directed Colloidal Crystal Assembly Based on Wrinkling. *Soft Matter* **2007**, *3*, 1530–1536.
- (23) Horn, A.; Schobert, H. G.; Hiltl, S.; Chiche, A.; Wang, Q.; Schweikart, A.; Fery, A.; Boker, A. Nanostructured Wrinkled Surfaces for Templating Bionanoparticles—Controlling and Quantifying the Degree of Order. *Faraday Discuss.* **2009**, *143*, 143–150.
- (24) Nyström, G.; Fall, A. B.; Carlsson, L.; Wågberg, L. Aligned Cellulose Nanocrystals and Directed Nanoscale Deposition of Colloidal Spheres. *Cellulose* **2014**, *21*, 1591–1599.
- (25) Habibi, Y.; Heim, T.; Douillard, R. AC Electric Field-Assisted Assembly and Alignment of Cellulose Nanocrystals. *J. Polym. Sci., Part B: Polym. Phys.* **2008**, *46*, 1430–1436.
- (26) Munier, P.; Gordeyeva, K.; Bergström, L.; Fall, A. B. Directional Freezing of Nanocellulose Dispersions Aligns the Rod-Like Particles and Produces Low-Density and Robust Particle Networks. *Biomacromolecules* **2016**, *17*, 1875–1881.
- (27) Wanasekara, N. D.; Santos, R. P. O.; Douch, C.; Frollini, E.; Eichhorn, S. J. Orientation of Cellulose Nanocrystals in Electrospun Polymer Fibres. *J. Mater. Sci.* **2016**, *51*, 218–227.
- (28) Reising, A. B.; Moon, R. J.; Youngblood, J. P. Effect of Particle Alignment on Mechanical Properties of Neat Cellulose Nanocrystal Films. *J. Sci. Technol. For Prod. Process.* **2012**, *2*, 32–41.
- (29) Revol, J.-F.; Godbout, L.; Dong, X.-M.; Gray, D. G.; Chanzy, H.; Maret, G. Chiral Nematic Suspensions of Cellulose Crystallites; Phase Separation and Magnetic Field Orientation. *Liq. Cryst.* **1994**, *16*, 127–134.
- (30) Kvien, I.; Oksman, K. Orientation of Cellulose Nanowhiskers in Polyvinyl Alcohol. *Appl. Phys. A: Mater. Sci. Process.* **2007**, *87*, 641–643.
- (31) De France, K. J.; Yager, K. G.; Hoare, T.; Cranston, E. D. Cooperative Ordering and Kinetics of Cellulose Nanocrystal Alignment in a Magnetic Field. *Langmuir* **2016**, *32*, 7564–7571.
- (32) Cranston, E. D.; Gray, D. G. Formation of Cellulose-based Electrostatic Layer-by-Layer Films in a Magnetic Field. *Sci. Technol. Adv. Mater.* **2006**, *7*, 319–321.
- (33) Dhar, P.; Kumar, A.; Katiyar, V. Magnetic Cellulose Nanocrystal Based Anisotropic Polylactic Acid Nanocomposite Films: Influence on Electrical, Magnetic, Thermal, and Mechanical Properties. *ACS Appl. Mater. Interfaces* **2016**, *8*, 18393–18409.
- (34) McLiesh, H.; Sharman, S.; Garnier, G. Effect of Cationic Polyelectrolytes on the Performance of Paper Diagnostics for Blood Typing. *Colloids Surf., B* **2015**, *133*, 189–197.
- (35) Prathapan, R.; Thapa, R.; Garnier, G.; Tabor, R. F. Modulating the Zeta Potential of Cellulose Nanocrystals using Salts and Surfactants. *Colloids Surf., A* **2016**, *509*, 11–18.
- (36) Efimenko, K.; Rackaitis, M.; Manias, E.; Vaziri, A.; Mahadevan, L.; Genzer, J. Nested Self-Similar Wrinkling Patterns in Skins. *Nat. Mater.* **2005**, *4*, 293–297.
- (37) Öner, D.; McCarthy, T. J. Ultrahydrophobic Surfaces. Effects of Topography Length Scales on Wettability. *Langmuir* **2000**, *16*, 7777–7782.
- (38) Ramos, S. M. M.; Charlaix, E.; Benyagoub, A. Contact Angle Hysteresis on Nano-Structured Surfaces. *Surf. Sci.* **2003**, *540*, 355–362.
- (39) Lee, Y.; Park, S. H.; Kim, K. B.; Lee, J. K. Fabrication of Hierarchical Structures on a Polymer Surface to Mimic Natural Superhydrophobic Surfaces. *Adv. Mater.* **2007**, *19*, 2330–2335.
- (40) Kurogi, K.; Yan, H.; Tsujii, K. Importance of Pinning Effect of Wetting in Super Water-Repellent Surfaces. *Colloids Surf., A* **2008**, *317*, 592–597.
- (41) Kusumaatmaja, H.; Yeomans, J. M. Modeling Contact Angle Hysteresis on Chemically Patterned and Superhydrophobic Surfaces. *Langmuir* **2007**, *23*, 6019–6032.
- (42) Tabor, R. F.; Morfa, A. J.; Grieser, F.; Chan, D. Y. C.; Dagastine, R. R. Effect of Gold Oxide in Measurements of Colloidal Force. *Langmuir* **2011**, *27*, 6026–6030.
- (43) t'Mannetje, D.; Ghosh, S.; Lagrauw, R.; Otten, S.; Pit, A.; Berendsen, C.; Zeegers, J.; van den Ende, D.; Mugele, F. Trapping of Drops by Wetting Defects. *Nat. Commun.* **2014**, *5*, 3559.
- (44) Darmanin, T.; Guittard, F.; Amigoni, S.; Tabin de Givenchy, E.; Noblin, X.; Kofman, R.; Celestini, F. Superoleophobic Behavior of Fluorinated Conductive Polymer Films Combining Electropolymerization and Lithography. *Soft Matter* **2011**, *7*, 1053–1057.

# Supporting Information

## Decreasing the wettability of cellulose nanocrystal surfaces using wrinkle-based alignment

*Ragesh Prathapan<sup>α</sup>, Joseph D. Berry<sup>+</sup>, Andreas Fery<sup>β</sup>, Gil Garnier<sup>χ</sup> and Rico F. Tabor<sup>α, \*</sup>*

<sup>α</sup>School of Chemistry, Monash University, Clayton, VIC 3800, Australia.

<sup>+</sup>Department of Chemical and Biomolecular Engineering and the Particulate Fluids Processing Centre, University of Melbourne, Parkville, VIC 3010, Australia

<sup>β</sup>Institute for Physical Chemistry and Polymer Physics, Leibniz-Institut für Polymerforschung Dresden e.V., 01069 Dresden, Germany

<sup>χ</sup>Bioresources Processing Research Institute of Australia (BioPRIA), Department of Chemical Engineering, Monash University, Clayton, VIC 3800, Australia.

### Corresponding Author

\*E-mail for R.F. Tabor: [REDACTED]. Tel: [REDACTED]

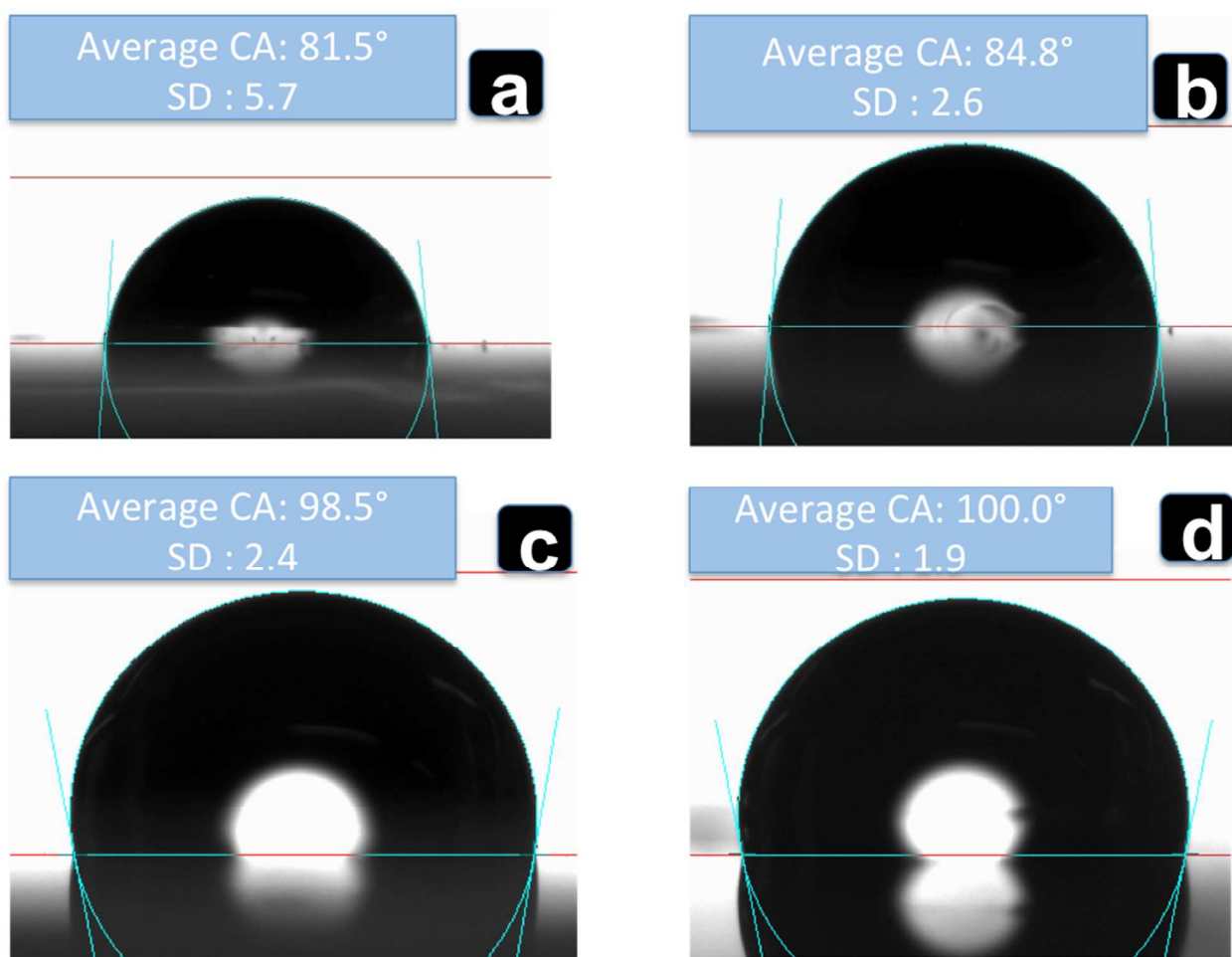


**Figure S1.** Contact angle of the aligned nano-wrinkled CNC (495 nm) on PAE coated glass surface (a) Parallel to the alignment axis. (b) Perpendicular to the alignment axis. Contact angle of the aligned micro-wrinkled CNC (1.37  $\mu\text{m}$ ) on PAE/PEI coated glass surface (c) Parallel to the alignment axis. (d) Perpendicular to the alignment axis.

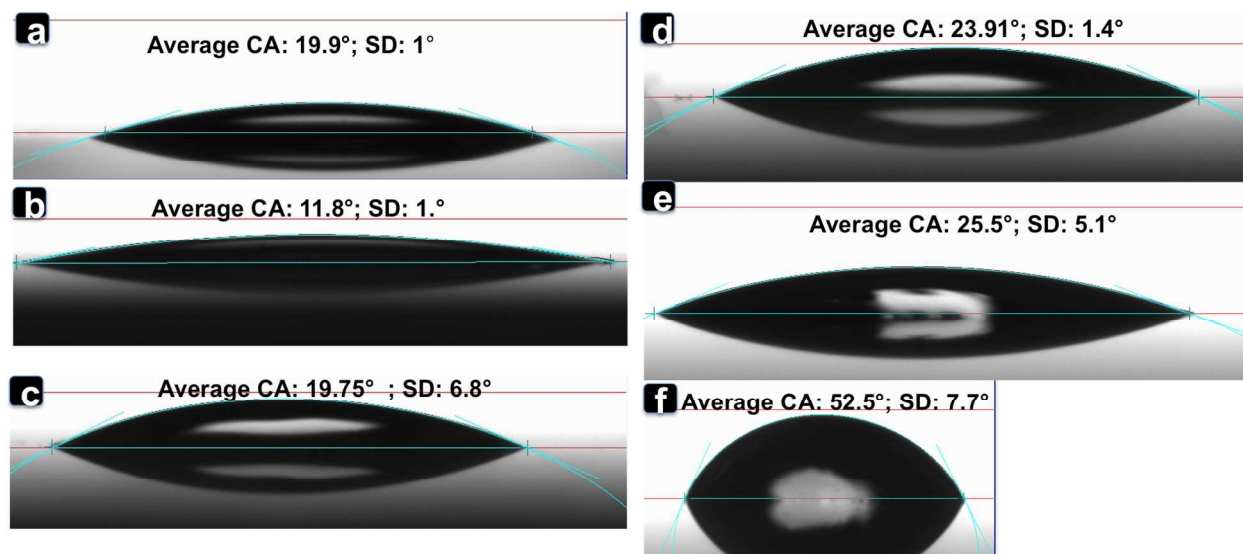


**Figure S2.** Contact angle of control samples (a) normal glass slide. (b) PEO on glass slide. (c) PAE/random CNC on glass slide. (d) PAE on glass slide. (e) PAE/PEI/random CNC on glass slide. (f) PAE/PEI on glass slide.

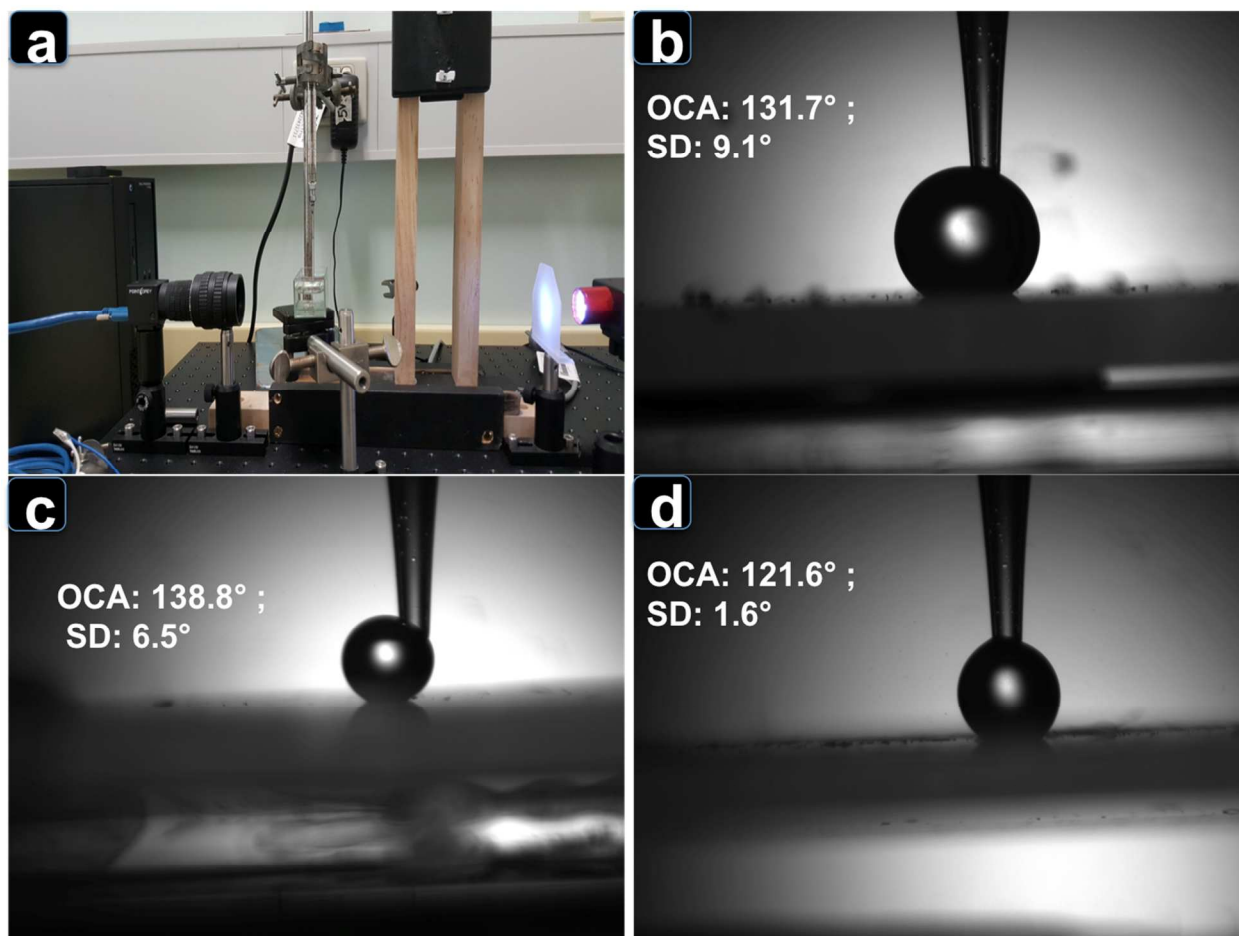
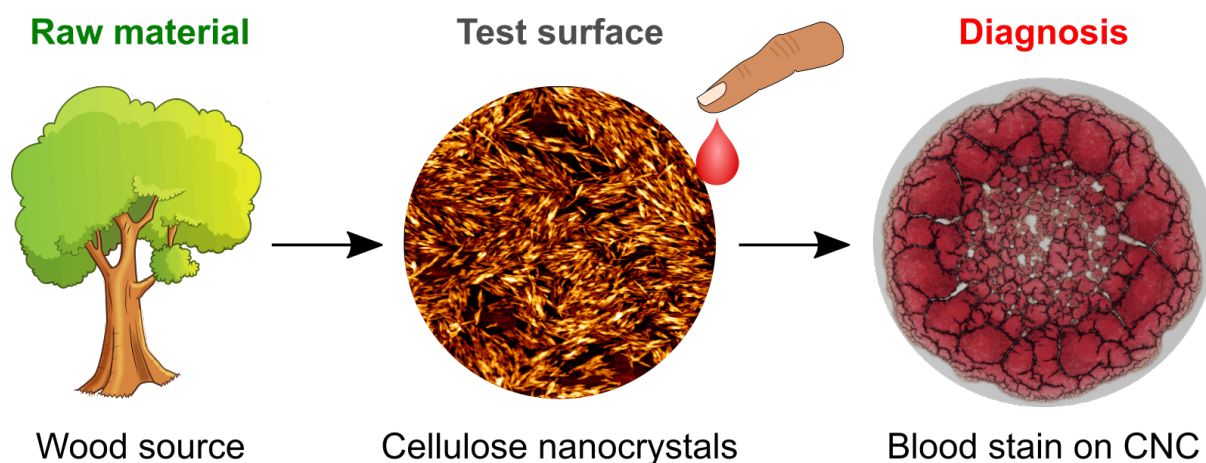


**Figure S3.** (a) Oil contact angle measuring set-up in which the sample surface placed inside water filled glass box and the oil droplet touching the sample surface. The contact angles were measured with oil droplets residing on (b) Blank glass slide, (c) Glass slide coated with random CNC/PAE/PEI and (d) Glass slide coated with aligned CNC/PAE/PEI surface.



## Preface for Chapter 5



In this Chapter, we try to apply the aligned (Chapter 4) and random CNCs as thin transparent coatings for biomedical applications. Conventional paper-based diagnostics face the limitation of wicking of human blood, and hence cannot be further used for morphological studies to clearly visualize individual cells. Here, we investigate the drying mechanism of whole human blood on cellulose nanocrystal coated glass slides and compare these with other surfaces like cellulose acetate, regenerated cellulose, normal glass slides, cationic polyelectrolyte coated glass slides, polystyrene and PTFE surfaces. To understand the effectiveness of cellulose nanocrystal coatings for blood testing, a simple antibody-antigen test is also carried out.

# Surface engineering of transparent cellulose nanocrystal coatings for biomedical applications

*Ragesh Prathapan<sup>α</sup>, Heather McLiesh<sup>β</sup>, Gil Garnier<sup>β\*</sup> and Rico F. Tabor<sup>α, \*</sup>*

<sup>α</sup>School of Chemistry, Monash University, Clayton, VIC 3800, Australia.

<sup>β</sup>Bioresources Processing Research Institute of Australia (BioPRIA), Department of Chemical Engineering, Monash University, Clayton, VIC 3800, Australia.

**KEYWORDS.** cellulose nanocrystals, human blood, pattern formation, diagnostics, wettability, blood typing, nanocellulose

**ABSTRACT.** The concept of blood typing diagnostics using blood drops dried onto transparent cellulose nanocrystal thin film (~ 35 nm) coatings has been demonstrated. The substrate onto which the blood drops are dried plays an important role in such tests, depending on surface composition, roughness and wettability. The drying profile of three different fluid dispersions: model latex particles, reagent blood cells, and whole human blood was studied on a range of different surfaces, including cellulose nanocrystals (CNCs), regenerated cellulose, and several hydrophobic polymers, in order to understand the role of surface chemistry, roughness and fluid dispersion properties. The morphology of these surfaces was investigated



using AFM, roughness was calculated, and wettability was explored via contact angle measurement. The morphology of dried drops of human blood on different cellulosic surfaces was compared in order to understand the importance of cellulose crystallinity. Well defined dried blood drops were observed on random and aligned CNC surfaces, facilitating visualization of individual cells. A simple antibody–antigen test was used to demonstrate the effectiveness of the CNC substrate for blood testing, showing high and reproducible selectivity.

## 1. Introduction

Blood is a non-Newtonian fluid consisting of cells (red, white, platelets) dispersed in a liquid (plasma) containing proteins and inorganic electrolytes.<sup>1,2</sup> The morphology of dried blood drops on solid surfaces is regulated by plasma and the cellular components,<sup>3</sup> and the study of such dried or drying blood patterns has significant applications in forensic investigation,<sup>4,5,6,7</sup> medical practice,<sup>8</sup> DNA microarray printing, *etc.*<sup>9</sup>

Current blood-typing techniques use positive identification of red blood cell agglutination based on antigen-antibody interactions.<sup>10</sup> Centrifugation under laboratory conditions is required for most of the techniques including the column agglutination test, CAT, gel columns, tube test, *etc.*, that makes them unsuited for remote and field testing.<sup>11</sup> CAT tests are time consuming to operate and expensive, in spite of their wide use. Glass slide testing for antigen identification is ineffective due to its lack of sensitivity.<sup>10</sup>

A major recent advance in the form of paper-based diagnostics have been reported extensively, giving a quick and inexpensive method for medical diagnostics that rely on the principles of hemagglutination.<sup>12</sup> To recognize and analyze biomolecules, different forms of paper including fabrics, cellulosic films, cardboard, *etc.* have been used.<sup>13</sup> Analysis of dried blood on paper for diagnostic purposes has been shown to be effective in screening many diseases including HIV<sup>14</sup> and Pompe disease.<sup>15</sup> The paper is sometimes impregnated with

chemicals to lyse the cells in order to better analyse their contents, such as in the case of the Flinders Technology Associates (FTA) card.<sup>16</sup> Blood on paper based diagnostics has also been studied for instantaneous blood typing.<sup>17</sup> Thin and porous papers were investigated for blood-typing diagnostics wherein the paper structure plays a critical role in the performance of the blood typing assay.<sup>18</sup> McLiesh et al. investigated blood typing via paper diagnostics by using a cationic polyelectrolyte to retain biomolecules on paper.<sup>19</sup> An increase in the concentration and charge density of the cationic polyelectrolyte resulted in a non-linear retention of red blood cells on paper. The blood group phenotype of red blood cells using flow-through and direct reporting (via paper-based methods) was studied by Then et al.<sup>10</sup> Optimization of the process parameters including antibody–antigen reaction time, antibody concentration, *etc.* was undertaken in order to identify blood groups.<sup>10</sup> However, the test sensitivity was affected by the non-specific binding of red blood cells to paper, depending on the formulation of antibody solution.

Despite its many advantages, paper is limited as substrate for diagnostic applications, as the analysis of cells by optical microscopy or spectroscopic techniques on such opaque substrates is often challenging. Also, paper diagnostics using metallic nanoparticles requires control of porosity to ensure that nanoparticles are not entrapped. Another issue with these paper diagnostics is its life-time. Studies reported by Khan et al. using enzymatic papers indicate the degradation of enzymatic activity due to a decreased solvent stabilization and increased thermal movement over time.<sup>20</sup>

The present work focuses on thin surface films using cellulosic materials as substrates for blood testing. The study has two objectives: firstly, to engineer the structure of transparent films of cellulose nanocrystals (CNC) to control blood wettability and stain formation (dry/wet); secondly, to test these cellulose surfaces for blood typing applications. To achieve this, the wettability and stain structure of droplets of blood and model fluids over thin films

made of aligned and random CNC were analyzed and compared with model surfaces. Substrates combining the benefits of cellulosic materials with the ability to interrogate individual cells were thereby obtained. Such substrates could serve as portable diagnostic materials amenable for further analysis using imaging techniques, thus increasing possibilities of automated and high-throughput analysis.

## **2. Experimental Details**

### **2.1 Materials**

Cellulose nanocrystals (CNCs, 12.2 wt%) dispersed in water, with sulfur content 1–2% were obtained from the University of Maine Process Development Center. Poly(aminoamide) epichlorohydrin (PAE, 33.5 wt%) was purchased from Nopco Paper Technology. Dichlorodimethylsilane ( $\geq 99.5\%$ ) was obtained from Sigma-Aldrich, and was used to hydrophobize the needle for controlled deposition of biological fluids onto the desired substrates. Anti-A monoclonal grouping reagent for blood typing was purchased from Epiclone, VIC, Australia. Uniform dyed polystyrene microspheres of mean diameter  $0.44\ \mu\text{m}$  were used as model particle solutions, and were purchased from Bangs Laboratories Inc, USA. Phosphate buffered saline (PBS) (1 tablet in 200 mL) was purchased from Sigma-Aldrich, USA. Cellulose acetate, sodium methoxide and acetone were purchased from Sigma-Aldrich, St. Louis, MO, USA. Methanol for analysis purposes was purchased from Merck, Germany. Human EDTA (ethylenediamine tetraacetic acid) whole blood samples (for simplicity we will describe this as ‘human blood’ throughout the rest of this paper) were sourced from the Australian Red Cross Blood Service, Melbourne, VIC. Abtectcell III 3% reagent blood cells were purchased from Seqirus Pty Ltd, VIC, Australia. Poly (ethylene oxide) (PEO, average molecular weight ( $M_v$ )  $400,000\ \text{g mol}^{-1}$ ) was used as release agent for aligned CNC preparation, and was purchased from Sigma-Aldrich, USA. To synthesize

polydimethylsiloxane (PDMS), silicone elastomer curing agent and Sylgard 184 silicone elastomer base (Dow Corning Corporation, USA) were used and prepared as per the manufacturer's supplied instructions.

## **2.2 Instrumental techniques**

For morphological analysis of the substrates used, atomic force microscopy (AFM, JPK Nanowizard 3) was used in alternating contact, AC mode. Bruker NCHV tapping mode cantilevers were employed. The CNC and cellulose acetate coatings on glass substrates were prepared using a spin coater (Laurell technologies, WS-400BZ-6NPP/LITE). An air plasma chamber (model PDC 002, Harrick Scientific Corporation, USA) with 30 W plasma power was used to hydrophilize the glass substrates as well as for preparation of aligned CNC on glass substrates. A customized-set up was used to measure the contact angle of the biological liquids on various substrates. Optical microscopy was used to investigate the blood drop drying process, using a standard optical microscope operating in transmission or reflection mode (Kozo XJP-300) coupled to a CMOS camera (Flea3, Point Grey, Richmond BC, Canada). The blood spots used for testing the blood typing protocol were visualized using a Nikon optical microscope (DS\_R12). The transparency of the prepared coatings on glass substrates was analyzed using UV-visible spectroscopy (Agilent Technologies, Cary 60 UV-vis), scanned across the wavelength range 300 nm to 800 nm. An orbital shaker (WiseShake<sup>R</sup>, Thermoline Scientific) was used to ensure reproducibility during the blood testing protocol for PBS washing of the samples.

## **2.3 CNC coating preparation**

Surfaces coated with aligned CNCs were prepared as described in our previous work.<sup>26</sup> Briefly, the PDMS was uniaxially stretched and then oxidized using plasma treatment;

thereafter releasing the strain resulted in well ordered, wrinkled surfaces. Onto these, PEO and CNC were deposited using spin-coating (2500 rpm, 1 minute). The PDMS was then wet stamped onto a PAE-coated glass substrate whereby CNC transfer to the glass substrate was facilitated using a tiny droplet of water. Surfaces coated with randomly oriented CNCs were prepared by spin-coating 5 mg/mL CNC dispersion at 2500 rpm for 1 minute onto the glass microscope slide coated with PAE. For better adhesion, the resulting samples comprising random CNC/PAE and aligned CNC/PAE were baked at 105 °C for 5 minutes, which covalently bonds CNC to PAE.<sup>19</sup> As a control, PAE solution on glass slides was drop-cast after hydrophilizing the slides using plasma treatment for 8 to 10 minutes.

## **2.4 Cellulose acetate and regenerated cellulose preparation**

To prepare glass substrates coated with cellulose acetate, 0.25 % cellulose acetate was prepared by dissolving cellulose acetate powder (0.125 g) in 50 g acetone with stirring. The cellulose acetate was then spin-coated onto a clean glass slide at 4000 rpm for 30 s. To regenerate the cellulose acetate films, a solution of sodium methoxide in methanol (2 vol.%) was prepared, and cellulose acetate coated glass slides were immersed in this solution overnight. The slides were subsequently rinsed with methanol and water to remove any residues. The resulting regenerated cellulose and cellulose acetate coatings were analyzed using AFM.

## **2.5 Testing protocol – blood typing studies and its quantification**

Droplets of 3  $\mu$ L of both group O and group A human blood were used to explore blood typing in a batch-wise method. 3  $\mu$ L Anti-A monoclonal antibody reagent was mixed with each human blood sample in a glass vial with gentle shaking. The pre-mixed sample was then placed carefully on the substrates (random CNC, regenerated cellulose and glass) and were air-dried

for about 25 minutes at controlled relative humidity (50%). 200 mL of PBS was taken in a rectangular plastic beaker wherein the substrates with dried human blood/antibody were immersed. The beaker was then subjected to controlled agitation using an orbital shaker at 60 rpm for 3 minutes. Samples before and after PBS washing were analyzed using optical microscopy in bright field transmission mode.

The test was quantified by calculating the fraction of blood 'Ø' after PBS washing using Image-J software. Optical microscopy images of the dried blood spots were opened in Image-J and then converted into a binary file (8-bit) using the threshold option. A live histogram was then recorded wherein the blood spot areas were selected to obtain the intensity of the selected blood spot area. The intensity corresponding to '255' (*i.e.* the total area covered by blood cells) was noted for the blood spot area before and after PBS washing, and the average ratio of pixels after PBS washing to pixels before washing was calculated. The method was repeated for all the surfaces (CNC, regenerated CNC and glass) to obtain the graph.

## **2.6 Measuring contact angle**

To determine the contact angle of the fluids used, 2 µL of human blood was applied as a sessile drop onto the substrates analyzed. For control measurements of the water contact angle of the substrates, a sessile drop of water (3 µL) was used. As both water and human blood evaporate quickly, five repeat measurements were conducted in each case, and the average contact angle and standard deviation were reported.

## **3. Results and Discussion**

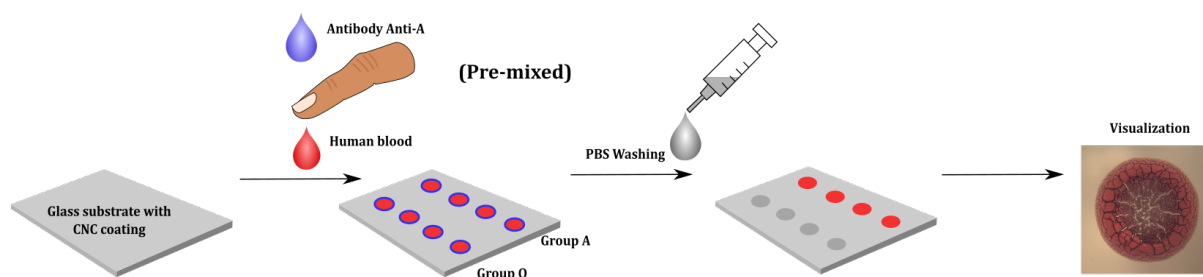


**Figure 1:** Schematic illustrating the conceptual application of cellulose nanocrystal (CNC) surfaces for blood typing. Antibodies pre-mixed with human blood are dried onto the CNC surface. In a successful test, after washing with PBS, the positive cells (group A) remain and the negative cells (group O) are washed off.

In this study, cellulose nanocrystals are investigated as coating material for cell diagnosis (**Fig. 1**). Model droplets made of a series of specific biomolecules (*e.g.* antibodies) pre-mixed with human blood are deposited onto the cellulose surface. The positive cells interact with their specific antibodies, agglutinate and strongly adsorb onto the CNC surface; they do not desorb upon buffer (PBS) washing, whereas negative cells do. This leaves a clear visual signal. The positive cells can be further visualized using physicochemical or spectroscopic characterisation. Advanced cell diagnosis is limited with paper based diagnostics as the thickness, roughness and opacity of paper restrict further probing of the properties of the dried blood drop or cells. In this method, cells can easily be investigated by optical imaging or spectroscopy thanks to the transparent substrate.

### 3.1 Surface morphology

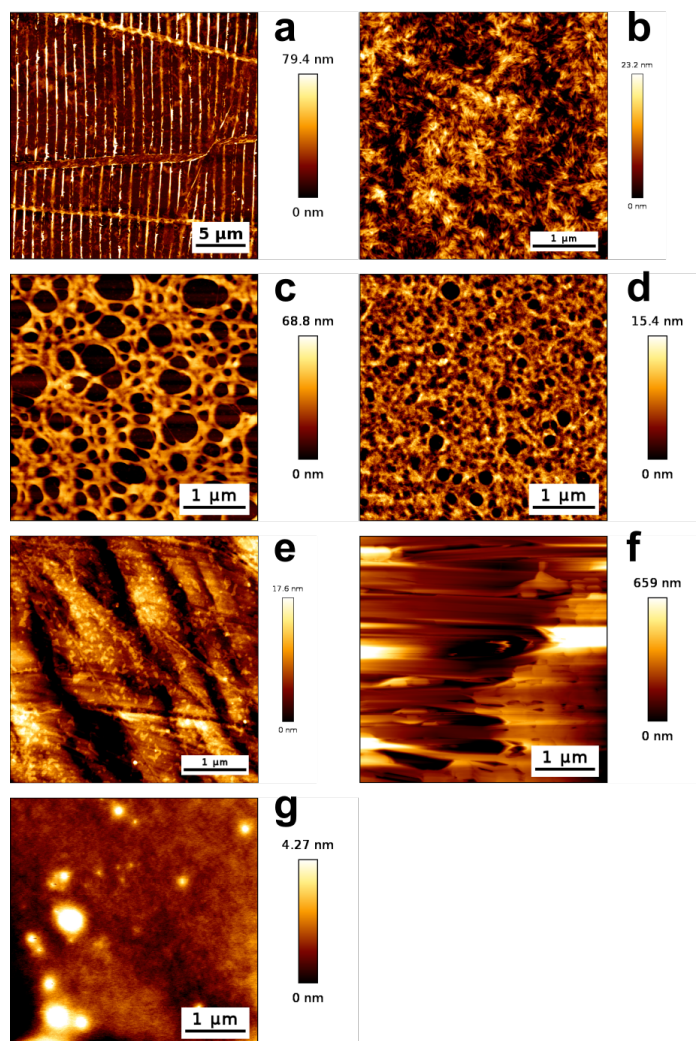


**Figure 2:** AFM images showing a) Aligned CNC surface with a periodicity of the order of 800 nm; b) Random CNC coated onto glass; c) Regenerated cellulose; d) Cellulose acetate; e) Polystyrene; f) PTFE surface and g) PAE surface.

To explore CNC-coated surfaces for blood droplet analysis, we first examine aligned CNCs and random CNCs, along with PAE, cellulose acetate, and regenerated cellulose – all coated onto glass microscope slides. Polystyrene and PTFE surfaces were also studied to deconvolute the effects of surface chemistry from morphology on wettability.

The morphology of the surfaces investigated was analysed using atomic force microscopy (AFM) in intermittent contact (AC) mode (**Fig. 2**). The average root mean square (RMS) roughness was calculated from the AFM height images and plotted for comparison in **Fig. 3**. Roughness analysis reveals PAE to be the smoothest surface ( $0.4 \text{ nm} \pm 0.2 \text{ nm}$ ),



essentially reflecting the underlying glass slide, and PTFE the roughest ( $113.1 \text{ nm} \pm 39.5 \text{ nm}$ ). The random CNC surface ( $5.3 \text{ nm} \pm 0.3 \text{ nm}$ ), which is the prime interest of our study, has a low surface roughness and is transparent, prospectively ideal properties for visualizing cells. The wettability of a surface is governed by surface chemistry, liquid composition and surface roughness. Since blood is a complex fluid with multiple components, it is necessary to understand the effect of surface roughness on wettability of blood droplets. Previously, we showed that roughness affects liquid droplet contact angle.<sup>21</sup> Surface roughness induces droplet pinning, an important factor to control drying patterns.<sup>22</sup>

### 3.2 Wettability

The contact angle of reagent blood cells (3% v/v), human blood and water measured for aligned CNC, random CNC, PAE, polystyrene and PTFE are presented in **Fig. 3**; the root mean square (RMS) roughness of the substrates are also indicated. Sessile drop images used for the blood contact angle measurement on the different surfaces are shown in **Fig. S1**. Reagent blood cells are obtained from blood but with the plasma replaced by simple aqueous buffer, and thus exhibit relatively higher surface tension and lower viscosity compared to whole human blood. Such a model fluid is particularly useful in this instance, as the suspended cell volume is low, enabling easy visualisation of individual cells, and samples are constant and very reproducible, unlike blood which has considerable composition variability among individuals. The reagent blood cells are suspended in an isotonic citrate phosphate buffer solution containing a purine, a nucleoside and glucose.

In addition to analysing the complex human blood, reagent blood cells of low concentration were explored as a simpler model system for comparison. The contact angles for droplets of whole blood and reagent blood cells are low on PAE and high on PTFE surfaces. The contact angle of human blood on aligned CNC, random CNC and polystyrene (apparently) were almost identical. However, the contact angle of a reagent blood cells droplet on aligned

CNC is higher than on random CNC. Interestingly, although surface roughness does not correlate strongly with blood droplet contact angle for the surfaces studied, substrates of varying wettability exhibit markedly different droplet drying profiles. We previously reported the contact angle of water droplet to be significantly higher on aligned CNC surfaces than on randomly orientated CNC.<sup>21</sup> However, the contact angle of whole blood droplets on aligned and random CNC are almost identical. This observation is at first surprising. There are 3 main differences between blood and water: 1) the surface tension of blood is lower ( $\sim 35$  mN/m)<sup>23</sup> than water ( $72$  mN/m)<sup>24</sup>, 2) its viscosity is higher and it exhibits non-Newtonian rheology due to the deformable red blood cells,<sup>25</sup> and 3) proteins from the blood plasma adsorb, thus changing the contact angle or wettability of the surfaces.<sup>26</sup> Blood proteins, mainly albumin and fibrinogen, affect cellulosic materials' wettability by adsorbing at the three-phase contact line during the time frame of wetting, thus changing the interfacial force balance.<sup>26,27</sup> Although we anticipate that the innate hydrophilicity of CNCs is the primary driving factor in the wetting seen here, it is likely that charge also has a role to play, as blood contains many highly ionised proteins in addition to the charged cell surfaces. This may also facilitate wetting of blood on CNC surfaces. As random CNC and aligned CNC showed almost the same contact angle for human blood, random CNC was selected to study owing to its ease of preparation.

It is known that substrate wettability significantly affects droplet drying profiles due to the initial spreading of the drop, pinning of the contact line, modulation of evaporation dynamics, *etc.*<sup>28</sup> In crude terms, we expect that greater initial blood drop spreading will result in a stain where cells are well-dispersed on the substrate, and thus we anticipate that the surfaces explored should show significantly different dried blood drop morphologies.

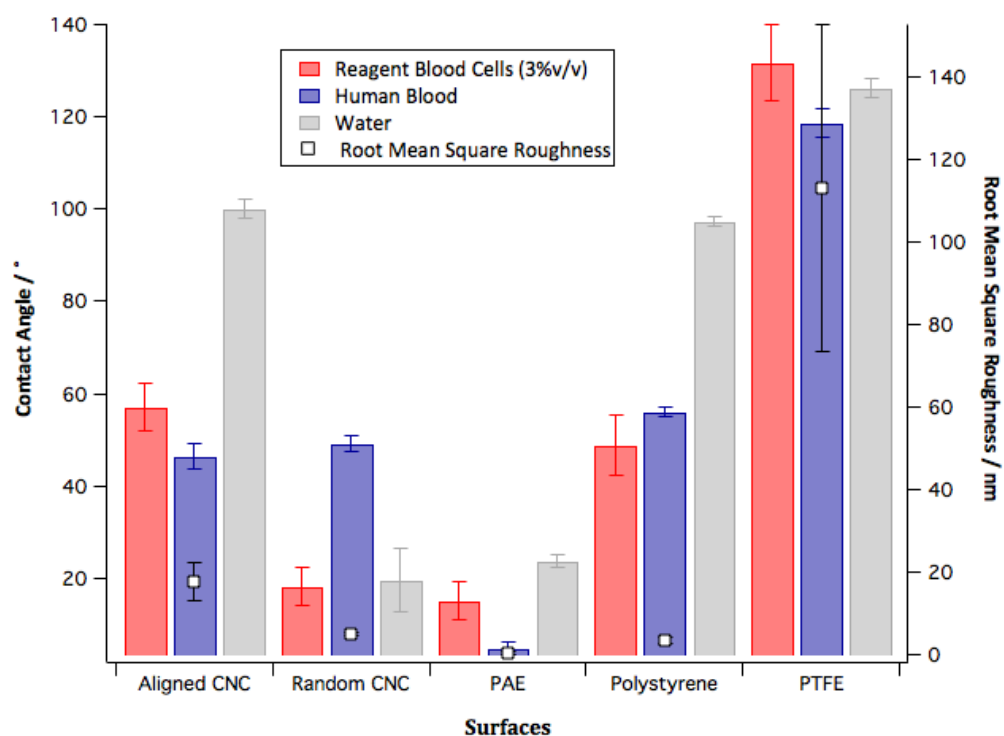


**Figure 3:** Contact angle values of reagent blood cells (3% v/v), human blood, and water on different surfaces along with their surface roughness values.

### 3.3 Drying profile: effect of fluid and surfaces

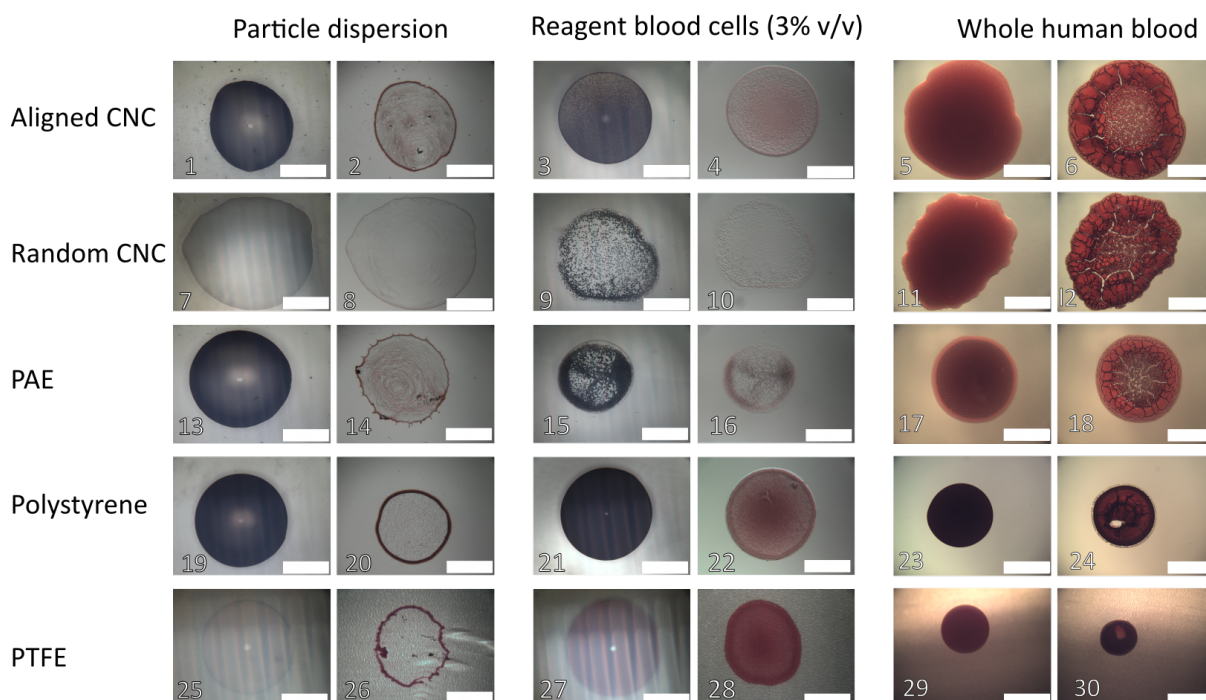


**Figure 4:** Drying profile optical images of particle dispersions, reagent blood cells and human blood (0.5  $\mu\text{L}$  each) on (1-6) aligned CNC, (7-12) random CNC, (13-18) PAE, (19-24) polystyrene and (25-30) PTFE. The before (left panels) and after (right panels) drying images in each case set were taken in reflectance and transmittance mode respectively.

Human blood is a complex fluid made of three types of cells suspended in a plasma containing a high concentration of proteins and inorganic salts with traces of lipids and saccharides.<sup>3</sup> To better understand the drying profiles of blood droplets, it is instructive to observe how simpler fluids dry on model surfaces. Polystyrene particle dispersions (mean diameter 0.44  $\mu\text{m}$ , 10.35% solids) and reagent cell suspensions (having no protein or surfactant) were selected as model suspensions for the drying study. This provides insight into the general pattern formation as affected by the particular substrate used, which involves a complex convolution of evaporation dynamics, surface characteristics and dispersion characteristics.<sup>28</sup> The latex particles were chosen as at this size the suspension is stable; larger polystyrene particles tend to rapidly sediment, and thus are a poor model for the rather stable blood cells. Suspension stains were investigated on model surfaces in terms of the drying profile of particle dispersions; the surfaces studied include: aligned CNC, random CNC, PAE, polystyrene and PTFE (**Fig. 4**), all coated onto glass microscope slides. A prominent coffee-ring effect<sup>29</sup> was seen for the PAE, PTFE and polystyrene surfaces, and was also apparent on aligned and random CNC surfaces. The ratio of width of the droplet stain before and after drying is tabulated in **Table S1** (supporting information). Aligned CNC and random CNC showed constant profile radii before and after drying, whereas the other surfaces showed a decrease in droplet radius after drying. PTFE surfaces, being very hydrophobic, exhibited distortion in the drying profile (**Fig. 4**). The constant radii in aligned CNC and random CNC indicates that the boundary is strongly pinned and the decrement in radius in other surfaces is due to evaporation and inward movement of the contact line. The factors that keep the liquid

boundary intact include evaporation rate and pinning forces, which are influenced by particle deposition, adsorption of any additives/dissolved material, substrate chemistry and roughness.<sup>3,30-32,33</sup>

Before investigating human blood, we examined the drying of reagent blood cell suspensions (3% v/v) to establish the morphology of stains and drying process. Reagent blood cells were dried onto the model surfaces and the stain profile was imaged before and after drying. With the exception of PTFE, all surfaces exhibited a constant droplet perimeter before and after drying. Individual dried reagent blood cells are clearly visible for further analysis only on the CNC surfaces (**Fig. 4**). The fluid tends to disperse more on random CNC due to the surface's hydrophilicity. The dried droplet patterns on the hydrophobic polystyrene and PTFE are unstable, tending to flake off the surface, indicating poor adhesion. The highly dense dried stains produced also refute optical analysis of individual blood cells. The PAE is a cationic polyelectrolyte, which can retain the negatively charged RBCs, hence the dried profile looks similar to the initial deposited drop. The constant radius of dried stain on the surfaces is attributed to pinning by surface roughness and deposition of the cells. Although inappropriate for blood testing itself, PAE was analysed as it is often used to enable adhesion of cellulosic materials, including in the alignment process we have used previously, and thus its properties are relevant if cellulosic surfaces are to be compared.

The drying profile of blood droplets is modulated by coupled mechanisms such as gelation, flow motion, crack formation and evaporation.<sup>3</sup> Cells are deposited at the pinned contact line edges due to solvent evaporation, which is non-uniform and driven by the solvent diffusion and capillary flow.<sup>34</sup> Gel formation occurs once the solute reaches the critical point after which the gelation front moves inward to complete the drying mechanism.<sup>35</sup> The reproducible crack patterns result from a mechanical balance set up by the non-uniform evaporation rate and adhesion of the gelled components of blood to the surface.<sup>36</sup>

In this section, we study the behaviour of whole human blood drying on the surfaces. To account for the effect of the relative humidity (RH), measurements were carried out at a constant temperature of 23°C and 50% relative humidity. The difference in stain pattern on the surfaces investigated with whole human blood compared to other fluid dispersions, was the formation of clear crack formations as seen in **Fig. 4**. The dried patterns were found to be well defined for the CNC and PAE surfaces, attributed to the wetting nature of these substrates. For hydrophobic surfaces including polystyrene and PTFE, the fluid dispersion dries into a complete solid flake which readily detaches from the surface; individual cells could not be detected. Droplet radius ratios before and after drying indicate a significant decrease in droplet radius for blood dried on PTFE, whereas it was found to be constant for cellulose nanocrystal surface, PAE and polystyrene surfaces, owing to pinning at the contact edge line. Even though PAE surfaces exhibit clear drying profiles for blood droplets, their use in diagnostic tests is limited because of the polymer's unspecific binding of all anionic material. The crack patterns that are clearly visible on the CNC and PAE surfaces form owing to the high volume fraction of cells within whole blood, which gels during evaporation, combined with the low surface tension of human blood of the order of 35 mN/m.

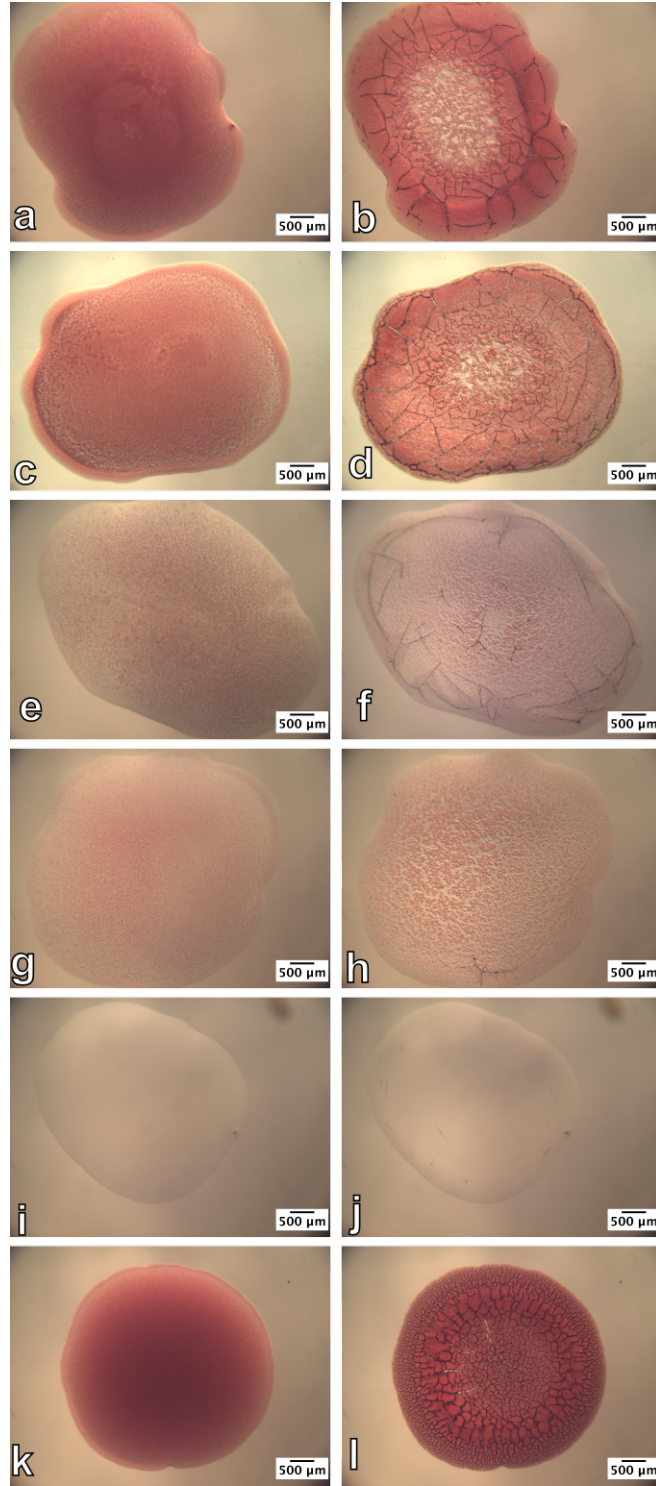


**Figure 5:** Drying profile optical images (before and after drying) of different RBC concentration of human blood in plasma on random CNC surfaces with: (a and b) 20% RBC in plasma; (c and d) 10% RBC in plasma; (e and f) 5% RBC in plasma; (g and h) 3% RBC in plasma; (i and j) plasma alone; and (k and l) human blood in PBS. In each case, the left panel shows the as-deposited liquid drop, and the right panel shows the drop after drying.

To explore conditions in which cell viability is optimal for diagnosis, the RBC concentration in human blood was varied by dilution, wherein blood and plasma were mixed in specific ratios and dried as seen in **Fig. 5**. For quick, simple and rapid diagnostic situations, whole human blood is preferentially used.<sup>37</sup> But for investigating cell morphology, for high end testing, *etc.*, it may be optimal to use lower cell concentrations. That is, low cell fractions are ideal for interrogating individual cells, whereas high concentration whole blood optimises ease of use for rapid testing. Since the wettability of human blood on random and aligned CNC was essentially identical, random CNC surfaces were used to explore the effects of RBC concentration in human blood. RBC concentrations of 20%, 10%, 5% and 3% blood cells in plasma were used, and plasma alone on random CNC was also analysed. It could be seen that as the plasma content in the blood samples increased, the degree of crack formation reduced, enabling easier visualization of individual cells. Plasma alone showed very few cracks and the cells were non-uniformly distributed. Thus, the crack formation in blood samples is seen to be a function of blood to plasma ratio.<sup>35</sup> The drying profile of RBCs in PBS (a simple electrolyte buffer as opposed to the protein-rich plasma) was analysed and compared to see whether the crack formation has any dependence on the solvent medium. It could be seen that the crack formation with PBS was similar to when whole human blood was used. In 3% RBC in plasma after drying (**Fig. 5h**), the cells are clearly visible as distinct objects, which is essential for some diagnostic purposes. The study indicates that for reagent blood cells, aligned CNC is best for further visualization of individual cells, whereas aligned and random CNC are of equal value when using whole human blood.



### 3.4 Comparing cellulose nanocrystal to amorphous cellulose surface

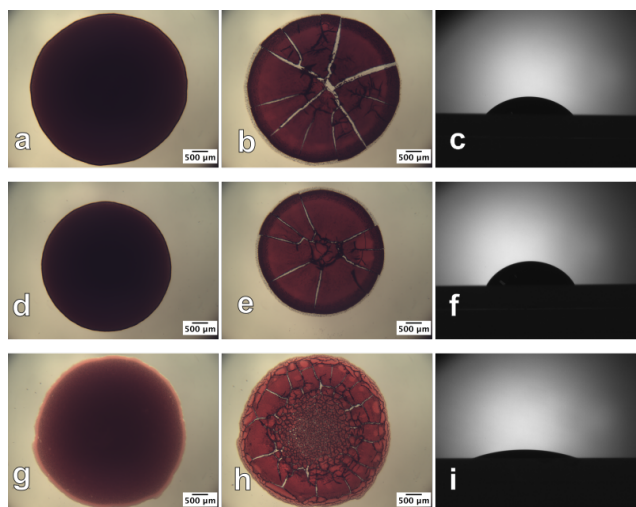


**Figure 6:** Optical images of human blood before (left), after (middle) drying and the contact angle sessile drop image (right) respectively on (a, b and c) glass slide surface; (d, e and f) Cellulose acetate surface; (g, h and i) Regenerated cellulose surface; The before and after drying images were taken in transmittance mode.

Crystalline CNC coatings can provide benefits over amorphous regenerated cellulose, cellulose acetate, or even the uncoated glass surfaces for blood drop analysis. The drying profiles of human blood droplets were examined on these surfaces as shown in **Fig. 6**. The dried profile of blood droplets on glass slides and cellulose acetate is somewhat distorted; adhesion is poor with stains tending to flake or peel off. The regenerated cellulose, however, shows a similar drying profile to that of cellulose nanocrystals. Contact angle measurements of human blood drops on these surfaces were also carried (**Fig 6. c, f and i**). The contact angle of whole blood on glass, cellulose acetate regenerated cellulose, aligned CNC and random CNC are  $44.1^{\circ} \pm 2.8^{\circ}$ ,  $59^{\circ} \pm 2.8^{\circ}$ ,  $15.7^{\circ} \pm 2.8^{\circ}$ ,  $46.4^{\circ} \pm 2.7^{\circ}$  and  $49.1^{\circ} \pm 1.7^{\circ}$  respectively. We previously showed that cellulose nanocrystals are stable for coating applications due to their charge behaviour.<sup>38</sup> Blood diagnosis on paper is limited by its opacity, which hinders further analysis relying on optical properties. Regenerated cellulose absorbs moisture and swells, owing to its amorphous structure, whereas CNC surfaces (crystalline) adsorb moisture only on

their surface without swelling.<sup>39</sup> Although CNC films hygroscopic and can take up water as humidity increases, the films themselves tend not to swell significantly due to the CNCs crystalline nature, as recently reported by Shrestha et al.<sup>40</sup> Indeed, thin cellulose films made from regenerated cellulose acetate were shown to swell by a factor up to three in water, and act as hydrogels into which biomolecules can diffuse.<sup>41,42</sup> This makes regenerated cellulose much more hydrophilic than a CNC surface. Thus, we anticipate that water will swell the regenerated cellulose beneath the dried blood drops, facilitating their detachment and reducing efficiency as a substrate for blood testing. This is explored in the section below. The low contact angle of whole blood on regenerated cellulose was observed, which is far less than on random and aligned cellulose nanocrystal surfaces. Even though the contact angle varies, the dried blood profile remains clear on all the cellulose surfaces, owing to the effect from the fluid dispersion like surface tension and volume fraction.

### **3.5 Blood typing on transparent cellulose nanocrystal coatings**

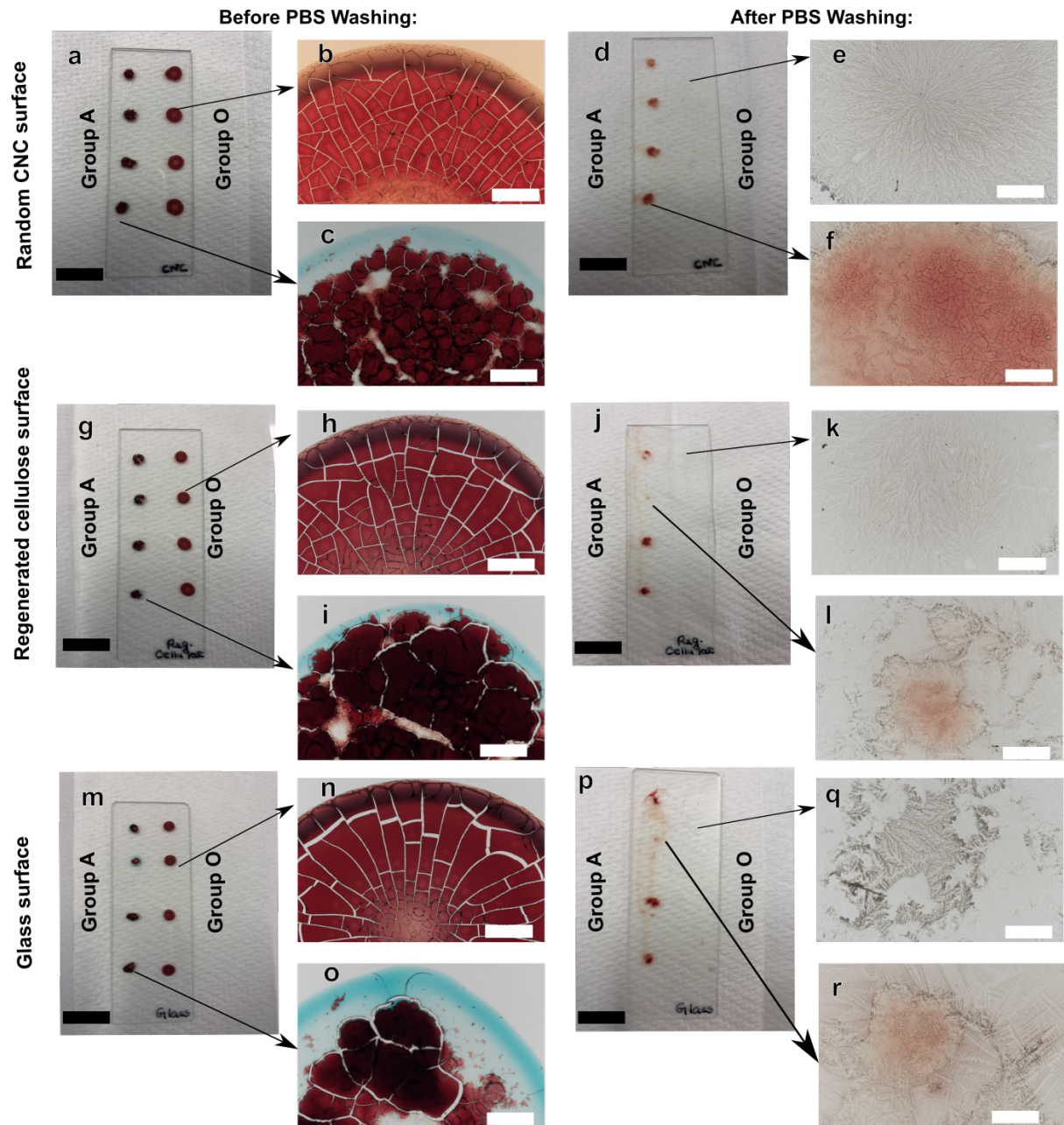


**Figure 7:** Optical microscope images of CNC (random), regenerated CNC and glass surfaces with human blood; positive test using A group blood (c, i and o) before and (f, l and r) after flushing PBS; Negative test using O group blood (b, h and n) before and (e, k and q) after flushing PBS. The antibody used for testing protocol was Anti-A. The blue shade before PBS flushing in the positive test samples indicates the antibody (Anti-A) which binds to the blood. Photographs of glass microscope slides with the dried human blood mixed with Anti-A on the above-mentioned surfaces before and after PBS wash are shown in (a, g, and m) and (d, j and p) respectively. The white scale bars in the optical images represent 500  $\mu\text{m}$  whereas the black scale bars in the images represent 1000  $\mu\text{m}$ .

The effectiveness of nanocellulose crystal coatings for low cost and instantaneous bio-diagnostics applications is analysed using blood typing as a specific example. The focus is to demonstrate the proof of concept and the benefits provided by a clear substrate. A simple testing methodology is demonstrated to compare a positive and a negative blood typing using the classical agglutination test. Here, we first analyse whether random CNC can facilitate differentiation and fine cell analysis between blood spots of positive and negative tests, respectively. Regenerated cellulose and glass were used as control samples to demonstrate the benefits of the CNC coating.

Droplets of A and O group blood were premixed with Anti-A serum and dried on the surfaces (**Fig. 7 a, g and m**). Group A blood provides a positive, and group O blood a negative agglutination reaction result for anti-A serum, with the expectation of significant agglutination for group A cells, and no agglutination for group O cells, respectively.<sup>43</sup> **Fig. 7 c, i and o** show the optical microscopic images of A group blood (positive) while **Fig. 7 b, h and n** display the O group blood dried on the sample surfaces before PBS washing (negative).

To type blood, the antibody to probe is mixed with a blood sample to analyse. Even before rinsing, the positive tests (A group blood) were clearly distinguishable from the negative tests (O group blood), as the former present stains of agglutinated (clumped) cells with antibody whereas the latter had the cells dispersed with the antibody. All O group blood stains were easily washed away by PBS solution (within 1 minute) whereas the A group blood on different substrates remained even after 3 minutes washing (**Fig.7 d, j and p**). The intensity of the positive result (A group blood) spots on random CNC was higher than on the other surfaces because of apparently superior adhesion (**Fig. 7 f, l and r**). The negatives on all surfaces were completely rinsed away (O group blood) with best transparency achieved on the cellulose coatings (**Fig.7 e, k and q**). The intensities of the blood spots were quantified using Image-J software (**Fig. 8a**), by which the blood surface coverage fraction ( $\varnothing$ ) remaining after PBS

washing was calculated. It can be seen that the random CNC surface provides greatest retained fraction and thereby most definitive result for positives. All negative tests (using O group blood) had similar and near-zero intensities. While triplicate testing shows reproducibility, the concept needs to be tested with all blood groups to record sensitivity and robustness for blood typing applications.<sup>10,13</sup> Cellulose nanocrystal coatings can provide access to further cell morphology definition for novel and current biomedical applications.<sup>44</sup>

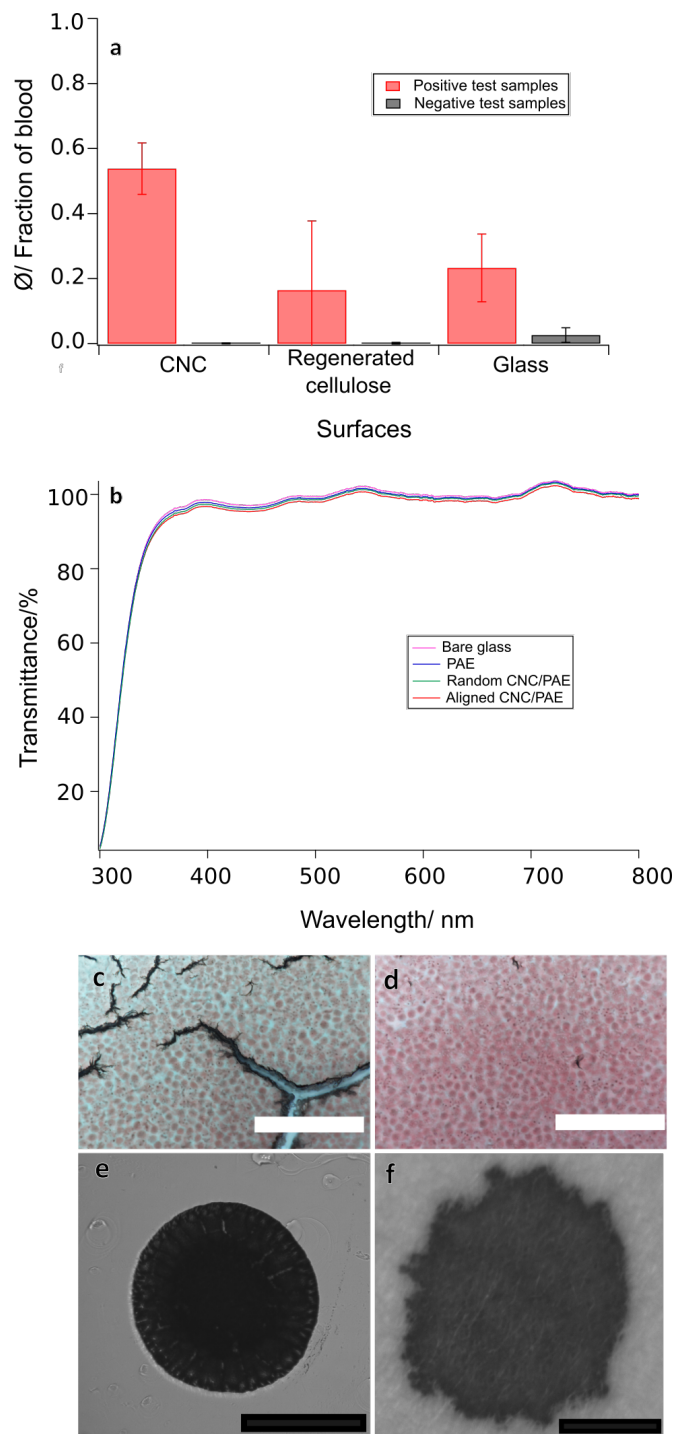


**Figure 8:** a) Quantification of the blood testing study which compares the fraction of blood remaining after PBS wash, ‘Ø’ for the blood spots on CNC (random), regenerated CNC and glass surface. b) The transparency of CNC coated glass substrates studied using UV-visible spectroscopy along with the control samples. Optical microscopy images of the O positive blood cells c) captured via Z- series scan at the crack region, d) at 100x magnification at crack-free region. The white scale bars correspond to 50  $\mu\text{m}$ . (e and f) Images of a blood spot on random CNC/PAE coated glass slide and paper respectively, captured using a CMOS camera and zoom lens. The black scale bars correspond to 100  $\mu\text{m}$  for a blood drop coated on random CNC and on paper.

The transparency of the random CNC and aligned CNC coatings on PAE coated glass substrates was studied using UV-visible spectroscopy (**Fig. 8 b**). The transparency study shows that the addition of random CNC and aligned CNC on PAE coated glass substrates does not decrease the transmittance of glass. This transparency is vital for fine microscopic analysis.<sup>44</sup> Using transparent cellulose nanocrystal surfaces enables further microscopic and spectroscopic diagnosis of blood cells (**Fig. 8 c and d**), where individual cells are now visible in the regions with and without cracks. The thickness of the random CNC on glass substrate was determined to be around 35 nm, as measured by scratching the surface and measuring an AFM height profile (**Fig. S2**).

To compare typical blood stains from the current state of the art technology (on-paper diagnostics) with the presented cellulose coatings on glass, a blood spot of the same volume (0.5  $\mu\text{L}$ ) was dried on both the random CNC/PAE coated glass slide and filter paper (**Fig. 8 e and f**). On paper the blood wicks to give an irregular stain, whereas on the random CNC surface, a clearly distinguishable drying profile which could be used for diagnostic purposes is obtained.

#### 4. Conclusion

Transparent and thin cellulose nanocrystal (CNC) films (35 nm thickness) varying in morphology were engineered and analysed for biomedical applications. The effect of chemical composition and surface structure on blood droplet wetting and drying patterns was investigated. CNC surfaces were therefore determined to be the most promising for blood typing, providing the desired intense red blood cell (RBC) stain needed to visualize a positive result, and resulting in complete stain removal for the negative. Regenerated cellulose and glass showed lower retention of blood cells for positive tests, whereas CNC-coated glass is transparent and demonstrates other advantages compared to paper-based diagnostics by allowing fine microscopic/spectroscopic characterization of the cells. The CNC surface is also preferred over regenerated cellulose films as it remains impervious to swelling once wetted, thanks to its crystalline structure.<sup>38,45</sup> Thin films of amorphous cellulose in contact with water swell by a factor of up to three, forming a hydrogel layer into which small molecules diffuse, and which enhances cell detachment.<sup>41,42</sup> However, aligning CNC presented no benefits over random CNC benefits in term of stain visualization or blood typing. Random CNC films are thus recommended for their ease of preparation and scalability.

To better understand the underlying mechanisms of blood stain formation and cell adhesion to these substrates, interaction studies between the proteins present in the blood and the CNC coating could be further explored, as well as forces between cells themselves and the surfaces. Crucially, the influence of pH and salt concentration on the CNC aqueous suspensions casted into coatings for diagnostics should be explored, as well as the effects of a number of different antibody/antigen systems, in order to determine the limits and applicability of the testing protocol.



## **ASSOCIATED CONTENT**

### **Supporting Information.**

## **AUTHOR INFORMATION**

### **Corresponding Author**

\*E-mail for R.F. Tabor: [REDACTED]. Tel: [REDACTED]

\*E-mail for Gil Garnier : [REDACTED] Tel: [REDACTED]

### **Funding Sources**

This work was supported in part by the award of an ARC Future Fellowship to R.F.T. (FT160100191).

### **Notes**

No competing financial interest declared by the authors.

## **ACKNOWLEDGMENT**

The State Government of Victoria and the Monash Centre for Atomically Thin Materials are duly acknowledged for the award of Victoria India Doctoral Scholarship and top-up scholarship respectively (R.P.). The authors thank the Australian Red Cross Blood Services for providing the blood samples for the study undertaken.

## **ABBREVIATIONS**

CNCs, cellulose nanocrystals; PAE, poly (aminoamide) epichlorohydrin; AFM, atomic force microscopy; PTFE, Polytetrafluoroethylene; RH, relative humidity; RBCs, red blood cells;

PDMS, polydimethylsiloxane; PEO, poly (ethylene oxide); RMS, root mean square; PBS, phosphate buffered saline; Anti, Antibody; Pos, positive; EDTA, Ethylenediamine tetraacetic acid.

## REFERENCES

- (1) Brust, M.; Schaefer, C.; Doerr, R.; Pan, L.; Garcia, M.; Arratia, P. E.; Wagner, C. Rheology of Human Blood Plasma: Viscoelastic Versus Newtonian Behavior. *Phys. Rev. Lett.* **2013**, *110*, 078305.
- (2) Luther, R. B.; Shanbrom, E. Non-thrombogenic Intravascular Time Release Catheter, *US4950256A*, 1990.
- (3) Chen, R.; Zhang, L.; Zang, D.; Shen, W. Blood Drop Patterns: Formation and Applications. *Adv. Colloid Interface Sci.* **2016**, *231*, 1-14.
- (4) Atwater, C. S.; Durina, M. E.; Durina, J. P.; Blackledge, R. D. Visualization of Gunshot Residue Patterns on Dark Clothing. *J. Forensic Sci.* **2006**, *51*, 1091-1095.
- (5) Hortolà, P. Red Blood Cell Haemotaphonomy of Experimental Human Bloodstains on Techno-Prehistoric Lithic Raw Materials. *J. Archaeol. Sci.* **2002**, *29*, 733-739.
- (6) Attinger, D.; Moore, C.; Donaldson, A.; Jafari, A.; Stone, H. A. Fluid Dynamics Topics in Bloodstain Pattern Analysis: Comparative Review and Research Opportunities. *Forensic Sci. Int.* **2013**, *231*, 375-396.
- (7) Adam, C. D. Fundamental Studies of Bloodstain Formation and Characteristics. *Forensic Sci. Int.* **2012**, *219*, 76-87.
- (8) Shatokhina, S. N.; Shabalin, V. N.; Buzoverya, M. E.; Punin, V. T. Bio-Liquid Morphological Analysis. *Sci. World J.* **2004**, *4*, 657-661.
- (9) Smalyukh, I. I.; Zribi, O. V.; Butler, J. C.; Lavrentovich, O. D.; Wong, G. C. L. Structure and Dynamics of Liquid Crystalline Pattern Formation in Drying Droplets of DNA. *Phys. Rev. Lett.* **2006**, *96*, 177801.
- (10) Then, W. L.; Li, M.; McLiesh, H.; Shen, W.; Garnier, G. The Detection of Blood Group Phenotypes using Paper Diagnostics. *Vox Sang.* **2015**, *108*, 186-196.
- (11) Harmening, D. M. *Modern Blood Banking and Transfusion Practices*, 4th ed; E. A. Davis Company: Philadelphia, 1999.
- (12) Khan, M. S.; Haniffa, S. B. M.; Slater, A.; Garnier, G. Effect of polymers on the retention and aging of enzyme on bioactive papers. *Colloids Surf. , B* **2010**, *79*, 88-96.
- (13) Then, W. L.; Garnier, G. Paper Diagnostics in Biomedicine. In *Rev. Anal. Chem.* **2013**, *32*, 269.
- (14) Beck, I. A.; Drennan, K. D.; Melvin, A. J.; Mohan, K. M.; Herz, A. M.; Alarcón, J.; Piscoya, J.; Velázquez, C.; Frenkel, L. M. Simple, Sensitive, and Specific Detection of Human Immunodeficiency Virus Type 1 Subtype B DNA in Dried Blood Samples for Diagnosis in Infants in the Field. *J. Clin. Microbiol.* **2001**, *39*, 29-33.
- (15) Goldstein, J. L.; Young, S. P.; Changela, M.; Dickerson, G. H.; Zhang, H.; Dai, J.; Peterson, D.; Millington, D. S.; Kishnani, P. S.; Bali, D. S. Screening for Pompe Disease using a Rapid Dried Blood Spot Method: Experience of a Clinical Diagnostic Laboratory. *Muscle Nerve* **2009**, *40*, 32-36.

- (16) Abdelwhab, E. M.; Lüscho, D.; Harder, T. C.; Hafez, H. M. The Use of FTA® Filter Papers for Diagnosis of Avian Influenza Virus. *J. Virol. Methods* **2011**, *174*, 120-122.
- (17) Khan, M. S.; Thouas, G.; Shen, W.; Whyte, G.; Garnier, G. Paper Diagnostic for Instantaneous Blood Typing. *Anal. Chem.* **2010**, *82*, 4158-4164.
- (18) Su, J.; Al-Tamimi, M.; Garnier, G. Engineering Paper as a Substrate for Blood Typing Bio-Diagnostics. *Cellulose* **2012**, *19*, 1749-1758.
- (19) McLiesh, H.; Sharman, S.; Garnier, G. Effect of Cationic Polyelectrolytes on the Performance of Paper Diagnostics for Blood Typing. *Colloids Surf. , B* **2015**, *133*, 189-197.
- (20) Khan, M. S.; Li, X.; Shen, W.; Garnier, G. Thermal stability of bioactive enzymatic papers. *Colloids Surf. , B* **2010**, *75*, 239-246.
- (21) Prathapan, R.; Berry, J. D.; Fery, A.; Garnier, G.; Tabor, R. F. Decreasing the Wettability of Cellulose Nanocrystal Surfaces Using Wrinkle-Based Alignment. *ACS Appl. Mater. Interfaces* **2017**, *9*, 15202-15211.
- (22) Kusumaatmaja, H.; Yeomans, J. M. Modeling Contact Angle Hysteresis on Chemically Patterned and Superhydrophobic Surfaces. *Langmuir* **2007**, *23*, 6019-6032.
- (23) Hrnčíř, E.; Rosina, J. Surface Tension of Blood. *Physiol. Res.* **1997**, *46*, 319-21.
- (24) Vargaftik, N. B.; Volkov, B. N.; Voljak, L. D. International Tables of the Surface Tension of Water. *J. Phys. Chem. Ref. Data* **1983**, *12*, 817-820.
- (25) Merrill, E. W.; Pelletier, G. A. Viscosity of Human Blood: Transition from Newtonian to Non-Newtonian. *J. Appl. Physiol.* **1967**, *23*, 178-182.
- (26) Hertaeg, M. J.; Tabor, R. F.; Garnier, G. Effect of Protein Adsorption on the Radial Wicking of Blood Droplets in Paper. *J. Colloid Interface Sci.* **2018**, *528*, 116-123.
- (27) Grundke, K.; Bogumil, T.; Werner, C.; Janke, A.; Pöschel, K.; Jacobasch, H. J. Liquid-Fluid Contact Angle Measurements on Hydrophilic Cellulosic Materials. *Colloids Surf. , A* **1996**, *116*, 79-91.
- (28) Brutin, D.; Sobac, B.; Nicloux, C. Influence of Substrate Nature on the Evaporation of a Sessile Drop of Blood. *J. Heat Transfer* **2012**, *134*, 061101-061101-7.
- (29) Devineau, S.; Anyfantakis, M.; Marichal, L.; Kiger, L.; Morel, M.; Rudiuk, S.; Baigl, D. Protein Adsorption and Reorganization on Nanoparticles Probed by the Coffee-Ring Effect: Application to Single Point Mutation Detection. *J. Am. Chem. Soc.* **2016**, *138*, 11623-11632.
- (30) Goehring, L.; Clegg, W. J.; Routh, A. F. Solidification and Ordering during Directional Drying of a Colloidal Dispersion. *Langmuir* **2010**, *26*, 9269-9275.
- (31) Lee, W. P.; Routh, A. F. Why Do Drying Films Crack? *Langmuir* **2004**, *20*, 9885-9888.
- (32) Dragnevski, K. I.; Routh, A. F.; Murray, M. W.; Donald, A. M. Cracking of Drying Latex Films: An ESEM Experiment. *Langmuir* **2010**, *26*, 7747-7751.
- (33) Birk-Braun, N.; Yunus, K.; Rees, E. J.; Schabel, W.; Routh, A. F. Generation of Strength in a Drying film: How Fracture Toughness Depends on Dispersion Properties. *Phys. Rev. E* **2017**, *95*, 022610.
- (34) Wong, T.-S.; Chen, T.-H.; Shen, X.; Ho, C.-M. Nanochromatography Driven by the Coffee Ring Effect. *Anal. Chem.* **2011**, *83*, 1871-1873.
- (35) Sobac, B.; Brutin, D. Desiccation of a Sessile Drop of Blood: Cracks, Folds Formation and Delamination. *Colloids Surf. , A* **2014**, *448*, 34-44.
- (36) Pauchard, L.; Abou, B.; Sekimoto, K. Influence of Mechanical Properties of Nanoparticles on Macrocrack Formation. *Langmuir* **2009**, *25*, 6672-6677.
- (37) Watanabe, T.; Ohkubo, Y.; Matsuoka, H.; Kimura, H.; Sakai, Y.; Ohkaru, Y.; Tanaka, T.; Kitaura, Y. Development of a Simple Whole Blood Panel Test for Detection of Human Heart-Type Fatty Acid-Binding Protein. *Clin. Biochem.* **2001**, *34*, 257-263.
- (38) Prathapan, R.; Thapa, R.; Garnier, G.; Tabor, R. F. Modulating the Zeta Potential of Cellulose Nanocrystals using Salts and Surfactants. *Colloids Surf. , A* **2016**, *509*, 11-18.

- (39) Dankovich, T. A.; Gray, D. G. Contact Angle Measurements on Smooth Nanocrystalline Cellulose (I) Thin Films. *J. Adhes. Sci. Technol.* **2011**, *25*, 699-708.
- (40) Shrestha, S.; Diaz, J. A.; Ghanbari, S.; Youngblood, J. P. Hygroscopic Swelling Determination of Cellulose Nanocrystal (CNC) Films by Polarized Light Microscopy Digital Image Correlation. *Biomacromolecules* **2017**, *18*, 1482-1490.
- (41) Raghuwanshi, V. S.; Su, J.; Garvey, C. J.; Holt, S. A.; Holden, P. J.; Batchelor, W. J.; Garnier, G. Visualization and Quantification of IgG Antibody Adsorbed at the Cellulose–Liquid Interface. *Biomacromolecules* **2017**, *18*, 2439-2445.
- (42) Su, J.; Raghuwanshi, V. S.; Raverty, W.; Garvey, C. J.; Holden, P. J.; Gillon, M.; Holt, S. A.; Tabor, R.; Batchelor, W.; Garnier, G. Smooth Deuterated Cellulose films for the Visualisation of Adsorbed Bio-Macromolecules. *Sci. Rep.* **2016**, *6*, 36119.
- (43) Li, M.; Tian, J.; Al-Tamimi, M.; Shen, W. Paper-Based Blood Typing Device that Reports Patient's Blood Type “in Writing”. *Angew. Chem. Int. Ed.* **2012**, *51*, 5497-5501.
- (44) Huang, Z.; Raghuwanshi, V. S.; Garnier, G. Functionality of Immunoglobulin G and Immunoglobulin M Antibody Physisorbed on Cellulosic Films. *Front. Bioeng. Biotechnol.* **2017**, *5*, DOI: 10.3389/fbioe.2017.00041.
- (45) Howsmon, J. A. Water Sorption and the Poly-Phase Structure of Cellulose Fibers. *Text. Res. J.* **1949**, *19*, 152-162.

# Supporting Information

## Surface engineering of transparent cellulose nanocrystal coatings for biomedical applications

*Ragesh Prathapan<sup>α</sup>, Heather McLiesh<sup>β</sup>, Gil Garnier<sup>β\*</sup> and Rico F. Tabor<sup>α,\*</sup>*

<sup>α</sup>School of Chemistry, Monash University, Clayton, VIC 3800, Australia.

<sup>β</sup>Bioresources Processing Research Institute of Australia (BioPRIA), Department of Chemical  
Engineering, Monash University, Clayton, VIC 3800, Australia.

### Corresponding Author

\*E-mail for R.F. Tabor: [REDACTED]. Tel: [REDACTED]

\*E-mail for Gil Garnier: [REDACTED]. Tel: [REDACTED]

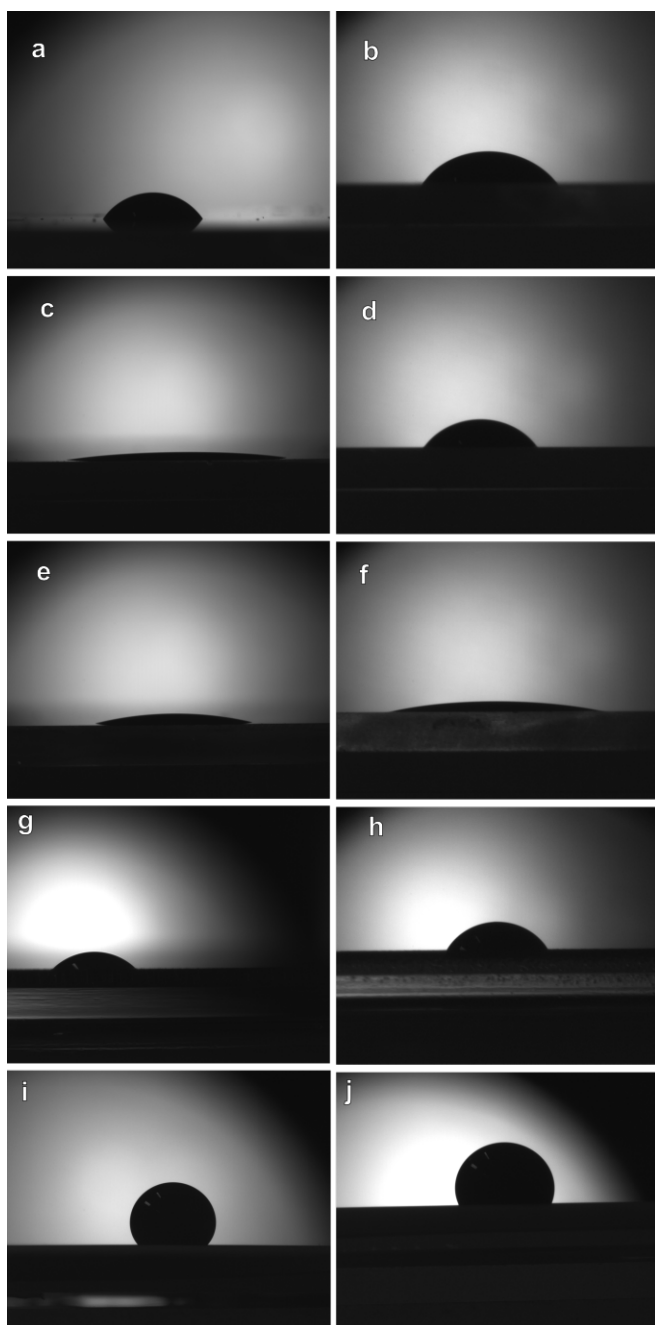


**Figure S1:** Contact angle sessile droplets of (a) Reagent blood cells on aligned CNC; (b) Whole blood on aligned CNC; (c) Reagent blood cells on random CNC; (d) Whole blood on random CNC; (e) Reagent blood cells on PAE; (f) Whole blood on PAE; (g) Reagent blood cells on polystyrene; (h) Whole blood on polystyrene; (i) Reagent blood cells on PTFE and (j) Whole blood on PTFE.

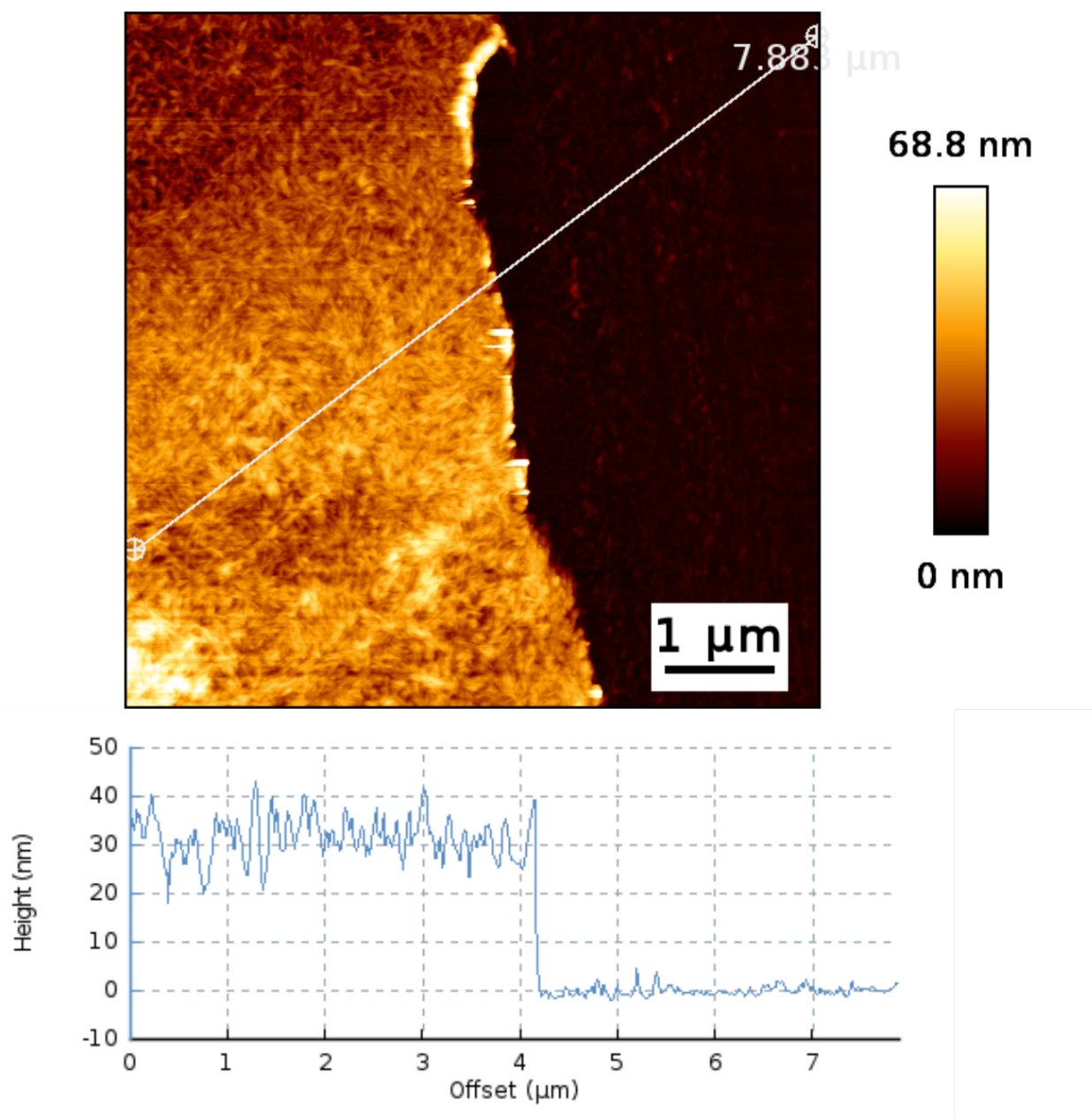


**Figure S2:** AFM height image above and the corresponding histogram of scratched random CNC coating surface on glass. The histogram (obtained by drawing a line profile over the AFM image) indicates the average thickness of the CNC coating to be  $\sim 35$  nm.

<b>Substrates/ liquid used</b>	Aligned CNC	Random CNC	PAE	Polystyrene	PTFE
Particle solution	0.94	0.98	0.85	0.83	0.75
Reagent RBC (3% v/v)	0.98	1	1	1	0.84
Whole Blood	1	0.97	1	1	0.84
Whole Blood (20% RBC)	–	0.98	–	–	–
Whole Blood (3% RBC)	–	0.98	–	–	–
RBC in PBS	–	1	–	–	–
Plasma	–	1	–	–	–



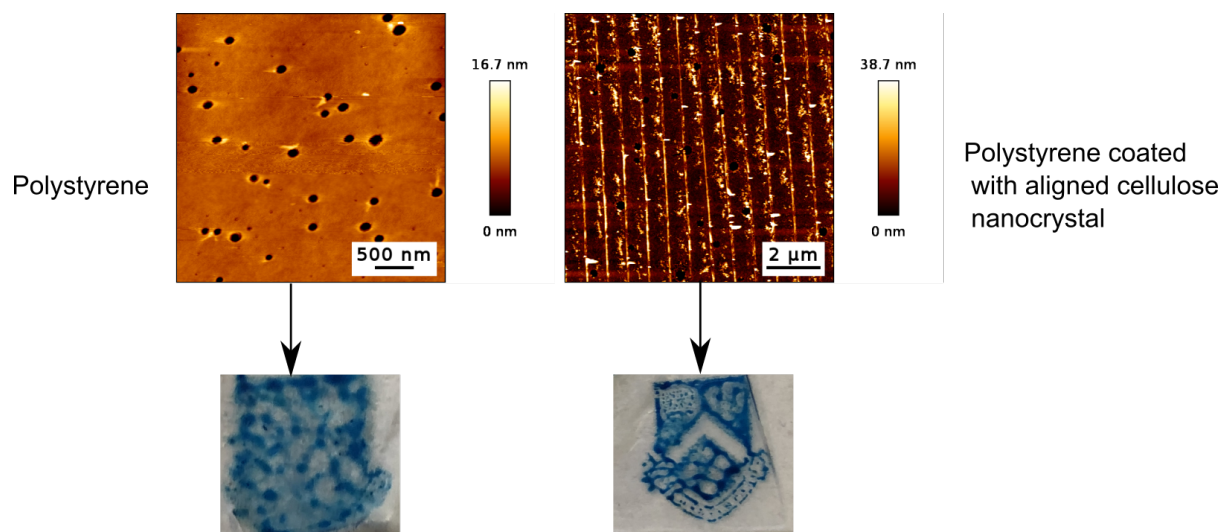
**Table S1:** Comparison of ratios of width of drying profile (after/before) for different liquid samples on different surfaces. The last 4 was recorded for random CNC substrate where the fluid was dried for visualization purpose.

The amount of sulfate groups on the cellulose nanocrystal surfaces (purchased from University of Maine, USA) was reported in literature using conductometric titration, and was found to be 1 wt.%.<sup>1</sup>

## REFERENCES

(1) Honorato-Rios, C.; Lehr, C.; Schütz, C.; Sanctuary, R.; Osipov, M. A.; Baller, J.; Lagerwall, J. P. F. Fractionation of Cellulose Nanocrystals: Enhancing Liquid Crystal Ordering without Promoting Gelation. *NPG Asia Mater.* **2018**, *10*, 455-465.

## Preface for Chapter 6



The aligned CNCs made using wrinkle-based alignment explored in Chapter 4 are coated onto a polystyrene surface, a commonly used hydrophobic surface that faces the limitation of ink bleeding, which affects printing resolution. We have already seen that aligned CNC decreases surface wettability using water, owing to strong pinning effects that result in high contact angle hysteresis and average critical roll-off angles (Chapter 4). Here, we try to examine whether water-based ink printed on aligned CNC coated polystyrene shows enhanced pinning and also try to analyse whether the alignment helps in preventing the spreading of ink on polystyrene surfaces.

DOI: 10.1002/((please add manuscript number))

Article type: Communication

**Enhancing printing resolution on hydrophobic polymer surfaces using aligned cellulose nanocrystal coatings**

*Ragesh Prathapan<sup>[a]</sup>, Bernhard Alexander Glatz<sup>[b],[c]</sup>, Anik Kumar Ghosh<sup>[b]</sup>, Stefan Michel<sup>[b]</sup>, Andreas Fery<sup>[b],[d]</sup>, Gil Garnier<sup>[e]</sup>, and Rico F. Tabor<sup>\*,[a]</sup>*

[a] [\*] R. Prathapan, Dr R. F. Tabor

School of Chemistry

Monash University

Clayton, VIC 3800

E-mail: [REDACTED]

[b] B. A. Glatz, A. K. Ghosh, S. Michel, Prof. A. Fery

Institute of Physical Chemistry and Polymer Physics

Leibniz Institute of Polymer Research

01069 Dresden, Germany

[c] B. A. Glatz

University of Bayreuth Graduate School

University of Bayreuth

Universitätsstr. 30, 95477, Bayreuth, Germany

[d] Prof. A. Fery

Chair for Physical Chemistry of Polymeric Materials

Technical University Dresden

Mommstr. 4, 01062 Dresden, Germany

[e] Prof. G. Garnier

Bioresources Processing Research Institute of Australia (BioPRIA)

Department of Chemical Engineering, Monash University

Clayton, VIC 3800

Keywords: alignment, cellulose nanocrystals, polystyrene, ink-jet printing, contact angle

High-resolution inkjet printing of a hydrophobic polymer surface (polystyrene, PS) is accomplished using a coating of aligned cellulose nanocrystals (CNC) that prevents the ink from bleeding. A periodically crack-free wrinkled (of wavelength around 850 nm) stamp is prepared by surface oxidation of an uniaxially stretched polydimethylsiloxane (PDMS) elastomeric substrate, and used as a template to transfer aligned cellulose nanocrystals (CNC) onto PS surfaces by wet stamping. The morphology of the aligned CNC coatings on PS is then compared with randomly deposited CNC on PS using atomic force microscopy (AFM). The wettability of the CNC and polymer surfaces with water and ink is measured and analyzed in the context of inkjet printing. This biomaterial coating technique enables high resolution

printing of modern water-based inks onto hydrophobic surfaces, for applications in renewable packaging and printing of biomolecules for high throughput diagnostics. Further, the technology is scalable to roll to roll manufacturing for industrial flexo printing.

Selective printing on various polymers using inkjet technology is central to a range of applications including drug delivery devices, fabrication of full colour polymer displays, transistors and biondiagnostics.<sup>[1],[2],[3],[4],[5]</sup> The stability of the ink, its spreading and adhesion to the surface as well as substrate roughness and chemical composition all contribute to the quality and resolution of printing.<sup>[6]</sup> Significant effort has been devoted to modifying inks for this purpose – mainly by tailoring their composition and rheology, or incorporating functional additives such as metallic particles. Park et al.<sup>[7]</sup> investigated ink-jet printing (piezoelectric) of silica based colloidal crystals onto hydrophobic and hydrophilic substrates, and analyzed how ink composition and drying morphology affected the printing. Wang et al.<sup>[8]</sup> used fluorinated patterned silica surfaces to study the effect of de-wetting of water-based conducting polymer inks, and found that the liquid viscosity and thickness were the controlling factors for the dewetting process. A similar study by Pudas et al.<sup>[9]</sup> investigated the effect of particulate conductive polymer based ink lines containing metal particles on paper and plastic substrates. They observed that the substrate smoothness had a superior influence over line resolution and resistance, that affected the printing quality. Tekin, et al.<sup>[10]</sup> reviewed the effect of ink on substrates, mainly the drying pattern formation and the basic theory behind droplet formation for piezoelectric print heads. The study highlighted the coffee ring effect, droplet size and velocity as key parameters affecting the quality of printing (determined using resistivity measurements as a function of curing temperature) on polymer surfaces. Gans et al.<sup>[11]</sup> investigated perfluorinated substrates using polystyrene polymer printed with non-volatile acetophenone-based inks to avoid the formation of ring-stains during droplet drying, which arises from pinning of the contact edge line convolved with evaporation rate.<sup>[12],[13],[14]</sup> The literature reports that for optimal ink-spreading on the substrate, the substrate surface energy should be higher than the ink

surface tension.<sup>[15]</sup> The structure and morphology of the substrate, including its porosity, are also important factors controlling the spreading of ink.<sup>[16]</sup>

Current technologies for preparing polymeric materials for printing often rely on surface treatment, such as plasma or corona discharge, to modify the top polymer layer, removing dirt, changing wettability and roughness.<sup>[17],[18]</sup> Strong chemical interactions and surface bonding are facilitated by such surface treatments that induce a high concentration of reactive surface functional groups.<sup>[19]</sup> These treatments increase surface free-energy and improve adhesive properties by eliminating pendant bonds from the surface.<sup>[20]</sup> For optimal adhesion and high-resolution printing, it is important to control the wettability of the polymer surface; to resolve this issue, a wide range of coating technologies have been utilized. Polymer surface modification using organic coatings has been reported extensively using UV-curable polymer coatings<sup>[21]</sup>, photo-graft polymers<sup>[22]</sup> and initiated chemical vapour deposition.<sup>[23]</sup> Inorganic coating techniques including plasma-enhanced chemical vapour deposition<sup>[24]</sup> and magnetron sputtering<sup>[23]</sup> use an energetic gas phase to deposit inorganic materials onto polymeric substrates. Enhancement of corrosion resistance, hardness, heat and electric conductivity of polymer surfaces is achieved using metallurgical coatings from chemical electro-less and vapour plating techniques.<sup>[25],[26]</sup> However, these high energy processes suffer from a lack of scalability or sustainability. Cellulose derivative coatings present an attractive alternative; however, some can absorb ink and swell when printed on, limiting printing resolution.<sup>[19]</sup> Recently, Nechyporchuk et al. investigated nanocellulose in the form of cellulose nanocrystals (CNCs), cellulose nanofibrils (CNFs) and carboxymethylated cellulose nanofibrils (CCNFs) for the consolidation of painting canvases.<sup>[27]</sup> Compared to the native canvas fibres, the nanocellulose coatings had a higher degree of crystallinity and good film forming properties, facilitating stable and reversible canvas consolidation. The importance of surface roughness was highlighted by Nechyporchuk, et al., using cellulose nanofibrils (CNFs) mixed with a plasticizer as a coating on woven cotton fabrics<sup>[28]</sup>. High resolution, high speed printing was enabled by this CNF coating, which facilitated the precise control of ink droplet deposition on the substrate.

Polystyrene, due to its low surface free-energy ( $\sim 43 \text{ KJ m}^{-2}$ ) and hydrophobicity, is generally a challenging surface for printing and gluing, despite its immense application in thermoformed packaging.<sup>[19]</sup> In this study, we have developed an effective method to inkjet print water-based ink onto hydrophobic polystyrene using aligned cellulose nanocrystal coatings. The alignment is achieved utilising template assisted self-assembly (TASA) of the CNCs from crack-free wrinkled surfaces. Such soft-lithographical surface patterns are prepared via plasma treatment of strained poly(dimethylsiloxane) (PDMS) substrates with a subsequent relaxation that leads to periodic sinusoidal surface corrugations.<sup>[29],[30]</sup> This provides a sustainable printing technology without affecting the properties of the underlying hydrophobic polymer, by preventing the spread of ink and achieving better printing resolution. Further, this technique is readily industrially scalable using roll-to-roll technology.

Crack-free wrinkled templates<sup>[31]</sup> were achieved using a known wrinkling procedure<sup>[32],[33],[34]</sup> (uniaxially stretching, surface oxidising and then relaxing) employing elastomeric poly(dimethylsiloxane) PDMS as substrate at different oxidation times (**Figure S1**). The process of wrinkle formation and the method of preparing aligned CNC coatings on polystyrene is shown schematically in **Figure 1(i-vi)** with details provided in the experimental section. Well-ordered, crack-free wrinkles were obtained at a strain of 30% and 135 s oxidation time (**Figure 1a**), resulting in a corrugation wavelength of 850 nm and a corrugation height of 120 nm. We previously showed that the level of ordering from printing aligned CNC was best with a wrinkle periodicity of  $\sim 700 \text{ nm}$ .<sup>[35]</sup> Polyethylene oxide (PEO) was applied to the wrinkled PDMS template as a non-adhesive agent to release the CNCs that are then deposited onto the PEO-coated template via spin-coating. To load the wrinkled substrate with CNCs, different spin-coating speeds ranging from 2000 rpm to 2500 rpm were tested to determine the effect on spreading of CNC suspensions; resolution was similar in all cases (**Figure S1**). Hence, spin-coating at 2500 rpm was used and the morphology of the CNCs was analysed using AFM as seen in **Figure 1b**. To understand the effect of CNC concentration on the degree of CNC alignment on

the wrinkled PDMS, concentrations of 3 mg/mL, 1 mg/mL and 0.5 mg/mL were spin-coated onto crack-free wrinkled PDMS surfaces as shown in **Figure 1c, d and e**, respectively, with PEO spin-coated as an initial step. All results were similar, indicating that CNC concentration is not an important variable. All subsequent CNC aligned surfaces were prepared at 135 s PDMS oxidation time, 30 % PDMS strain and 5 mg/mL CNC with PEO (1 wt %). The effectiveness of CNC transfer (**Figure 1f**) was observed through AFM imaging of the PDMS template after wet-stamping. CNC remnants were negligible, indicating the effectiveness of CNC transfer.

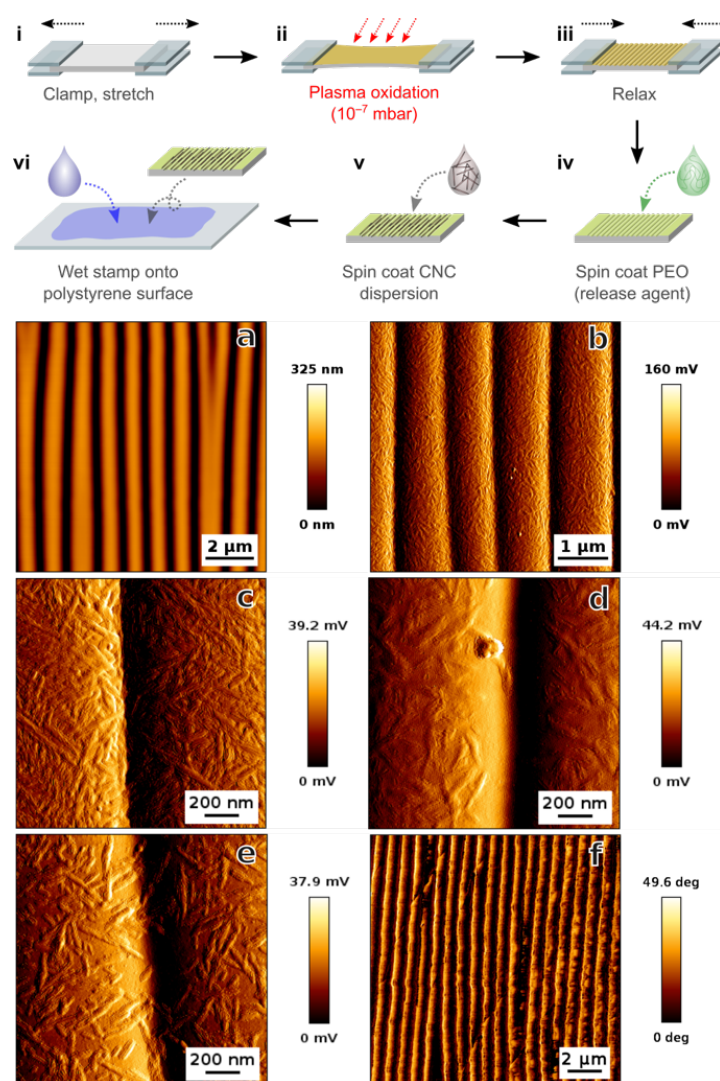


**Figure 1.** (i-vi) Schematic representation illustrating the preparation of aligned CNC on polystyrene surface using crack-free wrinkling technology. Topographical atomic force microscopy (AFM) images showing: a) topography of wrinkled PDMS templates (height profile) prepared using 30% strain and 135 s

oxidation time; b) the sample in (a) spin coated with PEO followed by CNC (5 mg/mL) (amplitude image), both at 2500 rpm; c) as (b) but with 3 mg/mL CNC; d) as (b) but with 1 mg/mL CNC and e) as (b) but with 0.5 mg/mL CNC. f) AFM phase image of PDMS stamp after stamping on polystyrene showing the effectiveness of CNC transfer.

The morphology of the original polystyrene surface as well as those coated with random CNC and aligned CNC was investigated using AFM as seen in **Figure 2** a–c. The hole-like perforations of the original (non-plasma treated) polystyrene film evolve during drying as the solvent (toluene) evaporates. To detect whether plasma treatment affected the surface morphology of polystyrene, AFM was performed after plasma exposure (**Figure S2**); analysis showed a roughness of  $2.1 \pm 1.2$  nm, similar to polystyrene without plasma treatment. This confirms that the plasma treatment changed the surface chemistry but not the roughness. It is widely accepted that surface wettability is strongly influenced by the roughness of the surface, with asperities and heterogeneities inducing different levels of pinning.<sup>[36],[37]</sup> Hence, the roughness was calculated from the AFM height images. Comparison of the surfaces in **Figure 2d** indicates that aligned CNC has a high degree of (in this case ordered) roughness compared to other surfaces, owing to its induced surface structure.

To determine the effect of aligned CNC coatings on the surface wettability of polystyrene, contact angle measurements were carried out. The maximum advancing and minimum receding contact angle of water (as a model for water-based inks) as well as the equilibrium contact angle of a commercial inkjet ink on all surfaces was measured (**Figure 2e**). The difference between the maximum advancing contact angle and the minimum receding contact angle defines the contact angle hysteresis (CAH).<sup>[38]</sup>

The aligned CNC on plasma treated polystyrene showed higher contact angle values compared to random CNC on polystyrene (plasma treated) and plasma treated polystyrene. The contact angles were similar both perpendicular and parallel to the alignment axis of the aligned CNC surface, supporting observations from our previous work.<sup>[35]</sup> Mild plasma treatment of the polystyrene surface is required to



facilitate effective transfer of the CNCs; we favoured plasma over an additional coating with a cationic polyelectrolyte to facilitate transfer as this treatment produces more robust coatings. The alignment technique was found to increase the surface roughness (owing to surface patterning), yielding higher contact angles with water and inducing strong pinning effects, as expected from previous work.<sup>[35]</sup> Randomly oriented CNCs on plasma treated polystyrene render a surface that is highly hydrophilic in nature, owing to the inherent hydrophilicity of the CNCs.

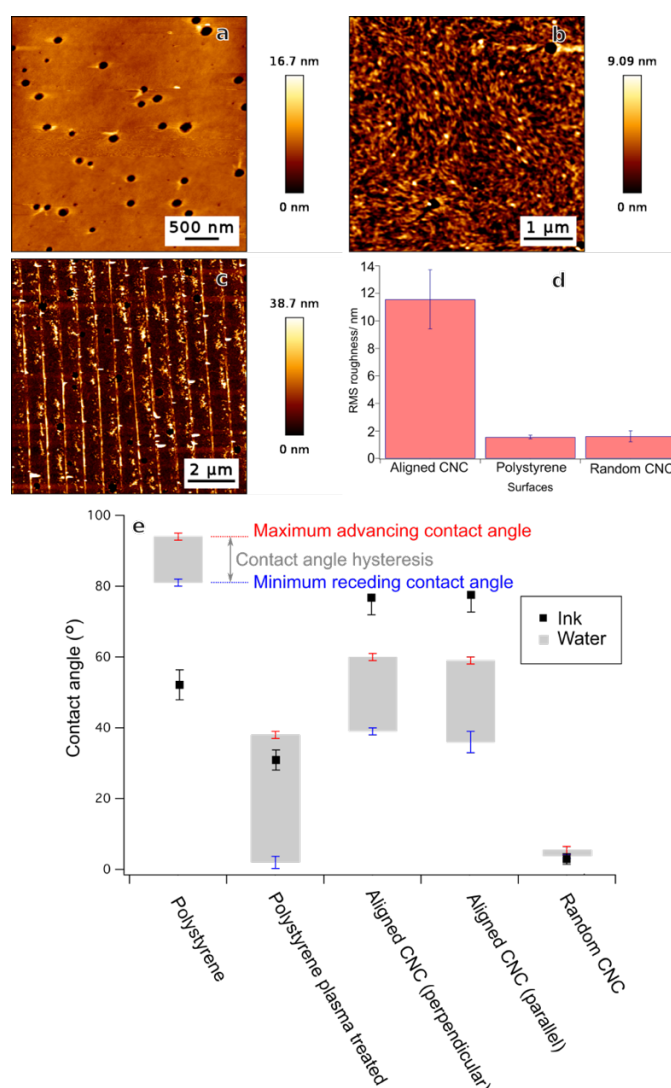


**Figure 2.** Atomic force microscopy (AFM) images showing topology of: a) polystyrene (non-plasma treated); b) random CNC on plasma treated polystyrene; c) Aligned CNC on plasma treated polystyrene.

d) Column graph comparing the roughness of the surfaces in (a–c); e) The maximum advancing and minimum receding contact angles of water, and the equilibrium contact angle of ink on the model surfaces in this study: as-prepared polystyrene, plasma treated polystyrene, aligned CNC on polystyrene (where the contact angle is measured separately perpendicular and parallel to the axis of alignment) and random CNC on polystyrene.

A similar trend was observed with contact angle measurements of ink on the surfaces examined. The wettability of water-based ink was considerably lower on the aligned CNC (both parallel and perpendicular to alignment), again owing to pinning effects.<sup>[36]</sup> We therefore anticipated that this pinning would lead to effective printing by retaining the ink droplet boundaries in place. This would maintain the ink droplets at their deposition site, preventing bleeding and feathering effects caused by wettable surfaces, or movement across the surface after droplet impact as is typically seen for hydrophobic surfaces.

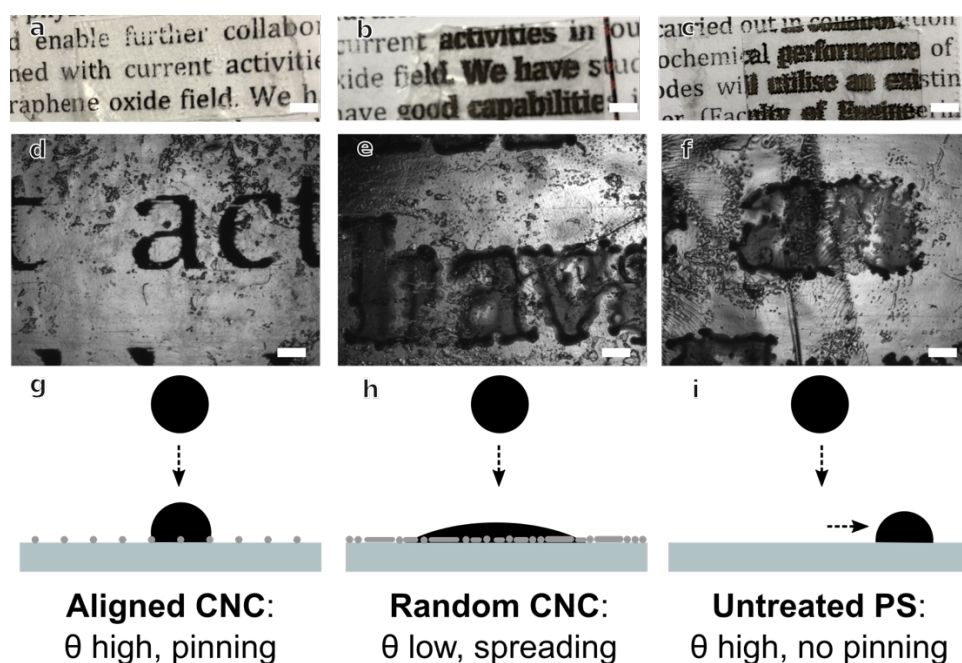


**Figure 3.** Photographs of text printed onto test surfaces, and corresponding optical microscopy images for (a and d) aligned CNC on polystyrene, (b and e) random CNC spin-coated onto polystyrene and (c and f) polystyrene surface. The white scale bars in (a, b and c) correspond to 700  $\mu\text{m}$  whereas in (d, e

and f) correspond to 200  $\mu\text{m}$ . (g, h and i) Schematic representation of ink behaviour on aligned CNC, random CNC and untreated polystyrene surface with varying pinning effects.

The hypothesis that aligned CNC coatings on polystyrene improves printing resolution was tested by inkjet printing of a black ink using a regular piezoelectric printer onto the surfaces of interest. The text printed on aligned CNCs stamped onto polystyrene is very clear, whereas the ink bleeds and feathers on both the random CNC coating on polystyrene, and the unmodified polystyrene surface as seen in **Figure 3a**, b and c, respectively. Optical microscopy reveals the letter ‘a’ to be printed very clearly without bleeding or feathering of the ink while the same letter ‘a’ is unclear on both random CNC on polystyrene and polystyrene surfaces (**Figure 3d**, e and f). Ink spreading was observed on the polystyrene and the random CNC coated polystyrene surfaces. A schematic representation of the assumed behaviour of ink droplets on different surfaces with varied pinning effects is shown in **Figure 3(g-i)**. This indicates that the ink spread is influenced by surface structuring using alignment, inducing pinning effects<sup>[39]</sup> with commensurate high surface roughness, thus preventing any contact line motion of the printed droplets. The unmodified polystyrene has a high contact angle with water/ink due to its hydrophobic surface; without hydrophilic pinning sites, droplets chaotically roll and spread on the surface, reducing printing resolution by creating bleeding and feather marks.<sup>[40]</sup> The periodic wavelength of the aligned CNC ( $\sim 850$  nm) is far less than the impacted droplet diameter (typically in the 10–20  $\mu\text{m}$  range), meaning the ink droplet boundaries pin on multiple cellulose features.<sup>[41]</sup> Surface engineering polystyrene using aligned CNC coatings thereby helps to achieve the highest printing resolution.

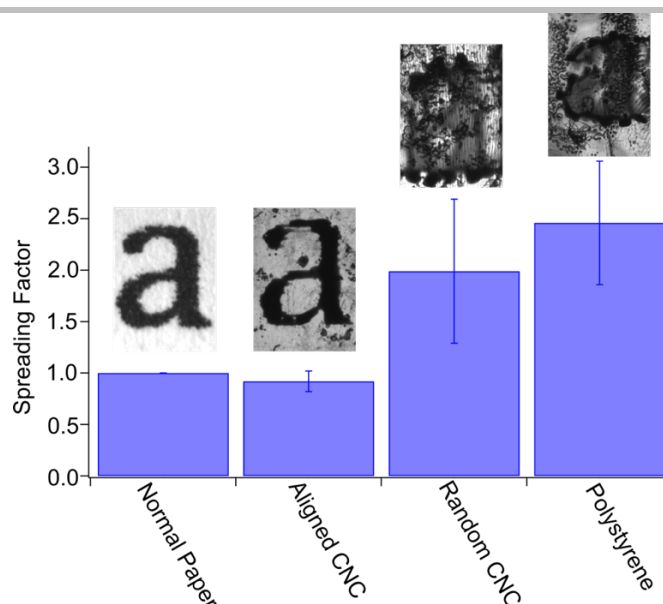


**Figure 4.** Column graph showing the calculated spreading factor of ink on normal (80 gsm white) paper as compared to coated surfaces: aligned CNC on polystyrene, random CNC on polystyrene and uncoated polystyrene, along with optical images of the letter ‘a’ printed on each surface respectively.

The enhancement of printing resolution using aligned CNC was quantified by calculating the spreading factor of the letter **a**, printed on normal paper as compared to uncoated polystyrene and polystyrene coated with aligned CNC or random CNC (**Figure 4**). The spreading factor was calculated by measuring the width of the lines making up the character at various different positions and calculating the average ratio of line thickness between the test surfaces and the character printed on regular 80 gsm white paper. The spreading factor is almost identical to paper in the case of the aligned CNC coated surface. Higher spreading factors for both random CNC coated polystyrene and uncoated polystyrene surfaces provide a quantitative measurement of ink spreading, indicating  $\sim 2\times$  loss of resolution in each case compared to aligned CNC.

In summary, highly ordered wrinkled PDMS templates of wavelength  $\sim 850$  nm were used to transfer aligned cellulose nanocrystal coatings onto polystyrene films, used as a model hydrophobic polymer surface. The alignment of cellulose nanocrystals locally increased the roughness of the surface in an ordered fashion, providing sites for liquid interface pinning, and hence decreasing the wettability in

---

a controlled manner. Such aligned cellulose nanocrystal coated polystyrene surfaces prevent ink bleeding in inkjet printing applications, typically using water based ink, thereby enhancing printing resolution. Further research could be carried out with a range of other hydrophobic surfaces, where printing resolution is a limiting factor due to ink bleeding. The current study may serve as a roadmap for investigating the printing of functional ink or biological fluids for high-throughput testing applications.

### Experimental Section

Kindly refer the supporting information for details.

### Supporting Information

Supporting Information is available from the Wiley Online Library or from the author.

### Acknowledgements

The State Government of Victoria and the Monash Centre for Atomically Thin Materials are acknowledged for the award of Victoria India Doctoral Scholarship and top-up scholarship respectively (R.P.). Financial support by the German Academic Exchange service (DAAD) -Thematic Network *Melbourne–Bayreuth Polymer/Colloid Network* e Federal Ministry of Education and Research (BMBF) is acknowledged. Thank to M. Nitschke for assistance with plasma treatment and sample preparation.

### Conflict of Interest

The authors declare no conflict of interest.

Received: ((will be filled in by the editorial staff))

Revised: ((will be filled in by the editorial staff))

Published online: ((will be filled in by the editorial staff))

### References

- 
- [1] B. J. de Gans, P. C. Duineveld, U. S. Schubert, *Adv. Mater.* **2004**, *16*, 203-213.
- [2] H. Sirringhaus, T. Kawase, R. H. Friend, T. Shimoda, M. Inbasekaran, W. Wu, E. P. Woo, *Science* **2000**, *290*, 2123-2126.
- [3] T. Shimoda, K. Morii, S. Seki, H. Kiguchi, *MRS Bull.* **2003**, *28*, 821-827.
- [4] W. E. Katstra, R. D. Palazzolo, C. W. Rowe, B. Giritlioglu, P. Teung, M. J. Cima, *J. Controlled Release* **2000**, *66*, 1-9.
- [5] F. Garnier, R. Hajlaoui, A. Yassar, P. Srivastava, *Science* **1994**, *265*, 1684-1686.
- [6] J. M. Grace, V. Botticelli, D. R. Freeman, W. Kosel, R. G. Spahn, *J. Adhes. Sci. Technol.* **1993**, *7*, 885-896.
- [7] J. Park, J. Moon, *Langmuir* **2006**, *22*, 3506-3513.
- [8] J. Z. Wang, Z. H. Zheng, H. W. Li, W. T. S. Huck, H. Sirringhaus, *Nat. Mater.* **2004**, *3*, 171.
- [9] M. Pudas, N. Halonen, P. Granat, J. Vähäkangas, *Prog. Org. Coat.* **2005**, *54*, 310-316.
- [10] E. Tekin, P. J. Smith, U. S. Schubert, *Soft Matter* **2008**, *4*, 703-713.
- [11] B.-J. de Gans, U. S. Schubert, *Langmuir* **2004**, *20*, 7789-7793.
- [12] R. D. Deegan, O. Bakajin, T. F. Dupont, G. Huber, S. R. Nagel, T. A. Witten, *Nature* **1997**, *389*, 827.
- [13] R. D. Deegan, O. Bakajin, T. F. Dupont, G. Huber, S. R. Nagel, T. A. Witten, *Phys. Rev. E* **2000**, *62*, 756-765.
- [14] R. D. Deegan, *Phys. Rev. E* **2000**, *61*, 475-485.
- [15] D. Pesach, A. Marmur, *Langmuir* **1987**, *3*, 519-524.
- [16] R. K. Holman, S. A. Uhland, M. J. Cima, E. Sachs, *J. Colloid Interface Sci.* **2002**, *247*, 266-274.
- [17] M. Tuominen, J. Lahti, J. Lavonen, T. Penttinen, J. P. Räsänen, J. Kuusipalo, *J. Adhes. Sci. Technol.* **2010**, *24*, 471-492.
- [18] J. W. Gooch, in *Encyclopedic Dictionary of Polymers* (Ed.: J. W. Gooch), Springer New York, New York, NY, **2011**, pp. 562-562.

- 
- [19] J. Izdebska, S. Thomas, *Printing on Polymers: Fundamentals and Applications*, Elsevier, USA, **2016**.
- [20] Y. Kusano, *J. Adhes.* **2014**, *90*, 755-777.
- [21] B. Türel Erbay, I. E. Serhatlı, *Prog. Org. Coat.* **2013**, *76*, 1-10.
- [22] H. Ma, R. H. Davis, C. N. Bowman, *Macromolecules* **2000**, *33*, 331-335.
- [23] K. K. S. Lau, K. K. Gleason, *Macromolecules* **2006**, *39*, 3688-3694.
- [24] A. S. E., H. M. L., *Chem. Vap. Deposition* **2005**, *11*, 457-468.
- [25] Y. Liao, B. Cao, W.-C. Wang, L. Zhang, D. Wu, R. Jin, *Appl. Surf. Sci.* **2009**, *255*, 8207-8212.
- [26] U. Schulz, N. Kaiser, *Prog. Surf. Sci.* **2006**, *81*, 387-401.
- [27] O. Nechyporchuk, K. Kolman, A. Bridarolli, M. Odlyha, L. Bozec, M. Oriola, G. Campo-Francés, M. Persson, K. Holmberg, R. Bordes, *Carbohydr. Polym.* **2018**, *194*, 161-169.
- [28] O. Nechyporchuk, J. Yu, V. A. Nierstrasz, R. Bordes, *ACS Sustainable Chem. Eng.* **2017**, *5*, 4793-4801.
- [29] S. Béfahy, P. Lipnik, T. Pardoën, C. Nascimento, B. Patris, P. Bertrand, S. Yunus, *Langmuir* **2010**, *26*, 3372-3375.
- [30] R. Dongjoon, L. Won-Kyu, O. T. W., *Angew. Chem. Int. Ed.* **2017**, *56*, 6523-6527.
- [31] M. Tebbe, M. Mayer, B. A. Glatz, C. Hanske, P. T. Probst, M. B. Muller, M. Karg, M. Chanana, T. A. F. König, C. Kuttner, A. Fery, *Faraday Discuss.* **2015**, *181*, 243-260.
- [32] C. Lu, H. Mohwald, A. Fery, *Soft Matter* **2007**, *3*, 1530-1536.
- [33] B. A. Glatz, M. Tebbe, B. Kaoui, R. Aichele, C. Kuttner, A. E. Schedl, H.-W. Schmidt, W. Zimmermann, A. Fery, *Soft Matter* **2015**, *11*, 3332-3339.
- [34] A. Schweikart, A. Horn, A. Böker, A. Fery, in *Complex Macromolecular Systems I* (Eds.: A. H. E. Müller, H.-W. Schmidt), Springer Berlin Heidelberg, Berlin, Heidelberg, **2010**, pp. 75-99.
- [35] R. Prathapan, J. D. Berry, A. Fery, G. Garnier, R. F. Tabor, *ACS Appl. Mater. Interfaces* **2017**, *9*, 15202-15211.

- 
- [36] K. Kurogi, H. Yan, K. Tsujii, *Colloids Surf. , A* **2008**, *317*, 592-597.
- [37] S. M. M. Ramos, E. Charlaix, A. Benyagoub, *Surf. Sci.* **2003**, *540*, 355-362.
- [38] C. W. Extrand, Y. Kumagai, *J. Colloid Interface Sci.* **1997**, *191*, 378-383.
- [39] Y. Lee, S. H. Park, K. B. Kim, J. K. Lee, *Adv. Mater.* **2007**, *19*, 2330-2335.
- [40] B. V. Burachinsky, Y. P. Jacob, *Printing on Polystyrene*, US3397074A, **1968**.
- [41] M. S. Khan, D. Fon, X. Li, J. Tian, J. Forsythe, G. Garnier, W. Shen, *Colloids Surf. , B* **2010**, *75*, 441-447.



Copyright WILEY-VCH Verlag GmbH & Co. KGaA, 69469 Weinheim, Germany, 2016.

## Supporting Information

### Enhancing printing resolution on hydrophobic polymer surfaces using aligned cellulose nanocrystal coatings

Ragesh Prathapan<sup>[a]</sup>, Bernhard Alexander Glatz<sup>[b],[c]</sup>, Anik Kumar Ghosh<sup>[b]</sup>, Stefan Michel<sup>[b]</sup>, Andreas Fery<sup>[b],[d]</sup>, Gil Garnier<sup>[e]</sup>, and Rico F. Tabor<sup>\*,[a]</sup>

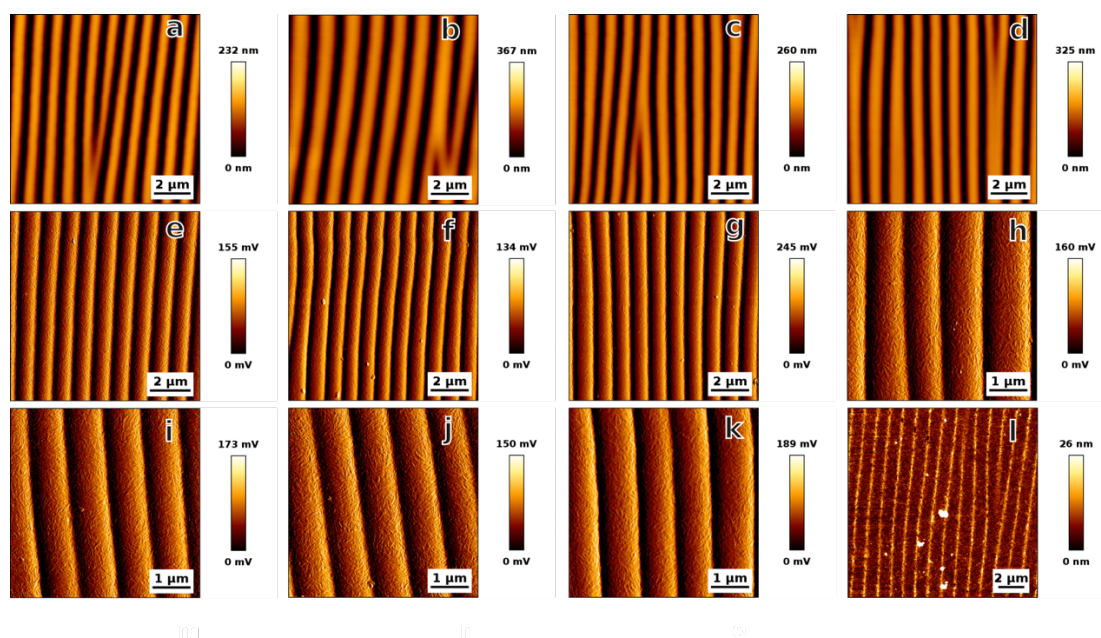


**Figure S1.** Atomic force microscopy (AFM) height images showing a) wrinkles on PDMS obtained for 30 % strain and 120 s oxidation time; b) same as ‘a’ with 165 s oxidation time; c) same conditions as ‘a’ except 105 s oxidation time; d) same conditions as ‘a’ except 135 s oxidation time; (e, f and g) AFM amplitude images with same conditions as ‘a, c and d’ spin-coated respectively with 5 mg/mL CNC and 1 wt% PEO. Atomic force microscopy amplitude images are being shown representing (h,i,j and k) 30 % strain 135 s oxidation wrinkles spin –coated with varying speeds of 2500 rpm, 2300 rpm, 2200 rpm and 2000 rpm to coat CNC/PEO on the wrinkled PDMS; l) AFM height image of aligned CNC stamped on polystyrene surface after repetitive contact angle measurements showing the robustness of the surface.

Optimization of PDMS wrinkles with various strain and oxidation times are shown in **Figure S1** (a-d). Irrespective of the oxidation time, the wrinkles formed were similar with a wavelength  $\sim 850$  nm. On the PDMS wrinkled surfaces, CNC (5 mg/mL) /PEO (1 wt%) was coated and observed using AFM as shown in **Figure S1** (e-g). There was no difference in the way the CNC was deposited on the wrinkled grooves as function of wrinkling conditions; hence 30% strain, 135 s oxidation time condition was selected for subsequent analysis. The effect of spin-coating conditions was explored (**Figure S1**, h-k) to understand whether the spread of CNCs could be controlled; however, the spread of CNC was similar at all conditions. The robustness of the aligned CNC on polystyrene was quantified using the average contact angle from 10 replicate using water; contact angle of  $63^\circ$  with a standard deviation of  $1.3^\circ$  resulted, similar to the initial stamped aligned CNC on polystyrene surface (**Figure S1**, l).

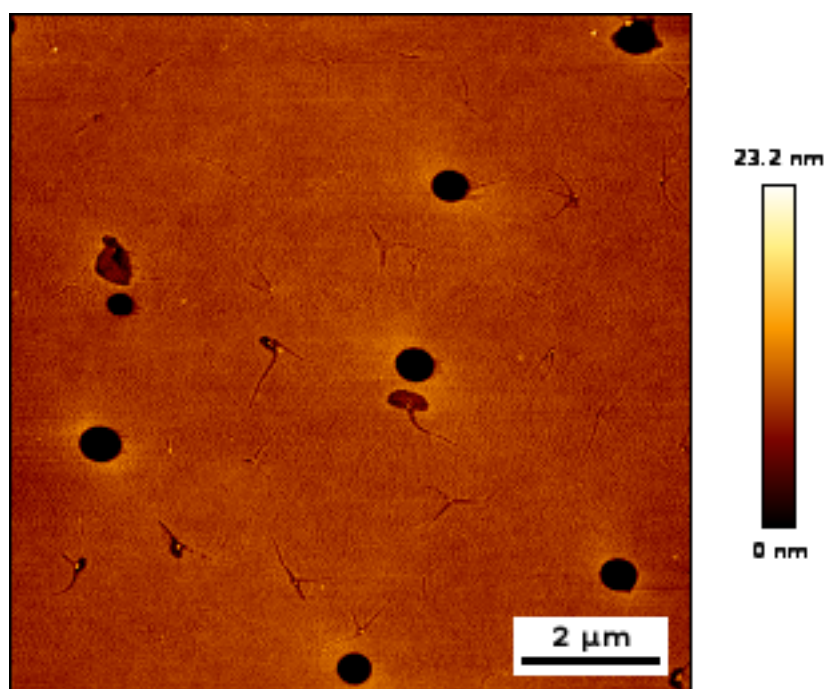


**Figure S2.** Atomic force microscopy (AFM) height images showing the polystyrene surface after 2 minutes exposure to 30 W plasma.

**Figure S2** indicates that the plasma condition just before wet-stamping does not change polystyrene morphology. Roughness was  $2.1 \pm 1.2$  nm, similar to the non-treated polystyrene, indicating that the surface morphology of the polystyrene has not been affected by the plasma conditions used. The hole-like perforations in the original (non-plasma treated) polystyrene film evolve during drying of the polymer as the solvent (toluene) evaporates.

## Experimental Procedures

### *Materials:*

Cellulose nanocrystals (CNCs, 12.2 wt%) with sulfur content 1–2%, dispersed in water, were purchased from the University of Maine Process Development Center. Polystyrene crystals (PS\_158K) were purchased from BASF, Germany. For polystyrene solution, analytical grade Toluene was purchased from Merck, Germany. Poly (ethylene oxide) (PEO, average molecular weight ( $M_v$ )  $400,000 \text{ g mol}^{-1}$ ) was used as a release agent for aligned CNC preparation, and was purchased from Sigma-Aldrich, USA. Silicone elastomer curing agent and Sylgard 184 silicone elastomer base (Dow Corning Corporation, USA) were used and prepared as per the manufacturer's instructions for polydimethylsiloxane (PDMS). For printing technique and contact angle measurements, films of polystyrene were prepared by evaporating the polystyrene (5 wt%) toluene solution at room temperature overnight. Ink (water-based dye) for printing on polymer surfaces was purchased from EPSON, Australia (cartridge 29XL, black).

### *Instrumentation Techniques:*

Atomic force microscopy (AFM, JPK Nanowizard 3) in alternating contact, AC mode was used for morphological analysis of the substrates. Bruker NCHV tapping mode cantilevers were employed. Spin coater (Laurell technologies, WS-400BZ-6NPP/LITE) was used to synthesis PEO/CNC coating on

---

wrinkled PDMS. A low-pressure plasma (Micro Sys apparatus (Roth & Rau, Wüstenbrand, Germany) with a microwave source ( $\sim 10^{-6}$  bar) of 800 W with nitrogen gas was used to create wrinkled PDMS. An air plasma chamber (model PDC 002, Harrick Scientific Corporation, USA) with 30 W plasma power was used to activate the wrinkled PDMS. To measure the wettability of water and ink on different surfaces, the contact angle measuring set-up (Data physics, OCA35) was used. An inkjet piezoelectric printer (EPSON, XP-245) was used to print the surfaces with text.

*PDMS wrinkles and aligned CNC preparation:*

The wrinkles were by stretching using a customized stretching device. The strained PDMS was subsequently oxidized to produce crack-free wrinkles upon strain relaxation. The aligned CNC on the polystyrene surface was prepared using a water-mediated transfer process as described in our previous work.<sup>[35]</sup> The wrinkled PDMS was initially surface activated using plasma (30 W) for 2 minutes. The wrinkled PDMS is then spin-coated with 20  $\mu\text{L}$  of PEO (1wt%) at 2500 rpm, 60 s, followed by CNC (5 mg/mL) deposition using spin-coating at the same conditions used for PEO. The prepared template with CNC was then stamped onto the polystyrene surface with the help of a tiny droplet of water ( $\sim 2 \mu\text{L}$ ), which facilitates the transfer of aligned CNCs onto the polystyrene surface. The PDMS stamp is carefully peeled-off from the polystyrene surface after 6 hours, to facilitate appropriate evaporation of water, that influences the CNC transfer.

**This page is intentionally blank**

# **Chapter 7: Concluding comments and future directions**

In this thesis, we have studied cellulose nanocrystals (CNCs, length 175 nm and 5 nm width), from their fundamental aspects to exploring their multi-functional properties in tailoring wettability when used as coating films, and applying them in biomedical and polymer materials applications. Atomic force microscopy (AFM), contact angle measurements and dynamic light scattering were used to characterize materials made in this thesis, demonstrating the relationship between nanostructure and macroscopic properties and function.

In Chapter 3, the effects of different salts and surfactants on the CNCs as a function of pH was investigated, to modulate the colloidal stability of CNC aqueous suspensions using zeta potential. Phase analysis light scattering (PALS) was employed to measure the zeta potential of the CNC suspensions. The roughness values of CNC cast films were calculated from AFM images to understand the relationship between roughness and zeta potential, which could be utilized in engineering tailored coating applications. An inverse relationship was found for CNC suspensions with ionic salt concentration, providing a path to control the morphology of CNC films. Hofmeister effects were clearly seen when using different salts (simple inorganic electrolytes or hydrophobic ions), whereas the use of surfactants with CNCs enabled supercharging and charge reversal effects. The study gives insight into controlling the stability and quality of films made from CNCs through choice of salts that affect the zeta potential of the dispersed CNCs, and hence the surface roughness of resulting CNC films.

Chapter 4 showed the use of a surface patterning method, wrinkling technology, to align cellulose nanocrystals. Wrinkle-based alignment reduced the wettability of CNC coatings (as observed using contact angle measurements), but preserved the inherent hydrophilic nature of

the CNCs themselves. The wrinkled templates were formed using poly(dimethylsiloxane) which was stretched and surface oxidised using plasma treatment, then relaxed to generate well-defined wrinkles. The templates were then coated with poly(ethylene oxide), PEO (acting as non-adhesive agent) and CNCs using spin-coating. The features of the stamp with CNCs were then transferred to a glass substrate coated with a cationic polyelectrolyte using a water-mediated transfer process, thereafter baking the glass slide to covalently bond the polymer to the CNCs. Compared to random CNC coatings, a high contact angle of  $\sim 100^\circ$  was found for micron-scale aligned CNCs. PDMS stamps with wavelength  $\sim 740$  nm showed the highest ordering of CNCs. Strong pinning effects induced by the aligned CNC structures were found to be the cause of the increase in water contact angle, also resulting in high average roll-off angles and significant contact angle hysteresis. The aligned CNC surfaces could be employed as coatings in anti-fouling applications under water, as it was seen that oil contact angles in water were high, with low hysteresis. The aligned CNCs themselves could be used as a template for aligning other materials, for instance aligning muscle cells for tissue engineering applications. Also, as these aligned CNCs are transparent along with their unique wettability characteristics, their use in coating technologies could be immense. The effects of the underlying chemistry of the substrate in optimizing the surface and wetting characteristics should be explored in detail to enable further application.

In Chapter 5, thin (35 nm) and transparent CNC films were engineered, and utilized in an exemplar biomedical application. The wetting of three fluids – a model latex particle dispersion, reagent blood cells and whole blood – was studied on six surfaces: aligned CNC, random CNC, regenerated cellulose, PAE, polystyrene and PTFE. The structure of all surfaces was characterized using AFM, and to separate the effects of surface chemistry and roughness, the cellulosic surfaces were compared with model surfaces. The drying patterns and the surface structure of blood droplets along with the effect of surface chemical composition was also

investigated. Lastly, the benefits of transparent CNC films for instantaneous blood typing diagnostics were demonstrated by depositing droplets of blood mixed with specific and non-specific antibodies and washing with buffer solution, for positive and negative tests, respectively.

The contact angle of human blood on random and aligned CNC surfaces of comparable roughness was low (around 45–50°) and similar on each surface. This differs from previous experiments where it was seen that water did not effectively wet the aligned CNC surface (contact angle 100°) but wetted random CNC (20°). The difference is likely due to the low surface tension of blood combined with plasma protein adsorption, all affecting wetting while minimizing pinning effects. The stains of blood droplets dried on the random and aligned CNC surfaces were well-defined and similar; red blood cells (RBCs) at the perimeter remained distinct and visible for microscopic or spectroscopic analysis. Cellulose was the surface providing the most uniform and readily characterised blood stains. Hydrophobic surfaces induce small stains with the cells drying into multilayer aggregates that are difficult to analyse. The cationic polymer PAE (used to adhere cellulose to glass substrates) adsorbs all cells non-specifically, while glass does not provide sufficient cell adhesion during drying for reproducible stains.

CNC surfaces are preferred over other forms of cellulose including regenerated cellulose and cellulose acetate, owing to their swelling nature upon moisture absorption. Further studies could explore the effect of salts and pH on the drying mechanism of RBC on CNC cast films for diagnostic purposes. Also, it would be interesting to know how proteins in blood like albumin, fibrinogen and collagen interact with the CNC surfaces, which would help to understand the drying mechanism of RBCs on CNCs in greater depth.

Chapter 6 focused on the alignment of CNCs on a model hydrophobic polymer, polystyrene surface using crack-free wrinkles of periodicity ~ 850 nm. The alignment of CNCs



increased the surface roughness, which modulated the wettability of the polystyrene surface by creating pinning sites on the surface. The prepared aligned CNCs on polystyrene were used to print water-based ink, eliminating ink bleeding on the surface. Control samples with random CNCs on polystyrene and the uncoated polystyrene surface showed severe ink-bleeding, a common failure of many hydrophobic surfaces. The aligned CNC coating could therefore be used to prevent ink-bleeding on other hydrophobic surfaces. To develop the concept further, printing of biological fluids and functional inks on aligned CNC coated hydrophobic surfaces could be further explored.

Knowledge of the stability of CNCs in a range of solution conditions, and how to align them to provide different functional surfaces can be utilized for future research. Other kinds of alignment of CNCs including magnetic alignment, electric field alignment, lithographic patterning, *etc.* could be used to see whether there is any change in wettability in a similar manner to what was observed for template-assisted CNC alignment in Chapter 4. As an alternative to the conventional PDMS wrinkling process (CNCs deposited after wrinkling PDMS), we could also try to deposit CNCs on non-wrinkled PDMS using spin-coating and then wrinkle the PDMS/CNC material to see whether CNCs are aligned better than the conventional method used, avoiding potential pitfalls of the current method.

Also, wrinkle-free alignment methods could be used to make graphene oxide (GO)/CNC composite materials wherein aligned CNC could be stamped over GO layers and then the GO reduced using methods such as laser reduction. This would enable the formation of unidirectional conductive surfaces. Bridging between CNCs and GO could be facilitated using simple ionic salts like calcium chloride. Also, the use of aligned CNCs for water droplet capture and retention, owing to its high average critical roll-off angle (due to strong pinning effects, shown in Chapter 4) could be explored in future studies. Another interesting aspect will be to investigate on hierarchical CNC structures for photonic applications.

Aligned CNCs as a template to grow muscle cells in a unidirectional manner may be a possible challenging avenue for future investigation. The biocompatibility of cellulose nanocrystals offers potential for aligning muscle cells. For this we would require a large surface with aligned CNC features, as the cell dimensions are in the  $\mu\text{m}$  range. The possibility of wrinkling other kinds of elastomeric materials using atmospheric plasma could be explored to enable the production of scalable large wrinkled surfaces. This could also provide a pathway to printing biomolecules for large-scale applications.

Chapters 5 and 6 indicate the proof of principle for blood typing and polymer printing respectively using cellulose nanocrystals. For scalability of blood diagnostics using transparent cellulose nanocrystal coatings on glass substrates, high-throughput and automated image analysis could be carried out in one batch-wise process, which could reduce the time and costs of such analysis when compared to conventional paper-based (or tube-based) diagnostics. The blood typing using transparent cellulose nanocrystal coatings could be extended to other blood groups like AB and B types, and also to study the effect of Rhesus factors associated with these blood groups through drying profiles and microscopic analysis on the coating surface. To check the robustness of the aligned cellulose nanocrystal coatings (accounting for the durability of the coating used) on hydrophobic polymers like polystyrene, contact abrasive tests and standard scratch tests could be employed. The technology I learned with this thesis findings could be further extended to the design of hydrophobic membranes for water purification (especially for reverse osmosis, RO system), where the pinning sites of the aligned CNC may help in separating the impurities to greater extend. The conventional RO membranes suffer the limitations of durability due to membrane fouling and the cost associated with the membrane preparation. We have already proved that aligned cellulose nanocrystal coating could be potentially used for anti-fouling applications and the use of these cellulose nanocrystals could also control the membrane characteristics such as porosity and wettability, which will be create a greater impact in the membrane technology.